

STEREOLITHOGRAPHY CURE PROCESS MODELING

A Dissertation
Presented to
The Academic Faculty

By
Yanyan Tang

In Partial Fulfillment
Of the Requirements for the Degree
Doctor of Philosophy in the
School of Chemical & Biomolecular Engineering

Georgia Institute of Technology

August 2005

STEREOLITHOGRAPHY CURE PROCESS MODELING

Approved by:

Dr. John D. Muzzy, Advisor
School of Chemical and
Biomolecular Engineering
Georgia Institute of Technology

Dr. David W. Rosen
School of Mechanical Engineering
Georgia Institute of Technology

Dr. Rigoberto Hernandez
School of Chemistry & Biochemistry
Georgia Institute of Technology

Dr. Clifford L. Henderson, Co-advisor
School of Chemical and
Biomolecular Engineering
Georgia Institute of Technology

Dr. Peter J. Ludovice
School of Chemical and
Biomolecular Engineering
Georgia Institute of Technology

Date Approved: July 18, 2005

ACKNOWLEDGEMENTS

I would like to take this opportunity to thank my advisor Dr. John Muzzy for the support and freedom he provided me to pursue this project as I envisioned it.

I would also like to thank my co-advisor, Dr. Cliff Henderson, for his advice and insight.

I appreciate being around Dr. David Rosen who pays attention to students' academic growth, from which I benefit a lot.

Thanks also go to Dr. Peter Ludovice and Dr. Rigoberto Hernandez for serving on my thesis committee.

I'm thankful to Dr. Jonathan Colton for his welcome gesture and helpful advice when I borrowed his equipment. I'd also like to mention the help from Dr. C. P. Wong and his postdoc Zhuqing Zhang for use of photo-DSC, Dr. William Koros and his graduate student William Madden for use of the density gradient column, Dr. Laren Tolbert and Kendra McCoy for use of the UV/VIS spectrometer, and Dr. Tongfan Sun for measurement of liquid thermal conductivity.

I appreciate the opportunity to work in both Henderson's and Rosen's research groups. I owe thanks to Augustin Jeyakumar for help with ellipsometer and optical microscope, Cody Berger for sharing his experience in standing wave issue, Lovejeet Singh for discussion regarding to CTE measurement, Benita Comeau and Mikkel Thomas (ECE) for use of surface profilometer, and Trevor Hoskins for being a wonderful officemate. Benay Sager (ME) has discussed with me regarding to the SLA minivat operation, Ec & Dp measurement, and other SLA problems.

It's worth mentioning the assistance from Safdar Ali and Marshall Sloane (ChBE undergraduates) as well as Andrew Mrasek (ME undergraduate) with part building in SLA 250 and dimension measurement by SEM.

It shouldn't be forgotten, either, that Ms. Yolande Berta has offered nice help regarding to SEM measurement and carbon coating unit operation, and that Jeff Andrews and Brad Parker in ChBE machine shop have kindly and carefully machined the light guide custom unit and user-designed DSC pans.

I'm lucky to have had you around, and I don't take it for granted.

TABLE OF CONTENTS

ACKNOWLEDGEMENTS	iii
LIST OF TABLES	viii
LIST OF FIGURES	x
LIST OF SYMBOLS	xiv
SUMMARY	xviii
CHAPTER 1 INTRODUCTION	1
1.1 Introduction to Stereolithography	1
1.2 Project Objective	2
1.3 Project Strategy	9
CHAPTER 2 MODEL DEVELOPMENT	11
CHAPTER 3 KINETIC CHARACTERIZATION	17
3.1 Photopolymerization Kinetic Model	17
3.2 Kinetic Experiments	27
3.2.1 DPC Pan	28
3.2.2 Standing Waves	28
3.2.3 DPC Experiments	32
3.3 Kinetic Data Analysis & Model Parameterization	35
3.4 Kinetic Model Validation	44
CHAPTER 4 MATERIAL CHARACTERIZATION	46
4.1 Specific Heat Capacity	46
4.2 Glass Transition Temperature	50
4.3 Coefficient of Thermal Expansion	52
4.4 Density	58
4.5 Thermal Conductivity	59
4.6 Heat of Polymerization	61
4.7 Absorption Coefficient	62
4.8 Summary	64
CHAPTER 5 SIMULATIONS	65
5.1 Single Laser Drawn Line	67
5.2 Overlapping Lines	74
5.3 Stacked Single Lines	78

CHAPTER 6	MODEL VERIFICATION	82
6.1	DOC Threshold Model	82
6.2	DOC Threshold Model Prediction	85
6.2.1	Single Line Part Prediction	85
6.2.2	Overlapping Line Part Prediction	88
6.2.3	Stacked Line Part Prediction.....	90
6.3	Exposure Threshold Model Prediction	91
6.3.1	Ec and Dp Determination.....	92
6.3.2	Single Line Part Prediction	93
6.3.3	Overlapping Line Part Prediction	97
6.3.4	Stacked Line Part Prediction.....	99
6.3.5	Comparison of DOC and Exposure Threshold Model.....	100
6.3.6	Model Prediction using Ec and Dp Evaluated by a Different Protocol ..	103
6.4	Summary	108
CHAPTER 7	MODEL APPLICATIONS.....	109
7.1	Parameter Effect Investigation.....	110
7.1.1	Sensitive Parameters for Width Resolution	113
7.1.2	Sensitive Parameters for Speed (Width Direction).....	118
7.1.3	Sensitive Parameters for DOC	121
7.1.4	Sensitive Parameters for Temperature Rise.....	124
7.1.5	Sensitive Parameters for Depth Resolution	127
7.2	Resolution and Speed Prediction by Regression Model	131
7.2.1	Regression Prediction Model for Depth Resolution	131
7.2.2	Regression Prediction Model for Width Resolution	132
7.2.3	Regression Prediction Model for Speed (Width Direction).....	135
7.2.4	Regression Prediction Model for Maximum DOC	138
7.2.5	Regression Prediction Model for Maximum Temperature Rise	140
7.3	Parameter Optimization	143
7.4	Parameter Analysis using Exposure Threshold Model	146
7.4.1	Parameter Significance Investigation	146
7.4.2	Parameter Optimization	150
CHAPTER 8	CONCLUSIONS & RECOMMENDATIONS.....	152
APPENDIX A	NOVECURE OUTPUT WITH 365NM FILTER (EXFO).....	155
APPENDIX B	NEGLIGIBLE HEATING EFFECT OF LIGHT IN DPC EXPEIRMENTS.....	156
APPENDIX C	A BRIEF LITERATURE REVIEW ON GEL POINT ESTIMATION	157
APPENDIX D	MINITAB REGRESSION OUTPUT OF REDUCED MODEL FOR WIDTH RESOLUTION.....	163

APPENDIX E	MINITAB STEPWISE REGRESSION OUTPUT FOR WIDTH RESOLUTION	164
APPENDIX F	REGRESSION PREDICTION MODEL FOR DEPTH RESOLUTION	165
APPENDIX G	REGRESSION PREDICTION MODEL FOR WIDTH RESOLUTION	166
APPENDIX H	REGRESSION PREDICTION MODEL FOR CURING SPEED (WIDTH)	167
APPENDIX I	REGRESSION PREDICTION MODEL FOR MAXIMUM DOC	168
APPENDIX J	REGRESSION PREDICTION MODEL FOR MAXIMUM TEMPERATURE RISE	170
REFERENCES	172

LIST OF TABLES

Table 1	Material & Process Parameters Involved in the SL Cure Process Model	26
Table 2	k_t / k_p and $k_p / k_t^{1/2}$ Values Obtained from DPC Experiments.....	37
Table 3	Determination of Rate Constants k_t and k_p	38
Table 4	Kinetic Parameter Values	42
Table 5	Characterized Material Properties	64
Table 6	Process and Laser Parameter Values Used for Simulations	67
Table 7	Dimensions of Single Line Parts Built at Two Laser-Scanning Speeds:.....	86
Table 8	Single Line Part Prediction by DOC Threshold Model.....	87
Table 9	Dimension Measurements of Overlapping Line Parts.....	89
Table 10	DOC Threshold Model Prediction for Overlapping Line Parts.....	89
Table 11	Dimension Measurements of 3-Layer Stacked Line Parts.....	90
Table 12	DOC Threshold Model Prediction for 3-Layer Stacked Line Parts.....	91
Table 13	Single Line Part Prediction Results Based on Exposure Threshold Model.....	93
Table 14	Exposure Threshold Model Prediction Results using Modified Beam Profile.	96
Table 15	Comparison of Prediction Results by Two Threshold Models.....	101
Table 16	Exposure Threshold Model Prediction (high working range): 1. Single Line (1) $V_s = 1.071$ (2) $V_s = 0.466$ in/sec, 2. Overlapping-line, and 3. Stacked-line Parts	102
Table 17	Exposure Threshold Model Prediction (protocol): 1. Single Line (1) $V_s = 1.071$ in/sec (2) $V_s = 0.466$ in/sec, 2. Overlapping-line, and 3. Stacked-line Parts ..	106
Table 18	Exposure Threshold Model Prediction (protocol; high working range): 1. Single Line (1) $V_s = 1.071$ in/sec (2) $V_s = 0.466$ in/sec, 2. Overlapping-line, and 3. Stacked-line Parts	107

Table 19	Exposure Threshold Model Prediction (protocol; low working range): 1. Single Line (1) $V_s = 1.071$ in/sec (2) $V_s = 0.466$ in/sec, 2. Overlapping-line, and 3. Stacked-line Parts	108
Table 20	Potential Sensitive Parameters and Their Level Values	111
Table 21	Significant Factors Identified from Screening Experiment	112
Table 22	Full Factorial Design and Response Values (Width Resolution)	113
Table 23	Estimated Factorial Effects and Lenth's Test for Width Resolution	114
Table 24	Estimated Factorial Effects and Lenth's Test for Speed (Width)	118
Table 25	Estimated Factorial Effects and Lenth's Test for Maximum DOC	121
Table 26	Estimated Effects and Lenth's Test for Maximum Temperature Rise	124
Table 27	Estimated Effects and Lenth's Test for Depth Resolution	127
Table 28	Significant Factors for Investigated Responses	130
Table 29	Simulation Conditions to Test Predictive Ability of Regression Models	132
Table 30	Depth Resolution Predicted by Regression Model	132
Table 31	Width Resolution Predicted by Regression Model	135
Table 32	Curing Time (Width Direction) Predicted by Regression Model	138
Table 33	Maximum DOC Predicted by Regression Model	140
Table 34	Maximum Temperature Rise Predicted by Regression Model	142
Table 35	Conditions used for Test of Temperature Rise Regression Model	142
Table 36	Parameter Range Used for Response Optimization	144
Table 37	Evolver Optimization Results for Investigated Responses	145
Table 38	Parameters in Exposure Threshold Model and Their Level Values	147
Table 39	Evolver Optimization Results using Exposure Threshold Model	150

LIST OF FIGURES

Figure 1	Complex SL Process and Oversimplified Exposure Threshold Model.....	5
Figure 2	Cured Shape of Single Laser Drawn Line.....	12
Figure 3	2D Domain for Single Laser Drawn Line	12
Figure 4	Absorbed Intensity at Point $Q(x,y,z)$	19
Figure 5	Structure Formula of E4PETeA (Sartomer)	27
Figure 6	Structure Formula of DMPA (Ciba).....	27
Figure 7	DPC Sample Pan	28
Figure 8	Standing Wave Intensity at 365nm.....	30
Figure 9	Standing Wave Intensity at 304-395nm	30
Figure 10	Isothermal DSC Runs to Detect the Onset Temperature of Thermal Cure	33
Figure 11	DPC Experimental Curves (Continuous and Flash Exposure at 50°C).....	34
Figure 12	Nonlinear Fit of Propagation Rate Constant k_p vs. Conversion X (50°C).....	40
Figure 13	Nonlinear Fit of Termination Rate Constant k_t vs. Conversion X (50°C)	40
Figure 14	Semi-log Plot of True Kinetic Constants k_{p0} and k_{t0} vs. $1/T$	41
Figure 15	Linear Fit of $1/f_c$ (Critical Fractional Free Volume) vs. $1/T$	41
Figure 16	Comparison of the Experimental and Simulated Polymerization Rate Curves (incident power = 0.1 mW): (a) 30°C, (b) 50°C, (c) 70°C.....	45
Figure 17	C_p -T Plot of Liquid E4PETeA Monomer Exported from MDSC Data.....	48
Figure 18	C_p -T Plot of Cured E4PETeA Polymer Exported from MDSC Data.....	48
Figure 19	Glass Transition of Liquid E4PETeA Monomer Detected by DSC.....	50
Figure 20	Glass Transition of Cured Poly(E4PETeA) Detected by DSC	51

Figure 21	Effect of Heating Rate on Measured T_g Value of Liquid Monomer	51
Figure 22	Effect of Heating Rate on Measured T_g Value of Cured Polymer	52
Figure 23	Temperature Dependence of Liquid E4PETeA Monomer Film Thickness	54
Figure 24	Temperature Dependence of Cured E4PETeA Polymer Film Thickness	54
Figure 25	CTEs of Poly(E4PETeA) below T_g Determined by Linear Regression of Curves Obtained by Fitting with Si Substrate Optical Data of 25°C (diamonds) and of Curves Obtained by Fitting with Temperature Dependent Si Substrate Data (triangles)	56
Figure 26	Effect of Temperature on Heat Generated by Polymerization	61
Figure 27	Absorption Coefficient Spectrum of DMPA	63
Figure 28	Three Basic Laser Drawing Patterns: Case I. Single Laser Drawn Line, Case II. Overlapping Single-Layer Lines, Case III. Stacked Single Lines	66
Figure 29	Transients of (a) Intensity, (b) Initiator Concentration, (c) Radical Concentration, (d) Monomer Conversion, and (e) Temperature at Point (x, 0, 0)	70
Figure 30	Distribution of (a) Monomer Conversion and (b) Photoinitiator Concentration upon a Single Laser Scan.....	72
Figure 31	Monomer Conversion vs. Width at the Top Surface of the Single Line Part (Plot Interval = 0.01 sec, except for t = 1860 sec).....	73
Figure 32	Monomer Conversion vs. Depth along the Centerline of the Single Line Part (Plot Interval = 0.01 sec, except for t = 1860 sec).....	73
Figure 33	(a) Monomer Conversion (b) Initiator Concentration (mol/m^3) Distributions upon Two Overlapping Scans.....	76
Figure 34	Monomer Conversion vs. Width at the Top Surface of Two-Overlapping-Line Part (Plot Interval = 0.01 sec, except for t = 1860 sec)	77
Figure 35	(a) Monomer Conversion (b) Initiator Concentration (mol/m^3) Distributions upon Two Stacked Scans.....	80
Figure 36	Monomer Conversion vs. Depth at the Centerline of Two-Layer-Line Part (Plot Interval = 0.01 sec, except t = 1860 sec)	81
Figure 37	SEM Image of Cross Section of a Single Line Part	83

Figure 38 Degree of Cure Contour for Parts Built at $V_s = 1.071$ in/sec (with the measured part contour shown in red).....	84
Figure 39 Degree of Cure Contour for Parts Built at $V_s = 10.71$ in/sec.....	88
Figure 40 Working Curve from WINDOWPANE TM Experimental Data	92
Figure 41 Beam Intensity Profile of HeCd Laser in SLA-250/50	94
Figure 42 Laser Movement when Drawing Overlapping Lines	97
Figure 43 High Working Range for Model Acrylate Resin in SLA	102
Figure 44 Comparison of Working Curves Obtained by the 3D Systems WINDOWPANE Procedure (labeled “SOP” in the figure) and by the Part Building Protocol.....	104
Figure 45 E_c and D_p Determined in the High Range using Part Building Protocol	106
Figure 46 E_c and D_p Determined in the Low Range using Part Building Protocol	107
Figure 47 Normal Plot for Width Resolution	114
Figure 48 Factorial Effects Plot for Width Resolution: (a) main effect (b) interaction.	116
Figure 49 Factorial Effects Plot for Speed (Width): (a) main effect (b) interaction.....	120
Figure 50 Factorial Effects Plot for Max DOC: (a) main effect (b) interaction	123
Figure 51 Factorial Effects Plot for Temperature Rise: (a) main effect (b) interaction	126
Figure 52 Factorial Effects Plot for Depth Resolution: (a) main effect (b) interaction.	129
Figure 53 Curvature in Factors for Width Resolution	133
Figure 54 Curvature Effect for Width Resolution: (a) main effect (b) interaction.....	134
Figure 55 Curvature in Factors for Speed (Width)	135
Figure 56 Nonlinear Behavior of Beam Radius for Speed (Width).....	136
Figure 57 Factors Curvature for Speed (Width): (a) main effect (b) interaction.....	137
Figure 58 Curvature in Factors for Maximum DOC	138

Figure 59 Factors Curvature for Maximum DOC (a) main effect (b) interaction	139
Figure 60 Curvature in Factors for Maximum Temperature Rise	140
Figure 61 Factors Curvature for Max Temp Rise (a) main effect (b) interaction.....	141
Figure 62 Main Effects Plot for Cure Depth.....	148
Figure 63 Main Effects Plot for Line Width.....	148

LIST OF SYMBOLS

A_{Ep}	Pre-exponential Factor of Propagation Rate Constant Dependence on Temperature
A_{Et}	Pre-exponential Factor of Termination Rate Constant Dependence on Temperature
A_p	Parameter of Propagation Rate Constant Dependence on Fractional Free Volume
A_t	Parameter of Termination Rate Constant Dependence on Fractional Free Volume
C_d	Cure Depth of Resin
C_p	Specific Heat Capacity
$C_{p,M}$	Specific Heat Capacity of Monomer
$C_{p,P}$	Specific Heat Capacity of Polymer
D_M	Diffusion Coefficient of Monomer
D_p	Penetration Depth of Laser into Resin
$D_{p\cdot}$	Diffusion Coefficient of Polymeric Radical
D_S	Diffusion Coefficient of Photoinitiator
E	Exposure
E_c	Critical Exposure
E_p	Activation Energy for Propagation
E_t	Activation Energy for Termination
f	Fractional Free Volume
f_{cp}	Critical Fractional Free Volume for Propagation

f_{ct}	Critical Fractional Free Volume for Termination
f_M	Fractional Free Volume of Pure Monomer
f_P	Fractional Free Volume of Pure Polymer
h	Heat Convection Coefficient
h_s	Hatch Space, i.e., the Lateral Distance between Adjacent Laser Scan Centerlines
I	Incident Laser Intensity
I_o	Laser Peak Intensity
I_a	Absorbed Light Intensity
k	Thermal Conductivity
k_D	Diffusion Limited Kinetic Constant
k_p	Rate Constant of Propagation
k_{p0}	True Rate Constant of Propagation
k_r	Reaction Limited (“true”) Kinetic Constant
k_r^*	Rate Constant of Reaction Diffusion
k_t	Rate Constant of Termination
k_{t0}	True Rate Constant of Termination
L	Average Sample Thickness Over Temperature Range
L_f	Average Free Path Length
L_w	Linewidth of the Cured Line
$[M]$	Monomer Concentration
$[M]_0$	Initial Monomer Concentration

$[P\cdot]$	Polymeric Radical Concentration
P_L	Laser Power
$Q(t)$	Heat Integral in DPC Experiment
Q_{tot}	Reference Heat of Reaction
R	Gas Constant = 8.314J/mol-K
R_i	Rate of Initiation
R_N	Normalized Rate of Propagation
R_p	Rate of Propagation
R_{rd}	Reaction Diffusion Parameter
R_t	Rate of Termination
S	Photoinitiator Concentration
t_e	Characteristic Exposure Time
T_b	SLA Resin Bath Temperature
T_{gM}	Glass Transition Temperature of Monomer
T_{gP}	Glass Transition Temperature of Polymer
T_{inf}	Ambient Temperature in SLA Chamber
U_R	Rao Function
V	Volume of Material
V_m	Molar Volume per Structure Unit of Polymer
V_s	Laser Scanning Speed
w_o	Half Width of Laser Spot (@ $1/e^2$)
X	Monomer Conversion

α	Volumetric Coefficient of Thermal Expansion
α_M	Coefficient of Thermal Expansion of Monomer
α_P	Coefficient of Thermal Expansion of Polymer
β	Linear Coefficient of Thermal Expansion
ε	Molar Absorptivity
ϕ_i	Quantum Yield of Initiation
ϕ_M	Volume Fraction of Monomer
λ	Laser Wavelength (325nm in SLA-250/50)
ν	Poisson's Ratio
ρ	Density
ρ_M	Density of Pure Monomer
ρ_P	Density of Pure Polymer
ΔH_p	Heat of Polymerization

SUMMARY

Although stereolithography (SL) is a remarkable improvement over conventional prototyping production, it is being pushed aggressively for improvements in both speed and resolution. However, it is not clear currently how these two features can be improved simultaneously and what the limits are for such optimization.

In order to address this issue a quantitative SL cure process model is developed which takes into account all the sub-processes involved in SL: exposure, photoinitiation, photopolymerization, mass and heat transfer. To parameterize the model, the thermal and physical properties of a model compound system, ethoxylated (4) pentaerythritol tetraacrylate (E4PETeA) with 2,2-dimethoxy-2-phenylacetophenone (DMPA) as initiator, are determined. The free radical photopolymerization kinetics is also characterized by differential photocalorimetry (DPC) and a comprehensive kinetic model parameterized for the model material. The SL process model is then solved using the finite element method in the software package, FEMLAB, and validated by the capability of predicting fabricated part dimensions.

The SL cure process model, also referred to as the degree of cure (DOC) threshold model, simulates the cure behavior during the SL fabrication process, and provides insight into the part building mechanisms. It predicts the cured part dimension within 25% error, while the prediction error of the exposure threshold model currently utilized in SL industry is up to 50%. The DOC threshold model has been used to investigate the effects of material and process parameters on the SL performance properties, such as resolution, speed, maximum temperature rise in the resin bath, and maximum DOC of the

green part. The effective factors are identified and parameter optimization is performed, which also provides guidelines for SL material development as well as process and laser improvement.

CHAPTER 1

INTRODUCTION

In this chapter, the stereolithography (SL) technology is introduced, the objective of this work is addressed, and the strategy to achieve the goal is demonstrated.

1.1 Introduction to Stereolithography

Stereolithography is currently the most widely used process in the rapid prototyping and manufacturing (RP&M) field. “It translates computer aided designs (CAD) into solid objects through a combination of laser, photochemistry and software technologies”¹.

A basic printing process goes like this²:

- “A 3-D model of an object is created in a CAD program.
- The software (e.g. Lightyear, 3D Systems) slices the 3-D CAD model into a series of very thin horizontal layers.
- The sliced information is transferred to an ultraviolet laser that scans the top layer of the photosensitive resin, hardening it.
- The newly built layer attached to the platform is lowered to just below the surface the distance of one layer, and a new layer of resin is then recoated and scanned on top of the previous one. This process repeats layer by layer, with successive layers bonding to each other, until the part is complete.”²

¹ ‘Stereolithography’, Conceptual Reality L.L.C., 2001, <http://conceptual-reality.com/stereo.htm>.

² ‘How Stereolithography (3-D Layering) Works’, Howstuffworks Inc., 1998-2001, www.howstuffworks.com/stereolith.htm.

“Traditional prototype production is a long, inefficient, expensive and fraught-with-inaccuracy process that adds to the ultimate cost of a product, wastes manpower and materials, and slows the production cycle”³. SL technology provides a solution to these problems inherent in the traditional approach. “It is a technological breakthrough that allows solid physical parts to be made directly from computer data in a short time using an automated process.”³

1.2 Project Objective

Although SL is a remarkable improvement over the conventional prototyping production in many aspects, it still needs further improvement in speed and resolution to meet the demands of industry. Resolution is particularly important as it indicates the minimum feature sizes and surface finish achievable.

One important factor that affects SL resolution is inherent in the nature of the laser. For example, for the case of a Gaussian laser and a resin obeying the Beer-Lambert law, the resin will cure in a shape of a parabolic cylinder upon a single laser scan vector (Jacobs, 1992). Using a smaller layer thickness can reduce this boundary effect, but it also increases the build time. Resolution can be improved by shrinking the laser beam size, but it also causes an increase in the building time. Increasing the laser intensity can improve SL speed since both the rate and degree of cure increase with the intensity (Maffezzoli et al., 1998). However, since the cure reaction is exothermic and SL resins have low thermal conductivities, the heat of reaction associated with the local photopolymerization cannot be easily dispersed. When the laser intensity is increased in order

³ ‘Benefits of Stereolithography – Higher Quality, Lower Costs’, Pure Fluid Magic Inc., 1999, www.purefluidmagic.com/sl_bene.htm.

to increase the part building speed, it also unfortunately leads to faster heat generation. Consequently, some thermally initiated polymerization might occur in the vicinity of the exposed region, which would reduce the resolution of the prototype being constructed. Furthermore, the temperature gradients built within the resin might cause considerable thermal stresses and correspondingly thermal strains, which could deteriorate the mechanical/chemical properties of the part, or even manifest themselves as part distortion.

Can these two features in the SL process, resolution and speed, be improved simultaneously or do they have to be compromised with each other? If there is an optimized solution, what are the limits for such optimization given a photosensitive material system? What are the most sensitive parameters that affect the resolution or speed? In order to answer these questions, being able to simulate and predict part shape, build time, and potential difficulties would be very beneficial.

Current models of the SL process assume that the extent of resin cure is a function of only the amount of exposure to UV radiation (Jacobs, 1992). They utilize an exposure threshold model that assumes a dose $E(x,y,z)$ that is greater than a minimum “critical exposure,” E_c , causes the resin to solidify at point (x,y,z) . Basically it derives an exposure spatial distribution in the resin, e.g. Equation (1), for a single laser drawn line (Jacobs, 1992), and substitutes E_c for $E(y,z)$, then y^* and z^* obtained (Equation 2) describe the cured shape of the part.

$$E(y, z) = \sqrt{\frac{2}{\pi}} \frac{P_L}{w_0 V_s} \exp(-2y^2 / w_0^2) \exp(-z / D_p) \quad (1)$$

$$E_c = \sqrt{\frac{2}{\pi}} \frac{P_L}{w_0 V_s} \exp(-2y^{*2} / w_0^2) \exp(-z^* / D_p) \quad (2)$$

where P_L , w_0 , and V_s are the laser power, beam radius, and scanning speed, respectively; D_p is the penetration depth of the laser into the resin, the depth where the laser intensity decreases to $1/e$ (about 36.8%) of the intensity incident at the resin surface. D_p can be expressed as $D_p = 1/(2.3\varepsilon S)$ (Jacobs, 1992), where ε and S are the absorption coefficient and concentration of the photoinitiator, respectively. A Gaussian laser and a resin obeying Beer's Law are assumed here.

This exposure threshold model is an oversimplification of the SL process. As demonstrated in Figure 1, it directly connects the exposure to the resin and the final solid part shape. It ignores an important intermediate step: reaction. Therefore, how the reaction, the resin kinetic characteristics, as well as the diffusion and thermal effects influence the size, shape and properties of parts fabricated by SL cannot be investigated by using this model. Its ability to predict the cured part outline is challenged especially when part resolution is in demand.

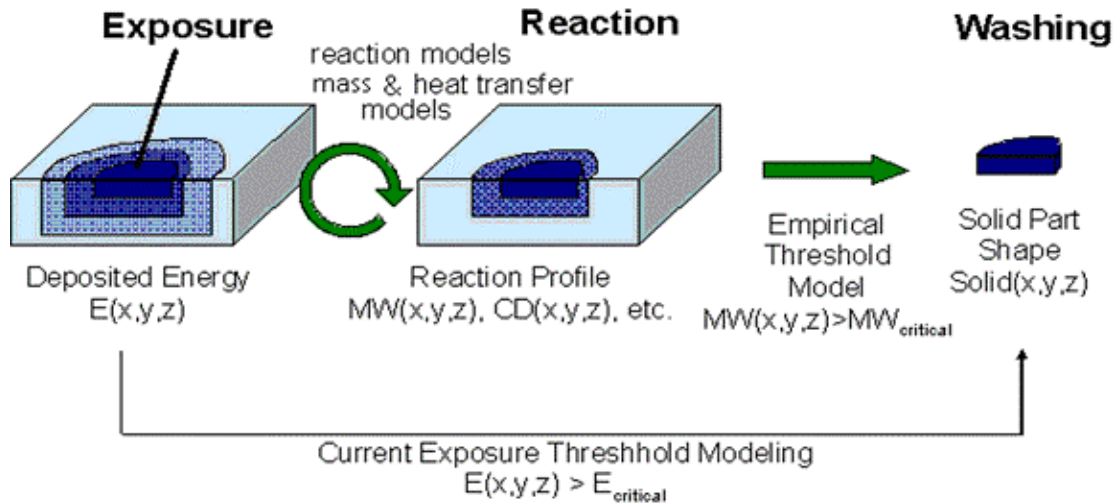


Figure 1 Complex SL Process and Oversimplified Exposure Threshold Model

Another deficiency of the exposure threshold model currently used in industry is that it also assumes the exposure is additive, i.e. when the laser draws multiple lines or layers to form a part, it simply adds all the exposure deposited in the part building process to determine the part dimensions (see section 6.3). The time delay between lines or layers is ignored as well as the chemical effects (e.g. chemical reaction, material change, etc.) during the delay. Again, the exposure threshold model is just an oversimplification of the part building process. It ignores everything (reaction, diffusion, heat, etc) but the exposure.

Saito (1993) conducted experiments varying laser power and scanning speed in SLA, and claimed a relationship which is close to the power function between the cured depth and laser scanning speed on a semi-log plot. Nagamori and coworkers (2001, 2003) performed SL curing tests to investigate how the laser power, laser beam diameter, and laser scanning speed affect the cured depth and width. They correlated the cured depth with energy density (exposure) and found a linear relation on the semi-log graph. All

these studies were trying to directly connect the laser exposure to the part dimensions, as in the exposure threshold model introduced above.

A lot of work has been done to investigate the effect of process parameters and optimize the SL process, but they are all based on the exposure threshold model currently used in industry. For example, Chockalingam and coworkers (2003) determined the part shrinkage (by comparing the SL finished part dimensions with the part dimensions on the CAD model) for an experimental set designed by genetic algorithm concerning the effects of layer thickness, hatch spacing, hatch style, hatch over cure, and hatch fill cure depth. They then performed an optimization and identified an optimal value set of these parameters to obtain parts with the same shrinkage ratio in both depth and width directions. Cho and coworkers (2000) also used a genetic algorithm based methodology to determine an optimal value set for the process parameters, such as hatch spacing, hatch overcure, border overcure, hatch fill cure depth, and layer thickness, to minimize SL part building error. Schaub and coworkers (1997) identified four key variables that affect the part dimensional accuracy among various control variables in the SL process. They then used design of experiments and the ANOVA technique to analyze and compare the significance of these four parameters, and concluded that layer thickness and part orientation have more effects on the part dimensional accuracy. Onuh and Hon (1998a) used the Taguchi method to design and conduct experiments concerning layer thickness, hatch spacing, hatch style, hatch overcure, and hatch fill cure depth. They analyzed the built results and optimized these building parameters to improve the surface finish of SL parts. Onuh and Hon (1998b) added two new hatch styles to their previous work (1998a) and studied the effects of these styles on the dimensional accuracy. Jayanthi and

coworkers (1994) performed a study on the influence of process parameters, such as layer thickness, hatch spacing, hatch overcure, and fill cure depth, on curl distortion of the cured part. This study was performed for two writing styles: hatch and weave. The ANOVA procedure was utilized to identify significant factors for each writing style, and it was concluded that the hatch writing style yields better results than weave style. All these studies took the exposure threshold model for granted, used it to control the SL part building, and analyzed the finished part property upon the variation of the process parameters.

Eschl and coworkers (1999) tested and simulated the transient post-fabrication shrinkage of SL parts to investigate the effect of the resin material type, acrylate or epoxy, on the SL cure process. They found that the epoxy resin produces more accurate parts because the stress due to shrinkage is smaller and the final stiffness is higher. Their methodology of studying material effects is based on an investigation of the built results rather than a direct study on the building process. This is a different perspective, which, however, cannot address the curing dynamics or the heating issue in SL building process.

A more complete model is needed that accounts for reaction, heat transfer and mass transfer in order to predict the cured shape and size more accurately, to investigate how the chemical effects (e.g. resin properties, cure reaction, etc.) impact the SL fabrication results, and to find the optimum combination of material and process parameters to improve SL resolution and speed.

Flach and Chartoff (1995a,b) incorporated both reaction and heat transfer into an SL process model and simulated the cure process when the laser is stationary and when it moves along one line. Mass transfer, however, was not taken into account. Their

simulation results predicted that a substantial temperature increase ($\sim 90^{\circ}\text{C}$) occurs in the resin bath under certain conditions. They also presented the profiles for monomer conversion and photoinitiator consumption in the curing process. However, no experimental verification of the model was provided. Furthermore, a systematic study of how the various SL parameters affect the SL process was not performed. Therefore, their work did not directly provide guidance on how to improve the SL process. Furthermore, the diacrylate monomer (hexanedioldiacrylate, HDDA) used in their work does not form well-made solid parts in SLA. Hur and coworkers (1997, 2000) further studied the part deformation and the thermal stress formed in the built part when the laser is stationary and moves along one line. However, in addition to suffering from the deficiencies in Flach and Chartoff's work (1995), their work also ignored the dark polymerization reaction in the case of the laser moving.

In this study, a tetraacrylate monomer is used for both simulation and part building in SLA. Its material properties and photopolymerization kinetics are characterized. The process model established incorporates both an energy balance and mass balances for multiple species. Since the chemical reactions are taken into account upon transient irradiation, the new model discards the additive exposure assumption used by the current exposure threshold model. The SL cure process is simulated and the process modeling is verified experimentally. For several responses that characterize the SL performance, such as temperature rise in the SLA vat, part resolution, and green part degree of cure, significant factors which affect each of these responses are identified and optimized.

1.3 Project Strategy

In this work, a complex SL cure process model is established that captures effects that are ignored in the exposure threshold model. It incorporates laser exposure, photoinitiation, polymer chain propagation and termination, species diffusion in the curing polymer network, and heat transfer via conduction in the exposed region and its vicinity. This model investigates during the part building process the spatial and temporal distributions of temperature, rate of polymerization, and degree of cure (DOC), which are necessary to characterize the cured part. It gives a full description of the transient cure behavior of the resin in the SLA bath, as well as a prediction of the cure behavior upon the variation of material or process parameters. Therefore, a fundamental understanding of the SL process that takes into account the detailed physics and chemistry of the underlying process can be expected; the material and process modifications can be made for SL technology improvement; and the SL applications which are currently limited by poor prediction of the exposure threshold model can be activated. Additionally, the sensitivity analysis of material parameters provides a guideline for developing new photosensitive SL resins.

In Chapter 2, the SL cure process model is formulated as a set of coupled partial differential equations describing mass and energy transport during the curing process, incorporating exposure and dark reaction in one model. In Chapter 3, the photopolymerization kinetics are characterized using differential photocalorimetry (DPC) and a comprehensive kinetic model is parameterized for a model acrylate resin system. The thermal and physical properties of the model material are characterized in Chapter 4. Chapter 5 demonstrates the simulation results by solving the process model using the

finite element method with the software package FEMLAB (Comsol Inc.). Chapter 6 verifies the process model through part fabrication and measurement. In Chapter 7, significant material and process parameters are identified and optimized for SL resolution and curing speed. Conclusions and recommendations are made in Chapter 8.

CHAPTER 2

MODEL DEVELOPMENT

The simplest case of complex laser drawing patterns in SL is that the laser moves along one direction and draws a single vector line. For a Gaussian laser and a resin obeying Beer's law used in this work, the cured shape upon a single laser drawn line is a parabolic cylinder (Jacobs, 1992), as shown in Figure 2, where the x axis is the laser moving direction. Considering the repetitive cure behavior along the x-axis (the very ends of the line which may receive different amount of exposure are not of interest here), only the cross section of the parabolic cylinder needs to be modeled. The heat and mass transfer along x direction can be ignored due to infinitely small behavior difference between neighboring planes (cutting the parabolic cylinder into infinite number of parabolic planes) as well as low thermal conductivity and diffusion coefficients of the curing system. A 3-dimensional problem is thus reduced to a 2-dimensional one. Furthermore, since the cross section is symmetric about z axis, only a half section needs to be modeled. This leads to a 2-dimensional rectangular domain in Cartesian coordinate (Figure 3) which is used to simulate the resin cure behavior during the single line drawing process.

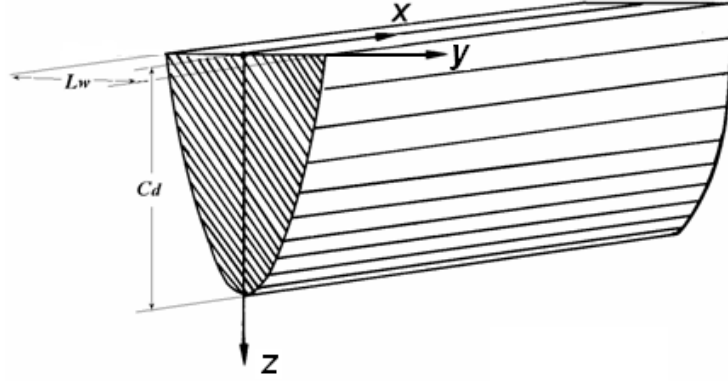


Figure 2 Cured Shape of Single Laser Drawn Line

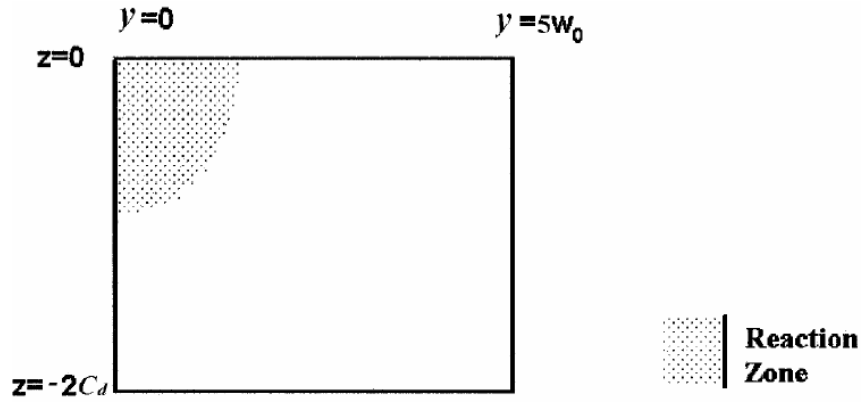


Figure 3 2D Domain for Single Laser Drawn Line

The shaded region in Figure 3, which corresponds to the half cross section of the parabolic cylinder in Figure 2, is where most of the reaction occurs and the material properties vary significantly. The size of this region increases with time as heat conduction and/or molecular diffusion continues (Flach and Chartoff, 1995a). The domain is chosen to be large enough to ensure ambient temperature and concentrations outside the rectangle at any time.

Mass transfer by diffusion and heat transfer by conduction are the two transport phenomena occurring in the SL cure process. Equation (3) is the energy balance of the curing system. Equations (4)-(6) describe mass balances for monomer, polymeric radicals (including monomer radicals), and photoinitiator, respectively. R_i , R_p , and R_t are the rate of initiation, propagation, and termination, respectively; ϕ_i is the quantum yield of initiation.

$$\rho C_p \frac{\partial T}{\partial t} = k \left\{ \frac{\partial^2 T}{\partial x^2} + \frac{\partial^2 T}{\partial y^2} + \frac{\partial^2 T}{\partial z^2} \right\} + \Delta H_p R_p \quad (3)$$

$$\frac{\partial [M]}{\partial t} = D_M \left\{ \frac{\partial^2 [M]}{\partial x^2} + \frac{\partial^2 [M]}{\partial y^2} + \frac{\partial^2 [M]}{\partial z^2} \right\} + (-R_p) \quad (4)$$

$$\frac{\partial [P\bullet]}{\partial t} = D_{P\bullet} \left\{ \frac{\partial^2 [P\bullet]}{\partial x^2} + \frac{\partial^2 [P\bullet]}{\partial y^2} + \frac{\partial^2 [P\bullet]}{\partial z^2} \right\} + (R_i - R_t) \quad (5)$$

$$\frac{\partial S}{\partial t} = D_s \left\{ \frac{\partial^2 S}{\partial x^2} + \frac{\partial^2 S}{\partial y^2} + \frac{\partial^2 S}{\partial z^2} \right\} + (-R_i / \phi_i) \quad (6)$$

These equations are coupled with one another through the reaction terms as source(s) or sink(s) and have to be solved simultaneously. The photopolymerization mechanism and kinetics will be addressed in Chapter 3.

As shown in Equation (3) the heat generated by steps other than propagation is assumed to be negligible. The heating effect of the laser (325nm wavelength) is

negligible ($\sim 10^1$ J/mol or less) due to the low absorption of the curing resin (except the photoinitiator) and very short exposure time. It can be safely ignored when compared with the large amount of heat generated by reaction ($\sim 10^5$ J/mol).

To take shrinkage effect into account, the convection term should also be incorporated into Equations (3)-(6). Only diffusion and heat conduction phenomena are considered here due to the minor difference (within 6%) between the density of liquid monomer and cured polymer.

Attention should be paid when the assumption is made that the propagation and termination only occurs in the dark. Although the exposure time for the resin is very short in SL (~ 20 ms in this study), this assumption is not valid for the photosensitive material system studied in this work. The later simulation results demonstrate that significant reactions and material property variations occur during this 20ms. Therefore, in Equation (5) the source/sink term can not be limited to R_t which only describes the radical reaction in the dark. The radical initiation rate R_i has to be incorporated in order to take the exposure reaction into account. Since R_i is proportional to the irradiance I , it is beneficial to develop a time-varying description of I which integrates the two periods that any point would go through (irradiation and dark) into one equation — Equation (7). A time parameter t_0 is introduced into the equation so that when time t goes from 0 to $+\infty$, I increases to a maximum (the investigated point is directly irradiated) and then decreases till zero (the beam moves away from the investigated point). As the laser moves from $-\infty$ to $+\infty$ along x direction, any point (x,y,0) only receives limited time of exposure, which

in SL is defined as characteristic exposure time and expressed as $t_e = 4.3w_o / V_s$ (Jacobs, 1992). Any value greater than half t_e can be used as t_0 .

$$I = I_0 \exp\left\{-2\left[\left(V_s(t-t_0)\right)^2 + y^2\right]/w_o^2\right\} \exp(-z/D_p) \frac{\lambda(\text{nm})}{1.196 \times 10^8} \quad (7)$$

where y and z axes are as shown in Figure 2, I_0 (W/m^2) is the maximum intensity incident at the resin surface, $\lambda(\text{nm})$ is the laser wavelength, and the last quotient term is adopted to convert the unit of intensity from W/m^2 to $\text{mol}/\text{m}^2\text{-s}$.

Neglecting the insignificant property variations along the laser scanning direction (x axis) (Figure 2), the terms containing x variations can be removed from Equations (3)-(6). The initial and boundary conditions corresponding to this 2D problem are established as follows:

$$\begin{aligned} [Q] &= [Q]_i \quad \text{at } t = 0, 0 \leq y \leq 5w_o, -2C_d \leq z \leq 0 \quad (\text{a}) \\ \frac{\partial Q}{\partial y} &= 0 \quad \text{at } y = 0, -2C_d \leq z \leq 0, t \geq 0 \quad (\text{b}) \\ [Q] &= [Q]_0 \quad \text{at } y = 5w_o, -2C_d \leq z \leq 0, t \geq 0 \quad (\text{c}) \\ \frac{\partial Q}{\partial z} &= 0 \quad \text{at } z = 0, 0 \leq y \leq 5w_o, t \geq 0 \quad (\text{d}) \\ [Q] &= [Q]_0 \quad \text{at } z = -2C_d, 0 \leq y \leq 5w_o, t \geq 0 \quad (\text{e}) \end{aligned} \quad (8)$$

where Q represents temperature T , monomer concentration $[M]$, polymeric radical concentration $[P\bullet]$, or photoinitiator concentration S ; their initial values are equivalent to their boundary values $[Q]_i = [Q]_0$. C_d is cure depth, the maximum depth of the solidified area (Jacobs, 1992); w_o is the laser beam radius. The domain size is initially set based on

the values of C_d and w_0 and adjusted accordingly to accommodate the transient variations of the simulated properties.

For the temperature condition at $z=0$ boundary, heat transfer with the natural air environment in the SLA chamber can be incorporated by replacing the temperature condition (8d) with the following:

$$k \frac{\partial T}{\partial z} = h(T_{inf} - T) \quad \text{at } z = 0, 0 \leq y \leq 5w_o, t \geq 0 \quad (9)$$

where k is thermal conductivity of the curing resin system, h and T_{inf} are the air-resin heat transfer coefficient and ambient temperature in the SLA chamber, respectively. The later simulation results show that the heat convection at the resin surface in the SLA chamber doesn't have a noticeable effect on the part building results.

In order to solve the governing equations (3)-(6), the reaction dependent source/sink terms need to be defined. The kinetic model and its parameterization are detailed in Chapter 3.

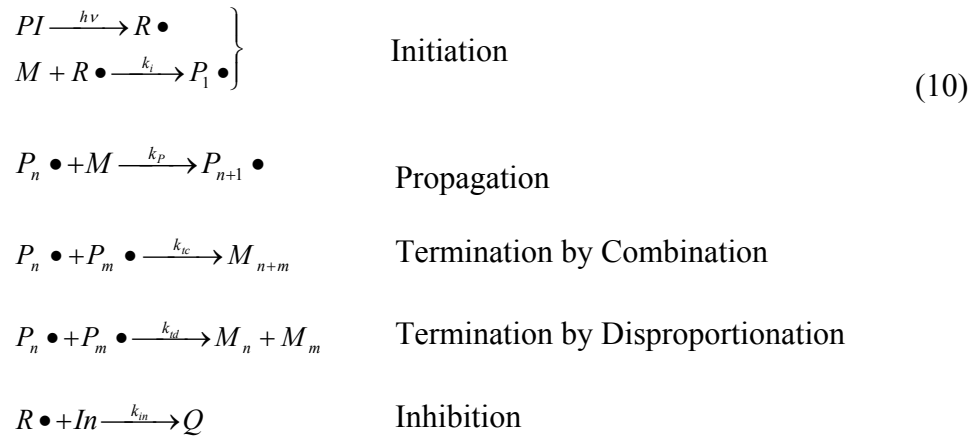
CHAPTER 3

KINETIC CHARACTERIZATION

In this chapter, a kinetic model of photoinitiated free radical polymerization is described, the kinetic experiments are designed, the kinetic coefficient data are extracted without using steady state assumption, a curve fitting method is utilized to analyze the kinetic data, and the kinetic model is parameterized and validated for a photosensitive acrylate system.

3.1 Photopolymerization Kinetic Model

As discussed in Chapter 2, all source/sink terms in the balance equations are related to the resin cure kinetics. Ignoring chain transfer reactions, the photocure mechanism for acrylate resin can be briefly described as follows:



where PI , M , and In represent the photoinitiator, monomer, and inhibitor, respectively; $R\bullet$ is the primary radical, $P_n\bullet$ the polymeric radical with a chain length of n monomer units, and M_n the stable polymer molecule with a chain length of n monomer units.

Correspondingly, the rates of initiation, propagation and termination are expressed as Equations (11), (12), and (13), respectively.

$$R_i = \phi_i I_a \quad (11)^4$$

$$R_p = k_p [P\bullet][M] \quad (12)$$

$$R_t = k_t [P\bullet]^2 \quad (13)$$

where k_p and k_t are the rate constants for propagation and termination; $[P\bullet]$ and $[M]$ are the polymeric radical concentration and monomer concentration; and I_a is the absorbed light intensity or rate of absorption ($\text{mol}/\text{m}^3\text{-s}$). For a resin obeying Beer's Law, the expression of the absorbed intensity at any point $Q(x,y,z)$ (Figure 4) can be derived as in Equation (14). I is the intensity incident on the resin surface ($\text{mol}/\text{m}^2\text{-s}$), and ε ($\text{m}^3/\text{mol-m}$) and S (mol/m^3) are the absorptivity and concentration of the initiator.

$$I_a(x, y, z) = \lim_{\Delta x, \Delta y, \Delta z \rightarrow 0} \frac{I(x, y, z)\Delta x\Delta y - I'(x, y, z)\Delta x\Delta y}{\Delta x\Delta y\Delta z} = \lim_{\Delta z \rightarrow 0} \frac{I(x, y, z)(1 - e^{-2.3\varepsilon S\Delta z})}{\Delta z} = 2.3\varepsilon SI(x, y, z) \quad (14)$$

⁴ (Fouassier, 1995; Crivello, 1998)

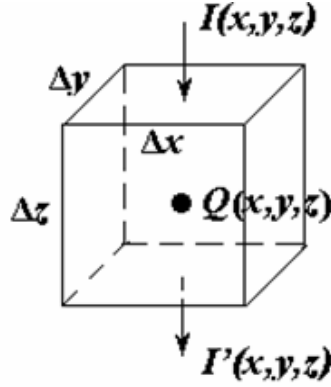


Figure 4 Absorbed Intensity at Point $Q(x,y,z)$

Fouassier (1995) has claimed that the absorbed light intensity can be expressed as:

$$I_a = I(1 - e^{-2.3\epsilon S l}) \quad (15)$$

where l is taken as 1cm in order for I_a to have the unit of photons/cm³-s. This always gives the absorbed intensity at a point 1cm lower than where the light is incident on, i.e. for an irradiance at point (x, y, z) : $I(x, y, z)$, $I_a(x, y, z + 1\text{cm})$ rather than $I_a(x, y, z)$ is evaluated. Equation (14), however, eliminates this spatial inconsistency.

The rate of initiation thus can be rewritten as:

$$R_i = 2.3\phi_i \epsilon S I \quad (16)$$

The decay of the photoinitiator can be approximated as:

$$\frac{dS}{dt} = -I_a = -2.3\varepsilon SI \quad (17)$$

The temperature dependence of the kinetic constants, k_p and k_t , is assumed to follow the Arrhenius form. The reaction is faster at higher temperature.

$$k_p = A_{Ep} e^{-E_p / RT} \quad (18)$$

$$k_t = A_{Et} e^{-E_t / RT} \quad (19)$$

where A_{Ep} and A_{Et} are pre-exponential factors, E_p and E_t are activation energies for propagation and termination, respectively, and R is the gas constant.

During the polymerization, the reaction is expected to accelerate due to the temperature rise caused by the heat of reaction; however, this is not what happens throughout the reaction. Due partially to the consumption of monomers and radicals, a rate decrease is observed in both propagation and termination reactions. Another reason for this is the decrease of the rate constants themselves. The rate constants are not only dependent on temperature but on the free volume of the reacting system. With the polymerization going on, the curing system becomes more viscous, the free volume decreases, and the mobility of the reacting species is reduced. The reaction becomes diffusion controlled. At the same temperature, the values of k_p and k_t are expected to be larger in an environment with more free volume and less diffusion limitation.

Marten and Hamielec (1979, 1982) related the kinetic constants k_p and k_t directly to

the diffusion coefficients of monomer and polymer radicals, respectively, with a temperature dependent proportionality constant. They assumed distinct regions exist for reaction and diffusion controlled polymerization, and divided the course of reaction into three conversion intervals to evaluate k_p and k_t . Bowman and Peppas (1991) adopted the same idea and coupled these intervals with volume relaxation during polymerization. These models don't take any transition region into account and the parameters have to switch to different values in different conversion ranges, i.e. each stage in the polymerization has to be treated separately. This problem has been solved by combining the reaction-controlled rate constants for propagation and termination and the diffusion-controlled mechanisms to incorporate the transition regions for both k_p and k_t . The rate constants k_p and k_t are expressed in terms of reaction resistances (Anseth and Bowman, 1993).

$$\frac{1}{k_p \text{ or } k_t} = \frac{1}{k_r} + \frac{1}{k_D} \quad (20)$$

where k_r is the reaction limited ("true") kinetic constant, and k_D is the diffusion limited kinetic constant.

For propagation, the resistances to reaction simply come from the reaction itself and the monomer diffusion. For termination, the diffusion resistance is not only from the translational and segmental diffusion of polymer radicals ($\frac{1}{k_D}$, translational diffusion is

negligible for highly crosslinked chains), but from the reaction diffusion ($\frac{1}{k_r^*}$, parallel to the segmental diffusion resistance).

$$\frac{1}{k_t} = \frac{1}{k_r} + \frac{1}{k_r^* + k_D} \quad (21)$$

According to Buback et al. (1989) and Buback (1990), the concept of reaction diffusion has been put forward by Schulz (1956) and has been refined and put into quantitative terms by several groups. The reaction diffusion is inherently a propagation step – the “frozen” polymer radical propagates via the reactive monomer matrix until encountering a second macroradical, which is also called “residual termination”. The rate coefficient of this process, k_r^* , is proportional to k_p and to monomer concentration $[M]$. The proportionality constant R_{rd} (called reaction diffusion parameter) is independent of temperature, pressure, and conversion (Buback et al., 1989; Buback, 1990).

$$k_r^* = R_{rd} k_p [M] \quad (22)$$

Anseth and Bowman (1993) assumed the diffusion limited kinetic constant k_D to be proportional to the diffusion coefficient of the reacting species and modeled it using the Doolittle equation (Bueche, 1962). Equations (18) and (19), the expressions of k_p and k_t without diffusion consideration, define the true kinetic constant k_r for propagation and the true kinetic constant k_t for termination, respectively. Substituting all the above

information into Equations (20) and (21), the dependencies of the rate constant (k_p or k_t) on both temperature and fractional free volume are incorporated into one equation (Goodner et al., 1997, 1998, 1999, and 2002) which describes the rate of propagation or termination throughout the whole polymerization course without changing parameter values.

$$k_p = \frac{k_{p0}}{1 + e^{A_p(1/f - 1/f_{cp})}} \quad (23)$$

$$k_t = \frac{k_{t0}}{1 + \frac{1}{R_{rd}k_p[M]/k_{t0} + e^{-A_t(1/f - 1/f_{ct})}}} \quad (24)$$

with

$$k_{p0} = A_{Ep} e^{-E_p/RT} \quad (25)$$

$$k_{t0} = A_{Et} e^{-E_t/RT} \quad (26)$$

where k_{p0} and k_{t0} are the true kinetic constants for propagation and termination, respectively, f is the fractional free volume of the curing system, f_{cp} and f_{ct} are critical fractional free volumes for propagation and termination, respectively, and A_p and A_t are parameters that determine the rate at which the propagation and termination rate constants decrease in the diffusion-controlled region (Goodner et al., 1997, 2002). When the free volume of the polymerization system is much larger than the critical free volume,

there is no diffusion limitation on propagation or termination, Equation (23) or (24) is reduced to Equation (18) or (19). The free volume decreases with the curing reaction going on. When it decreases to be smaller than the critical free volume, the reaction (propagation or termination) becomes diffusion limited. The diffusion resistances have to be incorporated in the kinetic constants as in Equations (23) and (24).

For a curing system comprised of pure monomer and pure polymer, the fractional free volume f is related to monomer conversion X as follows (Goodner et al., 1997, 2002):

$$f = f_M \phi_M + f_P (1 - \phi_M) \quad (27)$$

$$f_M = 0.025 + \alpha_M (T - T_{gM}) \quad (28)$$

$$f_P = 0.025 + \alpha_P (T - T_{gP}) \quad (29)$$

$$\phi_M = \frac{1 - X}{1 - X + \frac{\rho_M}{\rho_P} X} \quad (30)$$

In the above equations, f_M and f_P are the fractional free volumes of pure monomer and pure polymer, ϕ_M is the volume fraction of monomer, and the α 's, T_g 's, and ρ 's are the volumetric coefficients of expansion, glass transition temperatures, and densities, respectively, of pure monomer and pure polymer. The free volume of the polymerization system is dependent on both temperature and composition (conversion).

Goodner and Bowman (2002) also described the critical fractional free volume for propagation or termination as a function of temperature:

$$\frac{1}{f_c} = \frac{1}{f_c^{ref}} + \frac{E}{AR} \left(\frac{1}{T} - \frac{1}{T^{ref}} \right) \quad (31)$$

From the kinetic model described above and the SL process model established in Chapter 2, all the parameters (except the kinetic ones) involved are listed in Table 1. The process & laser parameters can be recorded during the SL part building (as shown in Chapter 5). The determination of material properties will be addressed in Chapter 4. The kinetic experiment has been conducted and the kinetic model for a model material system parameterized in sections 3.2 and 3.3, respectively.

Table 1 Material & Process Parameters Involved in the SL Cure Process Model

	Parameters	Symbols	Units
Process Parameters	laser scanning velocity	V_s	m/s
	bath temperature	Tb	K
	thermal convection coefficient	h	W/m ² -K
	chamber temperature	Ta	K
Laser Parameters	laser power	P _L	W
	wavelength	λ	nm
	beam radius	w_o	m
Material Properties	thermal conductivity	k	W/m-K
	heat of polymerization	ΔH_P	J/mol
	absorptivity (initiator)	ε	m ³ /mol-m
	initiation quantum yield	ϕ_i	
	diffusion coefficient (monomer)	D _M	m ² /s
	diffusion coefficient (radical)	D _{P.}	m ² /s
	diffusion coefficient (initiator)	D _S	m ² /s
	coefficient of thermal expansion (monomer)	α_M	1/K
	coefficient of thermal expansion (polymer)	α_P	1/K
	glass transition temperature (monomer)	Tg _M	K
	glass transition temperature (polymer)	Tg _P	K
	heat capacity (monomer)	C _{PM}	J/kg-K
	heat capacity (polymer)	C _{PP}	J/kg-K
	density (monomer)	ρ_M	kg/m ³
	density (polymer)	ρ_P	kg/m ³
Resin Compositions	monomer concentration	[M]	mol/m ³
	initiator concentration	[S]	mol/m ³

3.2 Kinetic Experiments

In order to simulate the polymerization behavior in the SLA bath, a model material system is identified and its kinetics characterized. Representative of the acrylate compounds commonly used in SL (Steinmann et al., 1995, 1999; Pang et al., 2000; Melisaris et al., 2000), Ethoxylated (4) PentaErythritol TetraAcrylate (E4PETeA, SR®494, Sartomer) was chosen as the model compound. The 2,2-dimethoxy-2-phenylacetophenone (DMPA, Irgacure®651, Ciba) was selected as its initiator. The inhibitor was removed from the received E4PETeA by a prepacked inhibitor remover column (Aldrich). 0.2wt% DMPA was added in the acrylate.

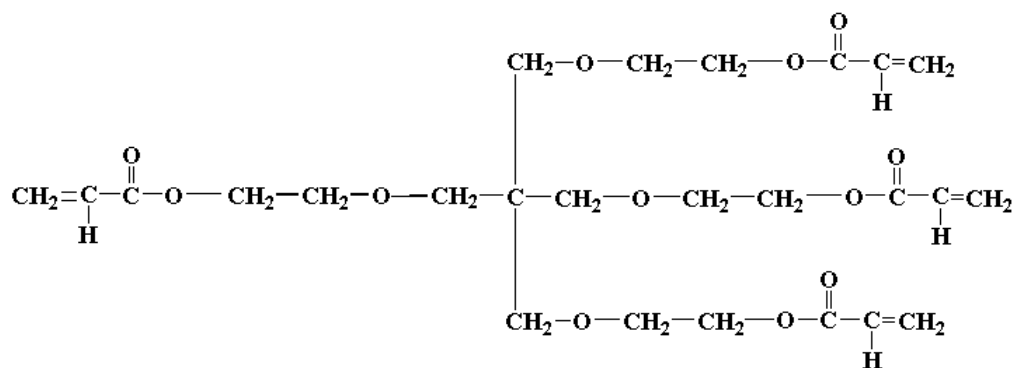


Figure 5 Structure Formula of E4PETeA (Sartomer)

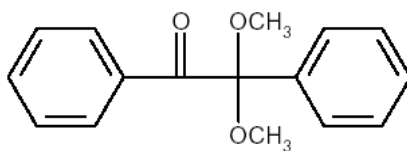


Figure 6 Structure Formula of DMPA (Ciba)

3.2.1 DPC Pan

The differential photocalorimetry (DPC) technique was used to monitor the photopolymerization kinetics. The aluminum pans were machined specially to have a 0.15mm depression to hold the sample. The sample size was determined accordingly to fill the depression, by which the thickness uniformity is ensured (Tryson and Shultz, 1979). The depth of the depression was proved small enough for heat to dissipate quickly so that the temperature uniformity through the sample can be assured.

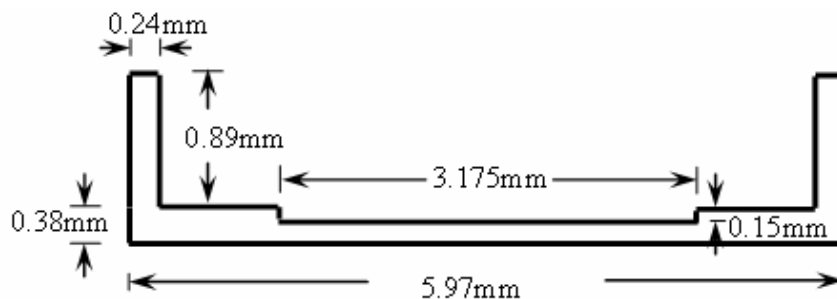


Figure 7 DPC Sample Pan

3.2.2 Standing Waves

To ensure uniform reaction occurring in DPC so that diffusion and heat conduction can be ignored in the mass and energy balance, the uniformity of light intensity through the sample thickness also has to be assured. Considering the reflectivity of the aluminum pan, the light absorption of the photosensitive sample is not the only factor that affects the intensity uniformity. When the light is incident on the sample surface, the transmitted light travels through the sample thickness and strikes the aluminum substrate, the reflectivity of which is 0.9642 (Bass et al., 1985). Therefore, most of light is reflected off the aluminum and travels through the sample again to the top surface, where the

reflection by the air-sample interface makes the light travel down into the sample and then reflected by the aluminum. This process continues until the light wave dies out due primarily to absorption. The waves traveling in opposite directions form a standing wave in the sample. The intensity of the standing wave is the intensity that exposes the sample, which takes not only the absorption but reflection into account. Mack (1985, 1986, and 1994) addressed in detail how the standing wave is formed in a thin film of absorbing material coated on a reflective substrate and described its intensity quantitatively.

According to the equation by Mack (1985, 1986, and 1994), the electric field of the light in the photosensitive sample on a reflective substrate can be calculated. The intensity that exposes the sample can be obtained by squaring the magnitude of the electric field (Mack, 1986). The magnitude of the standing wave intensity can be different from material to material, depending mainly on the absorptivity and thickness of the photosensitive material. Figures 8 and 9 demonstrate the standing wave intensity through a 150 μ m thick sample (E4PETeA with 0.2wt% DMPA) contained in the aluminum pan. Figure 8 shows the variation of the intensity at 365nm wavelength through the sample thickness; Figure 9 sums the intensities at individual wavelengths from 304 to 395nm. This wavelength range is where DMPA absorbs (Chapter 4) and the light source irradiates (Appendix A). The standing wave intensity outside the material absorption range is not of interest since it doesn't contribute to the polymerization initiation.

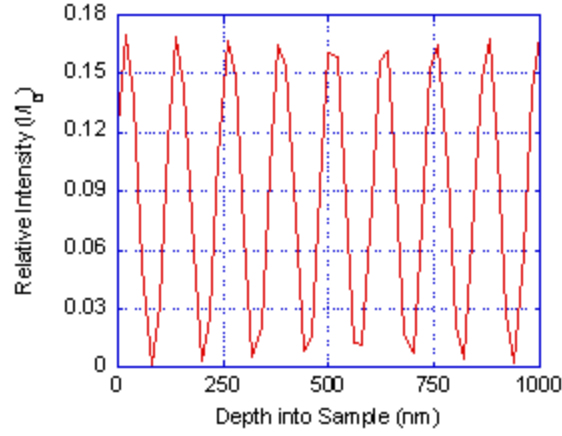


Figure 8 Standing Wave Intensity at 365nm

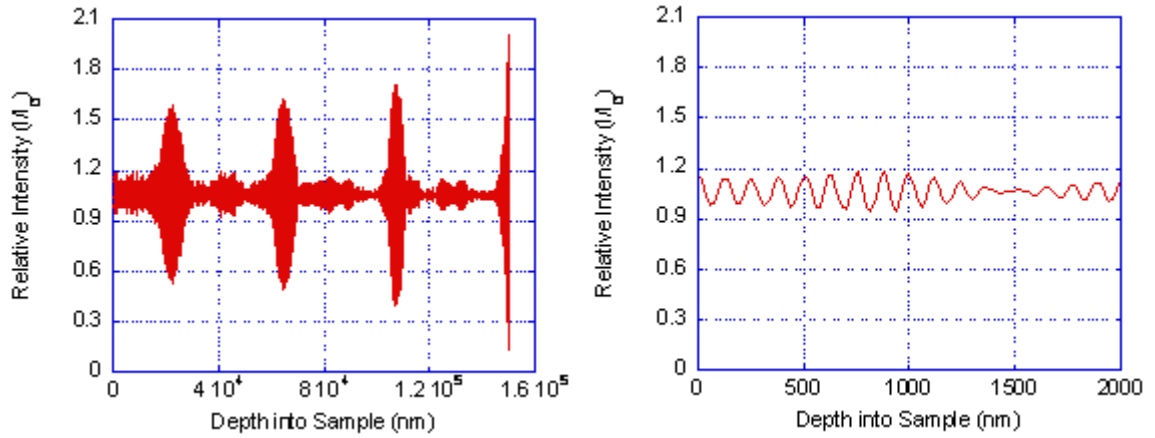


Figure 9 Standing Wave Intensity at 304-395nm

Obviously, the light intensity varies with depth into the sample. From Figure 9, it can be seen that for the investigated curing system the average of the light intensities (304-395nm) over depth is $1.15I_0$ (I_0 is the intensity incident at the sample top surface). Assuming reciprocity, the cure result under the standing wave intensity (Figure 9) should be the same as that under uniform intensity $1.15I_0$ through the sample thickness.

If the pan bottom doesn't reflect, according to the Beer's Law, the intensity of $0.93I_0$ would be expected at the bottom surface (150 μ m depth). In this case the top surface

intensity I_0 can be taken as the intensity the sample receives through the thickness (negligible light attenuation). Most published work involving DPC experiments took this assumption, ignoring the aluminum reflection and sample absorption. The aluminum reflection as well as the reflection from the sample-air interface, however, causes standing wave formed in the sample, the intensity of which as discussed above is more than 10% different from the top surface intensity I_0 .

Anseth (1994a) and Mateo (1997) and their coworkers took the reflection of the aluminum pan into account, but they assumed the sample only received two doses, one dose from the incident beam and a second dose from the reflected beam by the aluminum, and came up with $(1+0.9642)I_0$ for the intensity that exposes the sample in the pan (Recall the aluminum reflectance is 0.9642). These two light waves interfere with each other, the electric field being the sum of them. The intensity, however, is not a simple sum. The intensity is the square of the magnitude of the electric field for plane waves (Mack, 1994). Furthermore, as described earlier, rather than one single reflected wave, there are an indefinite number of reflected waves bouncing up and down in the sample and a standing wave is formed. The average intensity the resin receives was found to be 15% (not 96.42%) higher than the top surface intensity. The consideration of aluminum reflection by simply adding intensities of two doses together deviated even further away from the intensity the sample actually receives than the adoption of top surface intensity without reflection consideration.

3.2.3 DPC Experiments

1.16(\pm 0.05)mg sample was put in the aluminum pan using a micropipette to cover the 0.15mm deep depression. The differential scanning calorimeter DSC Q1000 with photo calorimetric accessory (TA Instruments) was adopted to monitor the photopolymerization of the model acrylate resin. The light source Novacure 2100 (EXFO Photonic Solutions) was used with filtered wavelength at 365nm (Appendix A). The incident power was adjusted and measured to be 0.06mW. In order for the intensity measured to be exactly the intensity incident on the sample surface in the actual experiment, a custom mount for the power probe (PM3, used with laser power meter EPM 2000e, Molectron) and twin light guides of the light source was designed and machined to simulate the DSC cell environment.

The model material system developed here can also be thermally initiated and polymerized. A set of isothermal DSC experiments demonstrate that the material won't be initiated thermally below 140°C (Figure 10). DPC experiments should be performed below this temperature to avoid thermal polymerization. Note that the heat flow oscillation in the initial stage represents the temperature overshooting and equilibration behaviour. The big exothermal peak in 140°C DSC curve, indicating the heat of polymerization, illustrates that the polymerization can be thermally initiated at and above this temperature. The absence of this peak in 130°C DSC curve shows that the material system won't polymerize at or below 130°C.

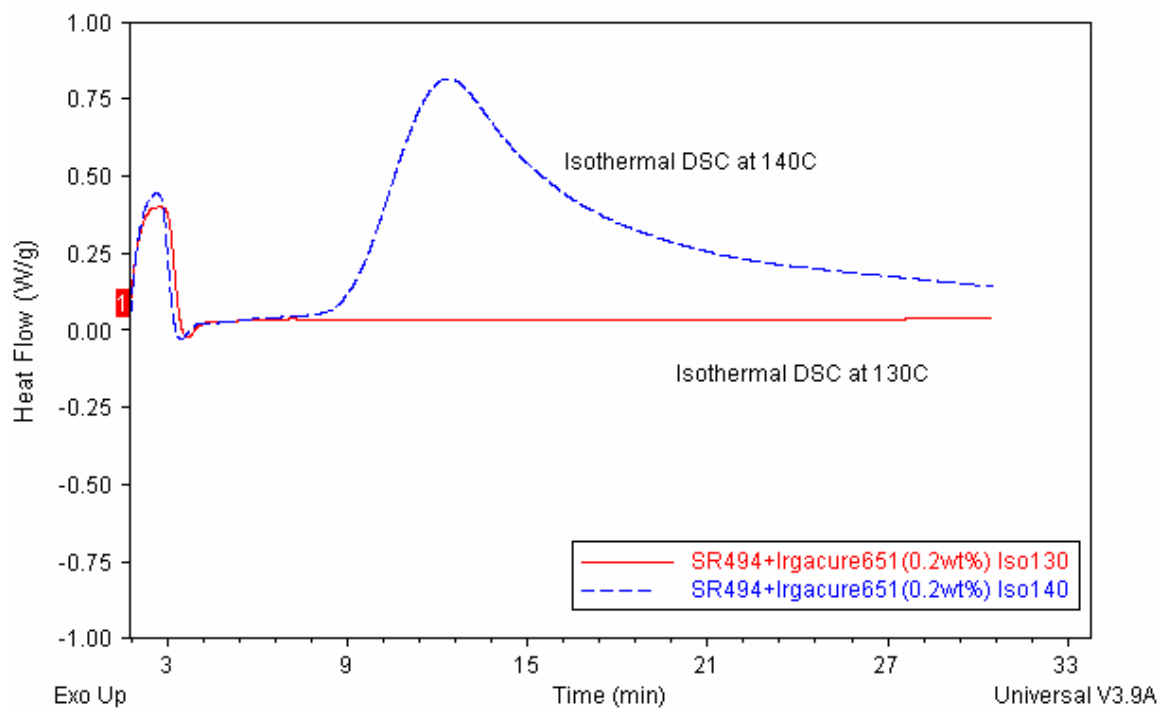


Figure 10 Isothermal DSC Runs to Detect the Onset Temperature of Thermal Cure

In this study, limited by the liquid light guide requirement on temperature, the DPC experiments cannot be conducted above 70°C. Both continuous and flash exposure experiments were carried out isothermally at three different temperatures (30, 50, 70°C). During the continuous irradiation experiment, the light is on until the heat flow curve drops to the baseline, i.e. the reaction is complete under the current temperature. The light is on only for a very short time in flash exposure experiments. For each temperature, five or more different flash times were used in order to extract the kinetic constants at different conversions. A typical set of experimental data is shown in Figure 11.

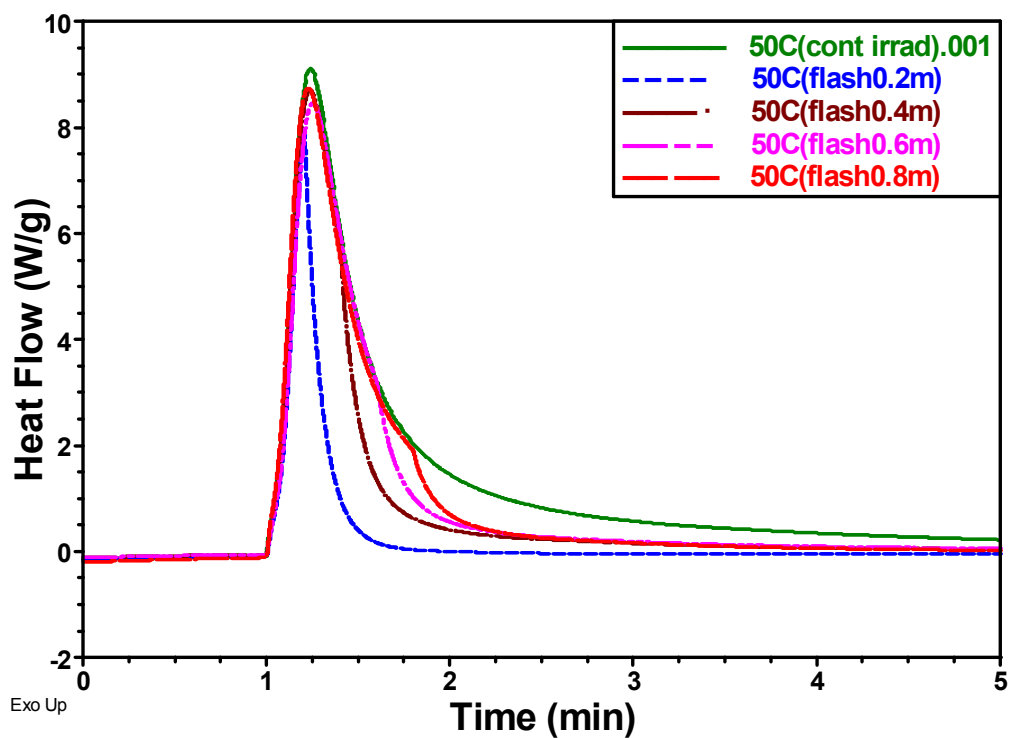


Figure 11 DPC Experimental Curves (Continuous and Flash Exposure at 50°C)

The heat flow curves are only contributed by the reaction generated heat. As shown in Appendix B, after the reaction is completed, no noticeable change in heat flow curve is observed when the light is turned off. This demonstrates that the heating effect of the DPC light source is negligible (Lecamp et al., 1997). A quantitative estimation also shows that the heating by light is insignificant ($\sim 10^0$ J/mol for continuous irradiation and 10^{-1} J/mol for very short time exposure) comparing with the heat generated by reaction ($\sim 10^5$ J/mol for continuous irradiation and 10^4 J/mol for very short time exposure).

3.3 Kinetic Data Analysis & Model Parameterization

Assuming that the heat produced by the reaction is proportional to the amount of monomer reacted (Burel et al., 1999, Cook, 1992, 1993, Lecamp et al., 1997, 1999, and Maffezzoli and Terzi, 1995, 2001), the degree of cure, X , in DPC experiments can be defined as follows:

$$X = \frac{Q(t)}{Q_{tot}} \quad (32)$$

Correspondingly, the rate of propagation normalized by the initial monomer concentration is expressed as follows (the monomer consumption by initiation, ignored in Equation 33, is negligible compared with the consumption during propagation):

$$R_N = \frac{R_p}{[M]_0} = \frac{dX}{dt} = \frac{dQ}{dt} \times \frac{1}{Q_{tot}} \quad (33)$$

where $Q(t)$ is the heat developed at any time t during a DPC measurement, which is the integration of the heat flow signal $\frac{dQ}{dt}$. Q_{tot} is in principle the total heat of reaction when all the monomers are converted. Q_{tot} is approximately the heat of polymerization measured at high enough temperature and light intensity.

For the dark reaction in the flash exposure experiment,

$$\frac{d[P\bullet]}{dt} = -k_t[P\bullet]^2 \quad (34)$$

Integrating the above equation and combining it with Equation (12), $R_p = k_p[P\bullet][M]$, leads to:

$$\frac{[M]}{R_p}\bigg|_{t_2} = \frac{k_t}{k_p}(t_2 - t_1) + \frac{[M]}{R_p}\bigg|_{t_1} \quad (35)$$

Therefore, the ratio k_t/k_p can be determined from the slope of the plot of $[M]/R_p$ (i.e. $(1-X)/R_N$) as a function of time t (Tryson and Shultz, 1979). The starting time t_1 is a time point after the light is turned off. The ending time t_2 is taken well before the reaction dies out.

At each temperature (e.g. 30, 50, and 70°C), from a series of flash exposure experiments (e.g. 0.2, 0.4, 0.6, and 0.8 min irradiation) the value of k_t/k_p at different conversions can be extracted, as shown in Table 2.

Table 2 k_t / k_p and $k_p / k_t^{1/2}$ Values Obtained from DPC Experiments

	Flash Exposure		dark reaction	Continuous Irradiation		QSSA Effect
T(°C)	Time (min)	X	kt/kp	kp/kt ^{0.5}	kp/kt ^{0.5} (QSSA)	Difference (%)
30	0.2	0.150	111.25	0.37	0.37	0.2
	0.4	0.339	21.66	0.16	0.18	12.3
	0.6	0.378	20.78	0.12	0.13	12.2
	0.8	0.424	18.94	0.08	0.09	15.2
50	0.2	0.163	182.72	0.34	0.34	0.2
	0.4	0.342	19.46	0.17	0.19	10.5
	0.6	0.404	14.92	0.12	0.14	13.4
	0.8	0.493	8.12	0.06	0.08	26.9
70	0.2	0.277	41.96	0.38	0.39	2.5
	0.4	0.455	11.43	0.15	0.18	21.2
	0.6	0.491	10.48	0.12	0.14	21.5
	0.8	0.567	7.09	0.07	0.09	27.3

For the continuous irradiation,

$$\frac{d[P\bullet]}{dt} = R_i - k_t[P\bullet]^2 \quad (36)$$

Integrating and combining it with Equation (12), $R_p = k_p[P\bullet][M]$, to obtain:

$$\ln\left(\frac{1+y_2}{1-y_2}\right) - \ln\left(\frac{1+y_1}{1-y_1}\right) = 2(R_i k_t)^{1/2}(t_2 - t_1) \quad (37)$$

with

$$y_{1,2} = \frac{k_t^{1/2}}{k_p R_i^{1/2}} \left(\frac{R_N}{1-X} \right) \Big|_{t_{1,2}} \quad (38)$$

where R_i is evaluated using Equation (16), $R_i = 2.3\phi_i \varepsilon SI$, and Equation (17),

$\frac{dS}{dt} = -2.3\varepsilon SI$. Since both photoinitiator absorptivity and light intensity are a function of

wavelength, $\int_{\lambda_1}^{\lambda_2} \varepsilon(\lambda)I(\lambda)d\lambda$ is substituted for εI in Equations (16) and (17). Equation

(37) combines two kinetic constants together in terms of $k_p / k_t^{1/2}$. For each temperature, a trial and error analysis is performed using k_t / k_p data derived from the dark reaction to evaluate $k_p / k_t^{1/2}$ values at corresponding conversions.

Table 2 lists the ratio k_t / k_p obtained from flash exposure experiments and the ratio $k_p / k_t^{1/2}$ obtained from continuous irradiation experiments. The values of k_p and k_t can thus be determined separately at several different conversions for each temperature (as shown in Table 3), from which the free volume and temperature dependence of k_p and k_t , i.e. the parameters in Equations (23) and (24), can be determined.

Table 3 Determination of Rate Constants k_t and k_p

T(°C)	X	kt/kp	kp/kt ^{0.5}	kt(m ³ /mol-s)	kp(m ³ /mol-s)
30	0.15	111.3	0.37	1694	15
	0.34	21.7	0.16	12	0.6
	0.38	20.8	0.12	6	0.3
	0.42	18.9	0.08	2	0.1
50	0.16	182.7	0.34	3860	21
	0.34	19.5	0.17	11	0.6
	0.40	14.9	0.12	3	0.2
	0.49	8.1	0.06	0.2	0.03
70	0.28	42.0	0.38	254	6
	0.45	11.4	0.15	3	0.3
	0.49	10.5	0.12	2	0.2
	0.57	7.1	0.07	0.3	0.04

As shown in Table 3, at low conversion, the magnitude of k_t is two order higher than k_p . Goodner and coworkers (1997) found that at similar conversion, the magnitude of k_t is three orders higher than k_p for 2-hydroxyethyl methacrylate (HEMA). It's possible that the steric resistance in tetra-functional material studied here affects more significantly the true kinetic constants for termination than for propagation. For both HEMA and E4PETeA, the rate constants k_t and k_p drop dramatically with the conversion increasing. The drop is more significant for tetraacrylate due to the crosslinkage. For both HEMA and E4PETeA, k_t drops at a lower conversion than k_p .

The scientific plotting and data analysis software Origin (OriginLab Corporation) is used for the nonlinear curve fitting of k_p and k_t data to determine the free volume dependence, as shown in Figures 12 and 13. Linear curve fitting in Excel (Microsoft Corporation) is performed to determine the temperature dependence of true kinetic constants k_{p0} and k_{t0} (Equations 25-26), as demonstrated in Figure 14. Figure 15 illustrates the temperature dependence of critical fractional free volume (Equation 31) for propagation and termination.

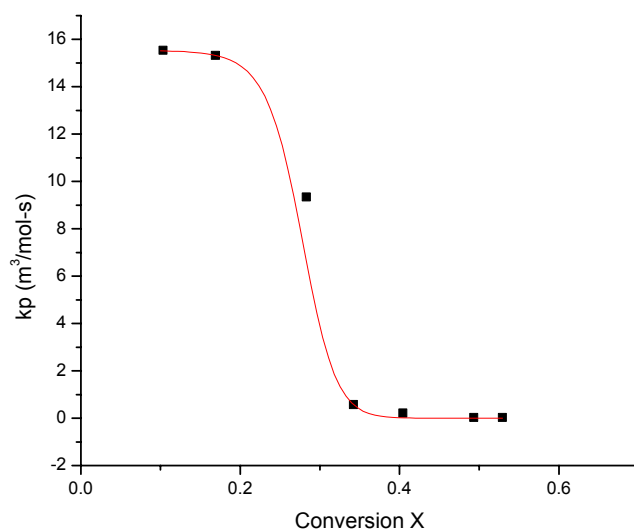


Figure 12 Nonlinear Fit of Propagation Rate Constant k_p vs. Conversion X (50°C)

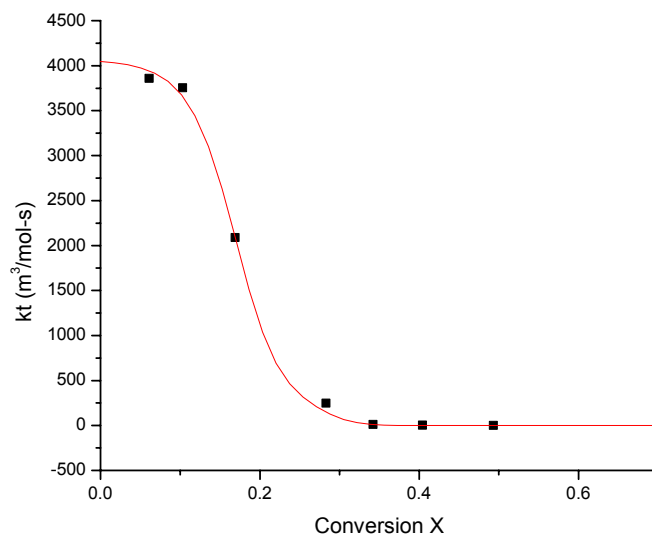


Figure 13 Nonlinear Fit of Termination Rate Constant k_t vs. Conversion X (50°C)

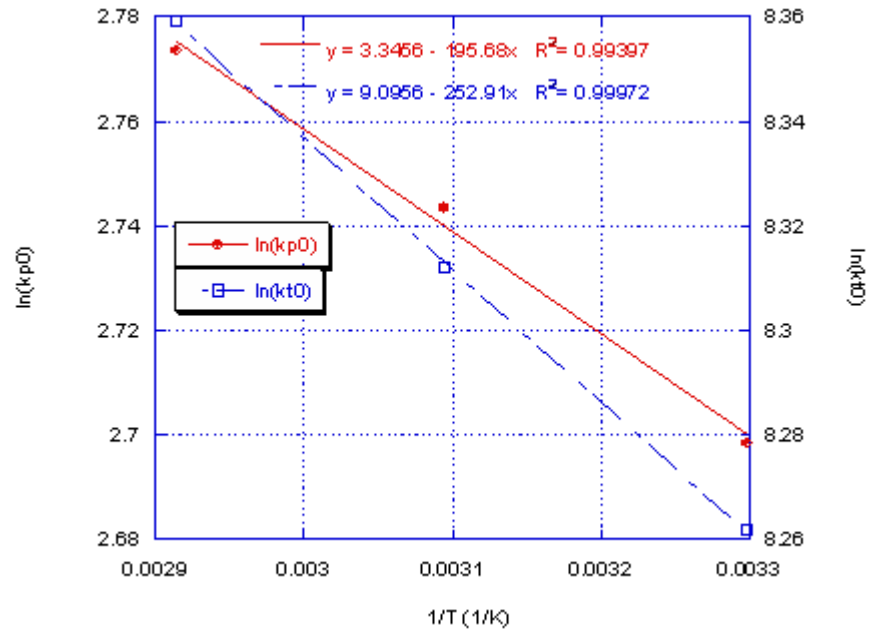


Figure 14 Semi-log Plot of True Kinetic Constants k_{p0} and k_{t0} vs. $1/T$

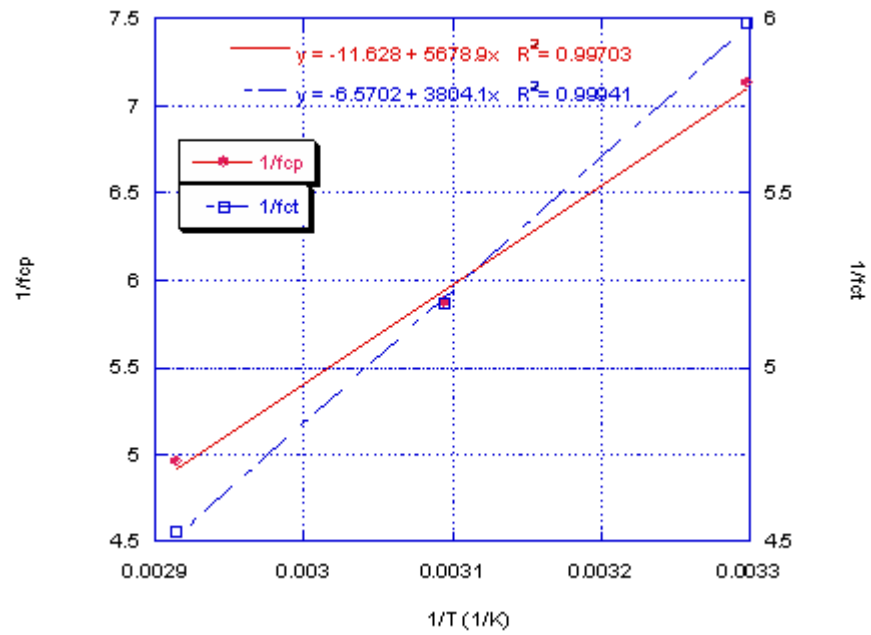


Figure 15 Linear Fit of $1/f_c$ (Critical Fractional Free Volume) vs. $1/T$

The fractional free volume of the tetraacrylate system is found to be one order of magnitude higher than that of HEMA (Goodner, et al., 1997) because the CTE of the system is one order of magnitude higher than that of HEMA. The linear CTE of the tetraacrylate system (see Chapter 4), however, is within the same range of the CTE used for the HEMA system (Goodner, et al., 1997). Accordingly, the critical fractional free volume for propagation and termination of E4PETeA (Figure 15) turns out to be one order of magnitude higher than that of HEMA (Goodner, et al., 1997).

The values of the kinetic parameters obtained are listed in Table 4.

Table 4 Kinetic Parameter Values

Parameters	Symbols	Values	Units
free volume parameter for propagation (see Equation 23)	A_p	6.1	N/A
free volume parameter for termination (see Equation 24)	A_t	6.4	N/A
reaction diffusion parameter (see Equation 24)	R_{rd}	0.013	m^3/mol
pre-exponential factor for propagation (see Equation 25)	A_{Ep}	28.4	$m^3/mol-s$
pre-exponential factor for termination (see Equation 26)	A_{Et}	8916	$m^3/mol-s$
activation energy for propagation (see Equation 25)	E_p	1627	J/mol
activation energy for termination (see Equation 26)	E_t	2103	J/mol

It should be mentioned that instead of integrating Equation (36) to obtain the relationship of k_p and k_t , people usually apply the quasi steady state assumption (QSSA) and Equation (36) is then reduced to:

$$R_i = k_t [P\bullet]^2 \quad (39)$$

Substituting the above equation into Equation (12), $R_p = k_p[P\bullet][M]$, the ratio $k_p / k_t^{1/2}$ can be directly calculated as follows:

$$\frac{k_p}{k_t^{1/2}} = \frac{R_N}{(1-X)\sqrt{R_i}} \quad (40)$$

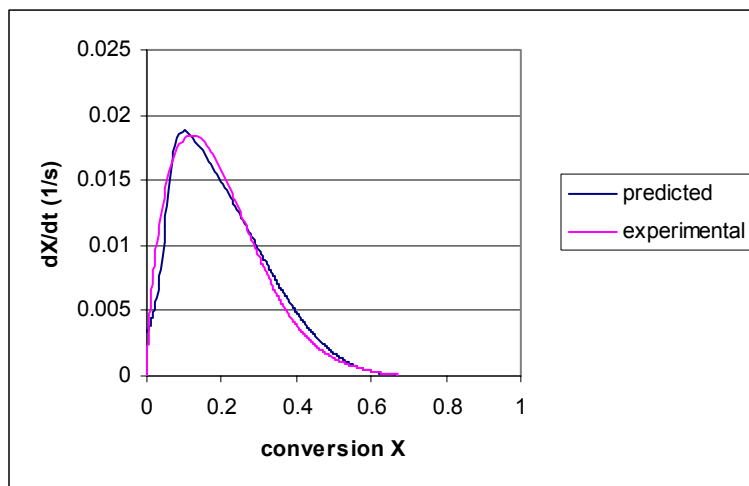
Table 2 also lists the values of $k_p / k_t^{1/2}$ determined with steady state assumption and their comparison with the values obtained without this assumption. It turns out that QSSA is valid only at low conversions; in this specific case, it has more than 10% deviation when the conversion is greater than 30%.

To analyze the kinetic data and parameterize the kinetic model, Goodner and coworkers (1997) have divided the polymerization process under continuous light irradiation into four regions based on the free volume and treated the four regions individually to determine the kinetic parameters. The advantages of this regional analysis method are that only continuous irradiation experiments need to be conducted (flash exposure experiments are not required) and unlike the nonlinear curve fitting, a unique parameter set can be expected. However, for a highly crosslinked polymerization system as investigated here, the first region where there are no diffusional limitations on either propagation or termination and the third region where there are no diffusional limitations on propagation but termination is reaction-diffusion controlled are often found to be ill-defined. The second region, autoacceleration, could also be ill-defined or just have not enough data to determine parameters. Often only the fourth region, autodeceleration, is defined well. This limits the application of the regional analysis method which requires

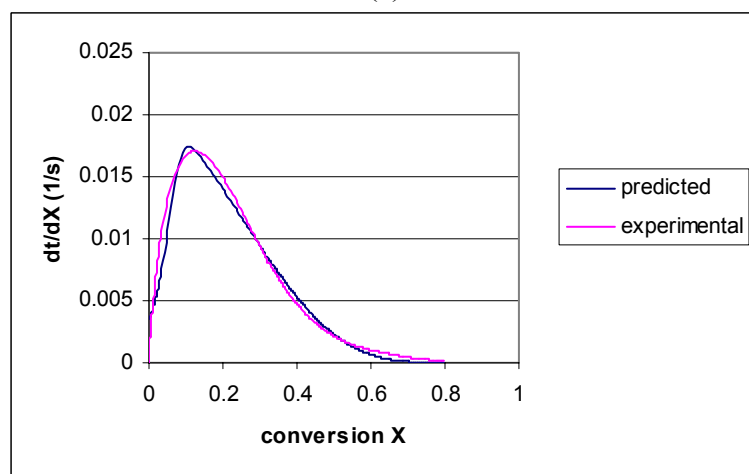
the system have four distinct kinetic regions. To broaden its application, the flash exposure experiment (so-called unsteady state analysis) has been proposed to find k_{t0} (or k_{p0}) for systems that don't have a well-defined first (or third) region (Goodner et al., 1997). In this case, however, the regional analysis has lost one of its attractive characteristics mentioned above. In addition to the continuous irradiation experiments, flash exposure experiments also have to be conducted and analyzed to find k_{p0} or k_{t0} to complement the regional analysis. Furthermore, the regional analysis method is established based on the QSSA assumption throughout the reaction, which is not valid as shown in Table 2.

3.4 Kinetic Model Validation

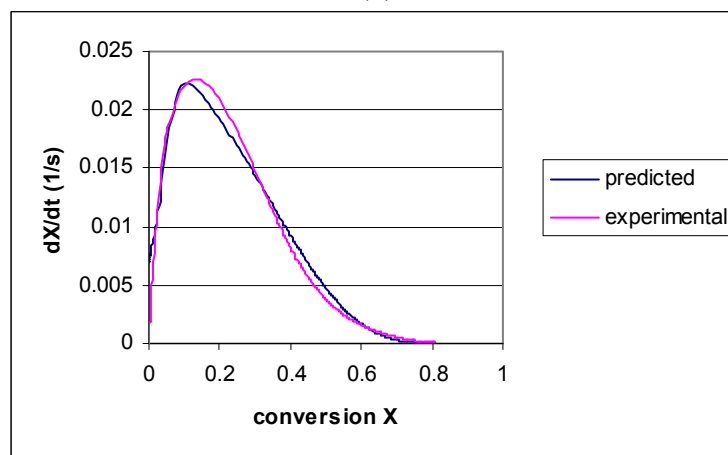
It's not easy to find a unique solution for the nonlinear curve fitting. Other restrictions should be applied for the fitted parameters in order to obtain a reasonable and unique parameter set. The fitted parameters should not only achieve a best fit for the kinetic data, but should be physically reasonable as well as capable of predicting kinetic behavior. Figure 16 demonstrates the kinetic model simulations for a series of continuous irradiation experiments conducted at different temperatures with the light power of 0.1 mW. The agreement between the predicted and experimental results validates the adopted kinetic model and the determined kinetic parameters.



(a)



(b)



(c)

Figure 16 Comparison of the Experimental and Simulated Polymerization Rate Curves (incident power = 0.1 mW): (a) 30°C, (b) 50°C, (c) 70°C

CHAPTER 4

MATERIAL CHARACTERIZATION

As listed in Table 1, some process and material parameters need to be determined in order to simulate the SL cure process. The process and laser parameters (such as laser scanning speed V_s , bath temperature T_b , laser power P_L , and laser beam radius w_o) are obtained from the actual part building process in SLA-250/50 (3D systems, laser wavelength $\lambda = 325\text{nm}$ ⁵). $h = 4.18 \text{ W/m}^2\text{-K}$ is taken as the value of heat convection coefficient at the interface of the natural air flow and the resin (Pananakis & Watts, 2000). $\phi_i = 0.6$ is taken as the quantum efficiency of initiation for DMPA (Goodner et al., 2002). The thermal and physical properties of the resin are evaluated for the model compound system comprised of E4PETeA tetraacrylate and 2 wt% photoinitiator DMPA. The initiator concentration is higher than in Chapter 3 to facilitate the SL cure process. They are obtained from literature, theoretical approximation, or experimental determination.

4.1 Specific Heat Capacity

The modulated differential scanning calorimeter (MDSC) option for DSC 2920 (TA Instruments) was used to measure the specific heat capacity of the pure monomer and pure polymer. MDSC provides unique capabilities besides those of standard DSC such as separation of complex transitions, detection of weak transitions, accurate measurement of

⁵ SLA Systems Specifications, 3D Systems, <http://www.3dsystems.com>

polymer crystallinity, and direct determination of heat capacity and thermal conductivity.⁶

In addition to the standard DSC cell calibration (performed in calibration mode) for cell constant, baseline and temperature, a heat capacity calibration (performed in modulated mode) was also performed in order to obtain accurate heat capacity measurement. The sapphire standard (provided by TA Instruments) was used as the calibrant. The calibration procedure should be as close as possible to that of the following measurements. The weights of two pans with lids were matched to within ± 0.1 mg. One pair of pan and lid were sealed and used as reference; the other pair was used to hold the weighed calibrant or sample and then sealed and placed in the sample position in the DSC cell. The method which tells the machine what to execute was formulated by combining the recommendations on heat capacity calibration and on heat capacity measurements as well as general MDSC operating parameters.⁶ The liquid nitrogen cooling accessory (LNCA) was used for the optimum performance of the MDSC measurement. The nitrogen gas was used to purge and circulate in the DSC cell at a rate of 40 ml/min before and during the experiment. A data sampling interval of 1.0 seconds/point was used. The MDSC directly measures the heat capacity and stores the signal.

Figures 17 and 18 are exported plots of heat capacity signal for liquid E4PETeA monomer and its cured polymer, respectively. Samples were weighed 12.09 ± 0.03 mg using an analytical balance (AG 245, Mettler Toledo).

⁶ 'Modulated DSCTM Option', DSC 2920 Differential Scanning Calorimeter Operator's Manual, Thermal Analysis & Rheology, TA Instruments, 1995.

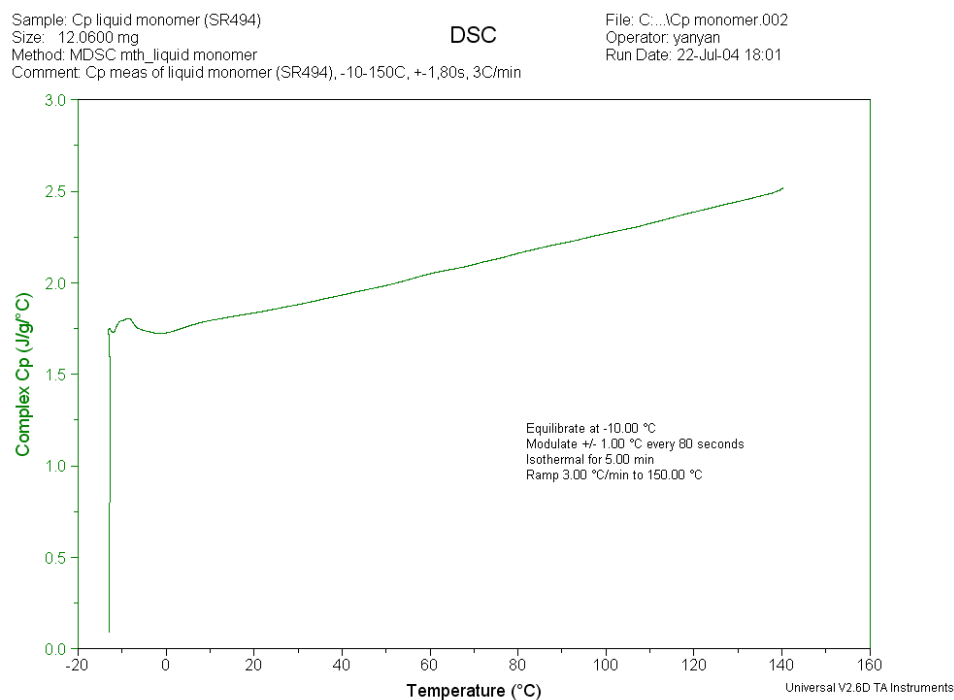


Figure 17 C_p -T Plot of Liquid E4PETeA Monomer Exported from MDSC Data

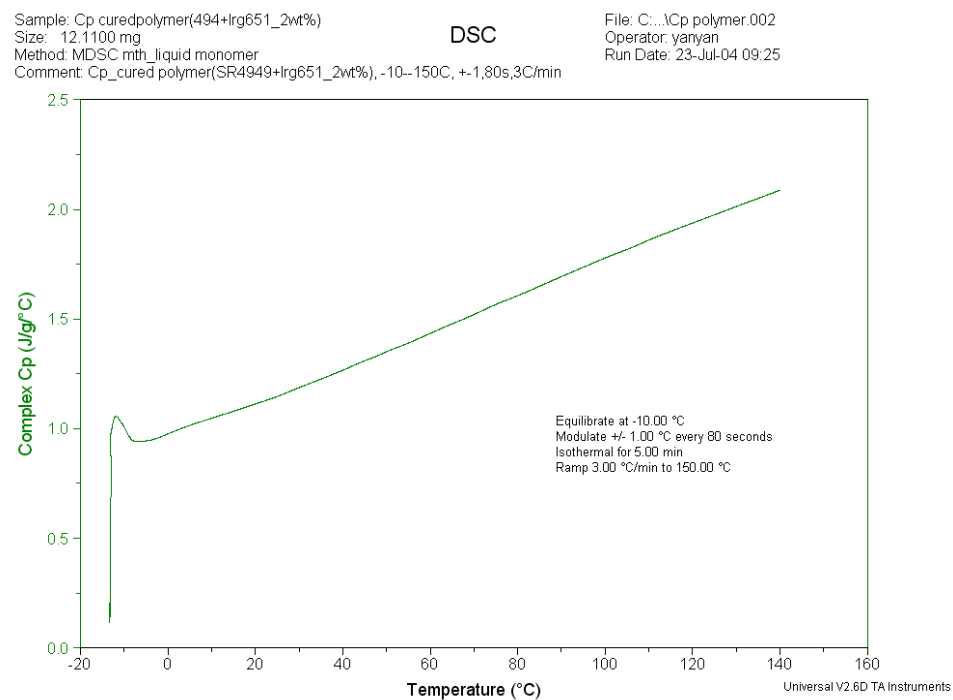


Figure 18 C_p -T Plot of Cured E4PETeA Polymer Exported from MDSC Data

The heat capacities were found to be functions of temperature as follows:

$$C_{P,M} = 5.6 \times T(K) + 218.6 \quad (41)$$

$$C_{P,P} = 9.1 \times T(K) - 1535.5 \quad (42)$$

where $C_{P,M}$ and $C_{P,P}$ are the heat capacities (J/Kg-K) of monomer and cured polymer, respectively.

The molar heat capacity of liquid E4PETeA monomer was also calculated to be 947 J/mol-K (i.e., 1.8 J/g-K for specific heat capacity) at 25 °C by the addition of group contributions (Van Krevelen, 1990). This calculated result is within 5% of the experimental value at the same temperature, which justifies the experimental measurement. Furthermore, the heat capacity value of E4PETeA is close to those of other acrylates such as methyl and butyl acrylates, etc (Yaws, 2003).

A weight-averaged heat capacity was used for the curing material, i.e., mixture of monomer and cured polymer:

$$C_P = C_{P,M}(1 - X) + C_{P,P}X \quad (43)$$

where X is monomer conversion.

4.2 Glass Transition Temperature

The glass transition temperatures of liquid E4PETeA monomer and its cured polymer are determined using a standard differential scanning calorimeter (DSC 2920, TA Instruments). The samples were weighed ~16mg for several heating rates: 5, 10, 15, 20 °C/min. Figures 19 and 20 are the heat flow curves at 10 °C/min heating rate and demonstrate the glass transition of liquid monomer and cured polymer, respectively. Figures 21 and 22 illustrate the effect of heating rate on the T_g measurement. In the range of heating rates tested, the measured T_g value increases linearly with the heating rate. For T_g measurement, a heating rate within 10-20 °C/min is recommended. A lower heating rate leads to gradual material change and thus less obvious glass transition.

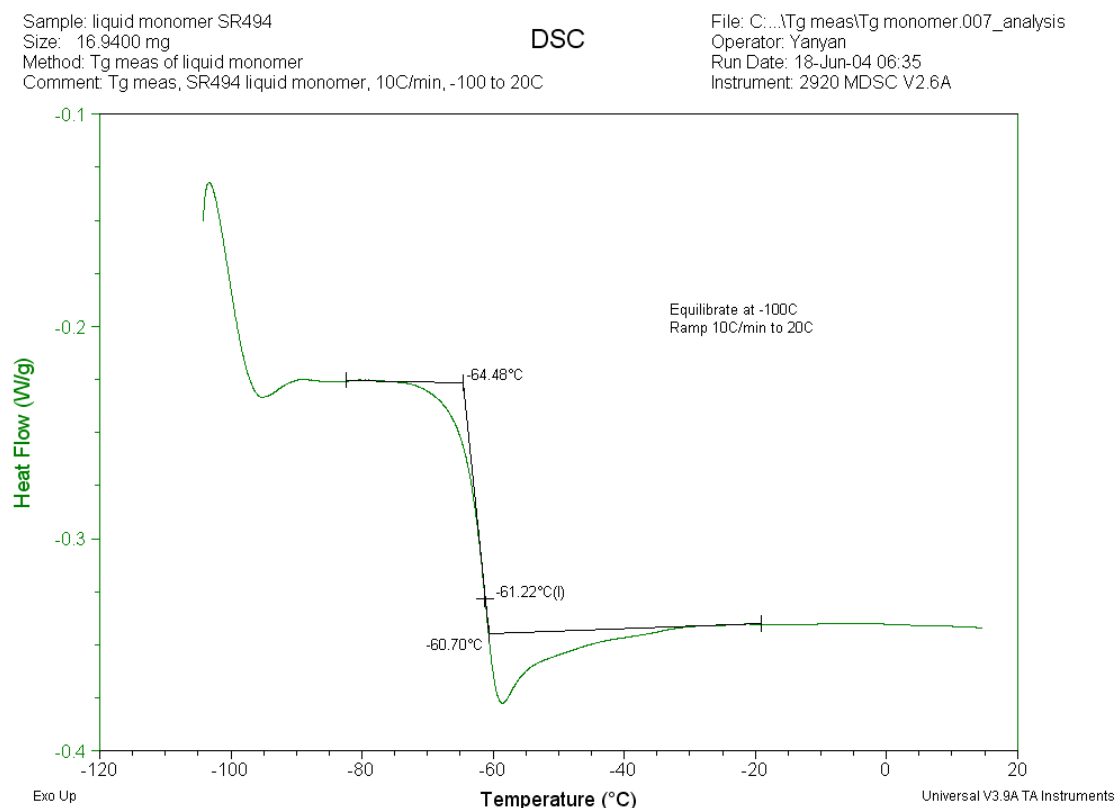


Figure 19 Glass Transition of Liquid E4PETeA Monomer Detected by DSC

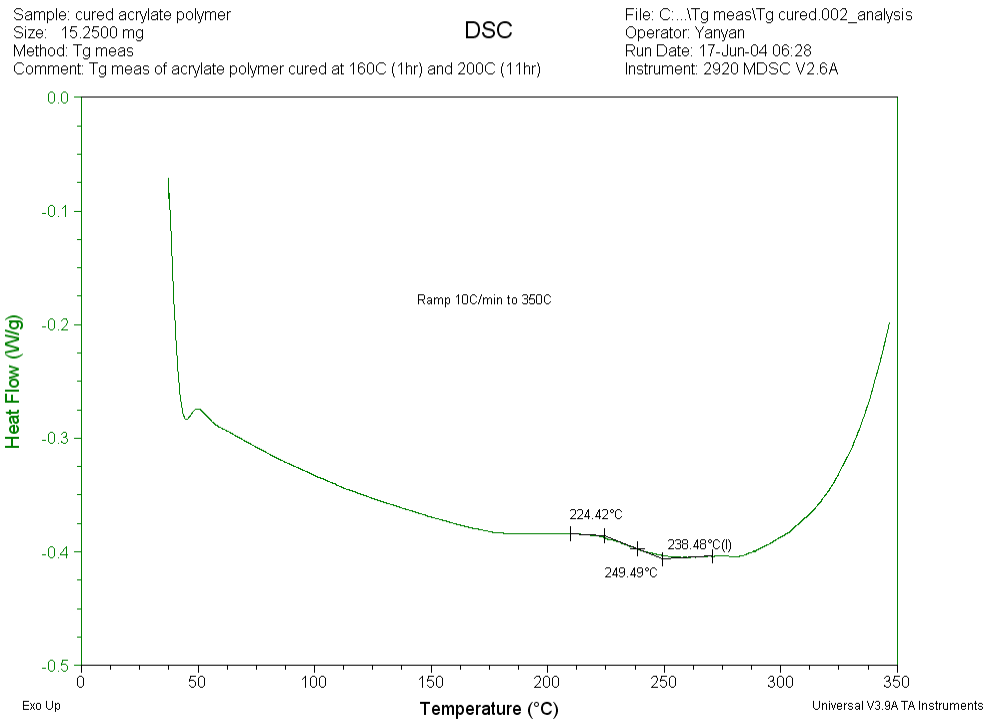


Figure 20 Glass Transition of Cured Poly(E4PETeA) Detected by DSC

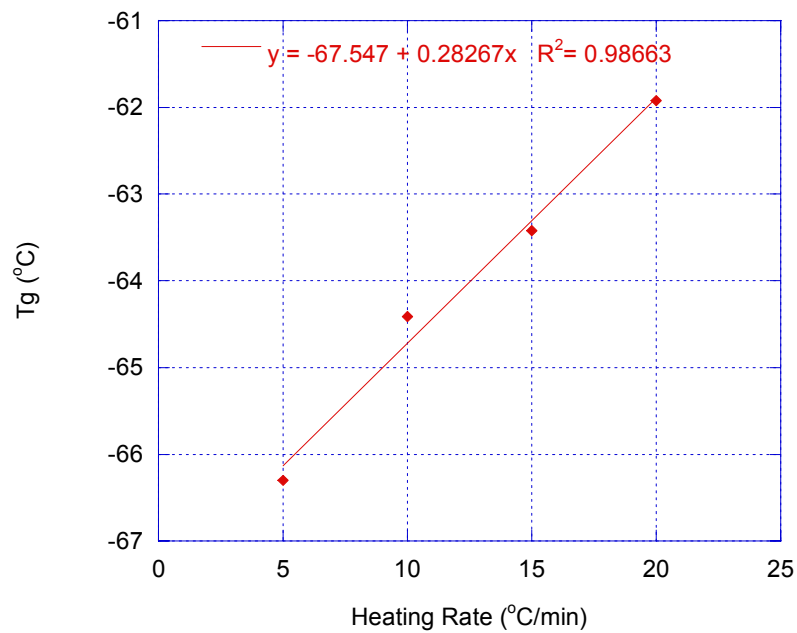


Figure 21 Effect of Heating Rate on Measured T_g Value of Liquid Monomer

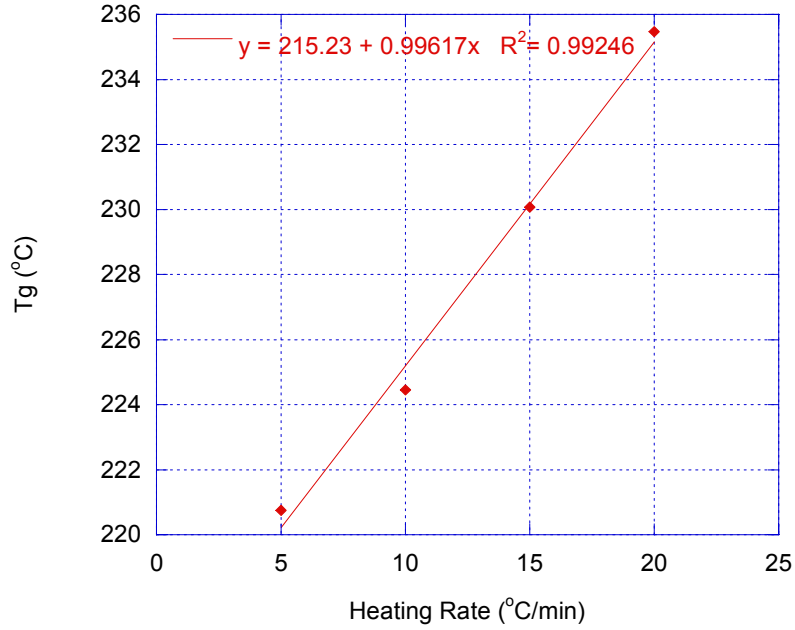


Figure 22 Effect of Heating Rate on Measured T_g Value of Cured Polymer

To eliminate the heating rate effect, the T_g values obtained by extrapolating linear curves in Figures 21 and 22 to 0 °C/min, -67.5 °C and 215.2 °C, are adopted for liquid monomer and cured polymer, respectively.

4.3 Coefficient of Thermal Expansion

The coefficients of thermal expansion (CTE) of monomer and cured polymer were determined by using an ellipsometry technique to measure film thickness at different temperatures. The linear CTE is defined as (Van Krevelen, 1990):

$$\beta = \frac{1}{L} \frac{\partial L}{\partial T} \quad (44)$$

where $\frac{\partial L}{\partial T}$ is the slope of the film thickness versus temperature plot, and L the average thickness over the temperature range investigated.

The variable angle spectroscopic ellipsometer (VASE VB 250, J.A. Woollam) was used to determine the film thickness at elevated (heating) or lowered (cooling) temperatures. A hot plate is installed on the commercial ellipsometer. The temperature controller (OMEGA CN 76000) can control temperature within ± 0.2 °C. Thermocouple (HH 11, OMEGA) was used for temperature calibration. At each set temperature, the ellipsometer scan starts after the film reaches thermal equilibrium. The film was spin-coated on silicon substrate (with native oxide layer) from a 10 wt% propylene glycol methyl ether acetate (PGMEA) solution. The monomer film was put in the vacuum oven and baked at 90 °C in vacuum for 1hr to remove the solvent without solidifying the monomer. The solid polymer film was obtained by baking the liquid film containing monomer and photoinitiator and solvent at 180 °C in vacuum for 60 hrs. No phenomenon such as discoloration or brittleness was observed, hence no apparent degradation occurred

Figures 23 and 24 demonstrate the temperature dependence of monomer film thickness above T_g and of polymer film thickness below T_g , respectively. β (monomer) = 5.9×10^{-4} 1/K and β (polymer) = 0.96×10^{-4} 1/K are found from these two graphs.

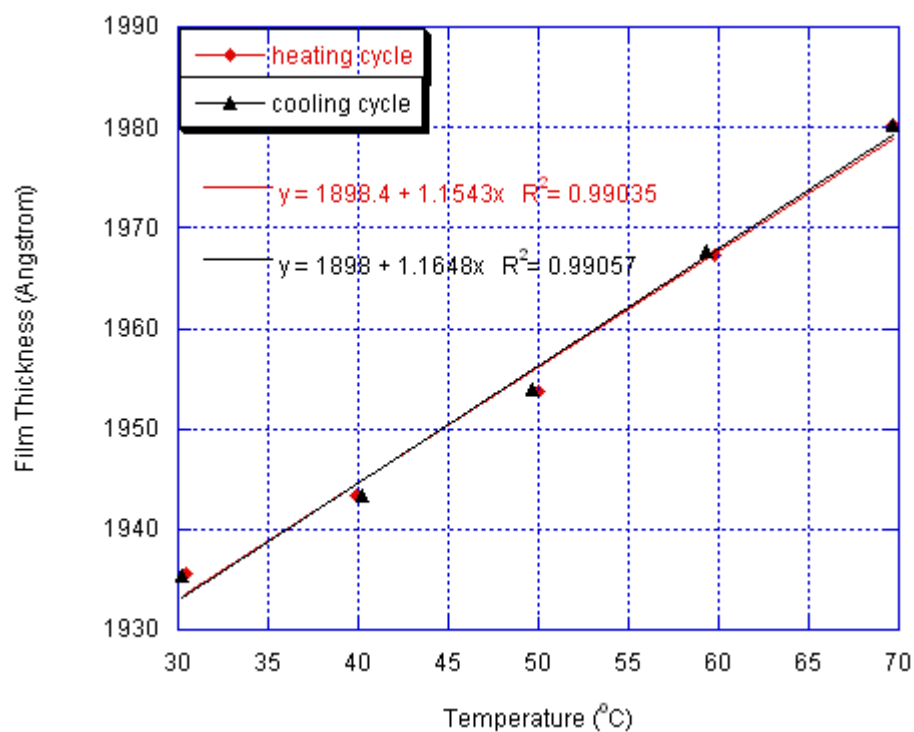


Figure 23 Temperature Dependence of Liquid E4PETeA Monomer Film Thickness

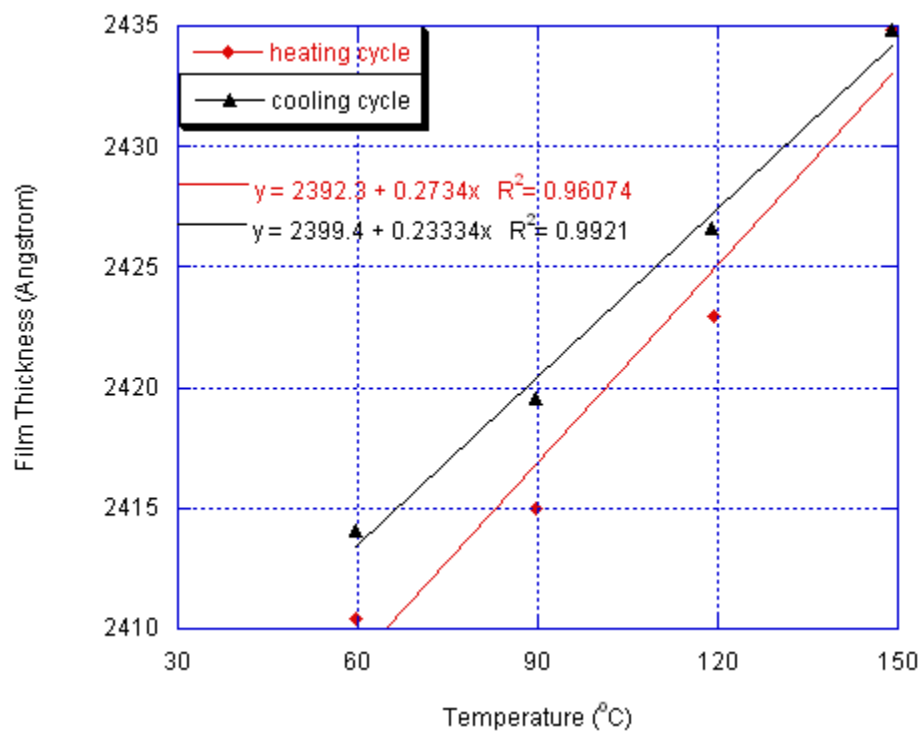


Figure 24 Temperature Dependence of Cured E4PETeA Polymer Film Thickness

The heat treatment of the film before ellipsometric measurement reduced the entrapped solvent enough that no solvent effect was observed during the heating or cooling stages. Two L - T curves are found to almost overlap with each other in Figure 23. In Figure 24, the fit for the first temperature scan (heating cycle) has a slightly higher slope than that for the second scan (cooling cycle). This is probably due to the residual unconverted monomer which has greater CTE entrapped in the polymer matrix.

The films with thickness above 1000 Å were made for measurement. For the films with thickness below 1000 Å, the thermal fluctuation of the air above the film could cause a big error in the thermal property quantification (Kahle et al., 1998).

The temperature dependence of Si substrate n & k spectra (complex refractive index: $\mathbf{n}(\lambda) = n(\lambda) + ik(\lambda)$) was taken into account when fitting the ellipsometric data to determine the film thickness. A slower increase in CTE was observed with film thickness decreasing, compared with the result from the fit with only the optical properties of Si at 25 °C, as shown in Figure 25. The thickness variation (500-2400 Å) was achieved by varying the spin speed and time. The CTE increases drastically for thickness below 2000 Å, but remains approximately constant for greater thickness.

Kahle and coworkers (1998) demonstrated that when temperature dependent substrate data were used for the fit, there was no pronounced thickness effect for the CTE within the thickness range of 500 to 10^5 Å for the poly(methyl methacrylate) (PMMA) film they investigated. This is different from what we observed here for the poly(E4PETeA) film, which might indicate that the trend discussed here depends on the material properties of the film such as molecular weight or cross-link density. The CTE value at greater thickness (2400 Å here) was taken as the bulk CTE, $\beta(\text{polymer}) = 0.96 \times 10^{-4}$ 1/K.

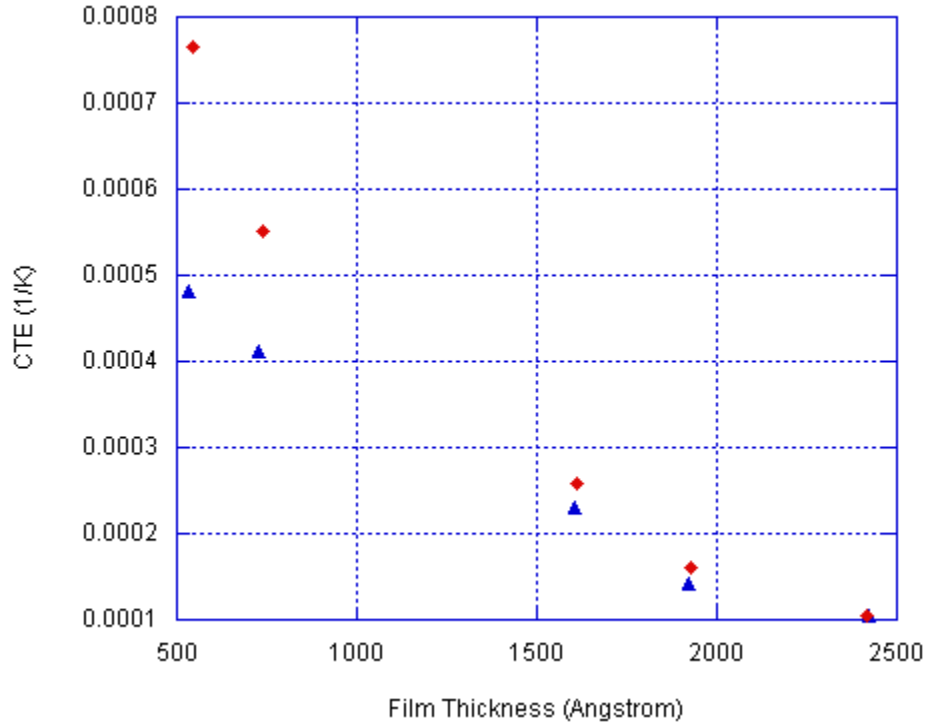


Figure 25 CTEs of Poly(E4PETeA) below T_g Determined by Linear Regression of Curves Obtained by Fitting with Si Substrate Optical Data of 25°C (diamonds) and of Curves Obtained by Fitting with Temperature Dependent Si Substrate Data (triangles)

The polymer CTE value, however, was measured under the constraint of the Si wafer and therefore it overestimates the true value. The true CTE is related to the constrained CTE by the following equation (Kahle et al., 1998):

$$\beta_{unconstrained} = \beta_{constrained} \times \frac{1-\nu}{1+\nu} \quad (45)$$

where ν is Poisson's ratio. The $\frac{1-\nu}{1+\nu}$ term converts expansion constrained by the Si substrate to a true unconstrained CTE value. Taking ν below T_g as 0.40 (typical Poisson's ratio value for polymers, Van Krevelen, 1990) for the poly(E4PETeA), the true CTE is calculated to be 0.4×10^{-4} 1/K.

The liquid film, on the other hand, is not constrained by the substrate, therefore, the measured value is the true bulk CTE, β (monomer) = 5.9×10^{-4} 1/K.

The volumetric CTE can be obtained by the following equation (Van Krevelen, 1990), assuming the bulk material is isotropic.

$$\alpha = \frac{1}{V} \frac{\partial V}{\partial T} = 3\beta_{unconstrained} \quad (46)$$

where V is the volume of the material over the temperature range investigated.

The volumetric CTEs of E4PETeA (above T_g) and its polymer (below T_g) are thus determined to be 1.77×10^{-3} , and 1.23×10^{-4} 1/K, respectively. These values are at the same magnitude as CTEs of ethylene glycol dimethacrylate (EGDMA) and its polymer (Bowman and Peppas, 1991). The polymer CTE value is also in the same range as PMMA (Brandrup and Immergut, *Ed.*, 1989). The monomer CTE is at the same order of magnitude as other acrylates such as methyl and butyl acrylates, etc (Yaws, 2003).

4.4 Density

The density of the cured polymer was found to be 1200 Kg/m³ at 35 °C (column control temperature) by using density gradient column (DC-4, Techne). Two water-calcium nitrate solutions of different concentrations were used to fill the column and form a linear density gradient from top to bottom.

The temperature dependence of density can be described as follows using the volumetric CTE α :

$$\rho_P = \frac{\rho_P(308K)}{1 + \alpha_P(T - 308)} = \frac{1200}{1 + \alpha_P(T - 308)} \quad (47)$$

Similarly, we have the following for the monomer density:

$$\rho_M = \frac{\rho_M(298K)}{1 + \alpha_M(T - 298)} = \frac{1128}{1 + \alpha_M(T - 298)} \quad (48)$$

where $\rho_M(298\text{ K}) = 1128\text{ Kg/m}^3$ from the product technical data sheet.

The density of cured polymer was also calculated at 298 K. Using a group contribution method (Van Krevelen, 1990), the molar volume per structural unit of the polymer was calculated to be 404.42 cm³/mol at 298 K. With the unit molecular weight of 528 g/mol, the density of the cured polymer was found to be 1290 Kg/m³ at 25 °C, which is within 10% of the value obtained from Equation (47) for the same temperature. This justifies the measurement and Equation (47) will be adopted.

The density of the curing material system can be expressed as:

$$\rho = \rho_M \phi_M + \rho_P (1 - \phi_M) \quad (49)$$

where ρ_P and ρ_M are described in Equations (47) and (48), respectively, and ϕ_M is the monomer volume fraction as described before.

4.5 Thermal Conductivity

The thermal conductivity of polymer can be calculated using the following equation (Van Krevelen, 1990):

$$k = \rho C_p L_f \left(\frac{U_R}{V_m} \right)^3 \left[\frac{3(1-\nu)}{1+\nu} \right]^{1/2} \quad (50)$$

where ρ , C_p , L_f , U_R , V_m , and ν are density, specific heat capacity, average free path length, Rao function, molar volume per structural unit and Poisson's ratio of the cured polymer, respectively. It can be obtained from Sections 4.1 and 4.3 that at 298 K, $\rho = 1.25$ g/ml, $C_p = 1.18$ J/g-K, and $V_m = 404.42$ cm³/mol. $L_f = 5 \times 10^{-11}$ m for PMMA is taken. The Rao function, U_R , is calculated to be 22,460 (cm³/mol)·(cm/s)^{1/3} using a group contribution method (Van Krevelen, 1990). The factor $\left[\frac{3(1-\nu)}{1+\nu} \right]^{1/2}$ is nearly constant for

solid polymers (≈ 1.05) (Van Krevelen, 1990). The thermal conductivity of the cured polymer is thus calculated to be 0.123 W/m-K at 298 K.

The thermal conductivity of polymer is temperature dependent. From a generalized plot of $k(T)/k(T_g)$ as a function of T/T_g based on available experimental data (Van Krevelen, 1990), thermal conductivity of amorphous polymers can be evaluated at different temperatures. The thermal conductivity of the cured E4PETeA polymer at its glass transition temperature 230 °C (Section 4.2) was thus found to be 0.135 W/m-K, which is within 10 % of the value at 25 °C and therefore the temperature dependence can be ignored in the temperature range during the cure reaction.

The thermal conductivity of the liquid acrylate monomer was measured using the relative transient hot-wire method (Sun and Teja, 2003). A U-shape Pyrex cell, with capillary as part of it, filled with liquid mercury is inserted into the liquid sample. The Pyrex capillary is employed as the wire. A Hewlett-Packard (Model 6213A) power supply is used to provide the voltage for heating. A thermocouple is used to measure the sample temperatures. Further details of the experimental apparatus and procedure as well as theory were described by DiGuilio and Teja (1990). The thermal conductivity of the liquid E4PETeA is found to be 0.161 W/m-K at 297.8 K by averaging the results of five experiments. The value is reproducible within 0.5% and close to the thermal conductivity values (~ 0.13 W/m-K at 297.8 K) of other acrylates such as butyl acrylate and methyl acrylate, etc (Yaws, 2003). The temperature dependence is insignificant and thus ignored within the SL cure temperature range (refer to other acrylates, Yaws, 2003).

The later modelling results demonstrate that thermal conductivity is not a sensitive parameter. For approximation, the averaged value of the cured polymer and liquid

monomer (0.142 W/m-K) can be taken as that of the curing material system to be used in the process model. This value is at the same order of magnitude as that used for hexanedioldiacrylate (HDDA) curing system, 0.2 W/m-K (Flach and Chartoff, 1995a).

4.6 Heat of Polymerization

The isothermal standard DSC experiments performed on the model material show that the thermally initiated polymerization doesn't occur below 130 °C. The DPC experiments were performed at constant light intensity (0.36 mW/cm²) for several different temperatures below 130 °C. The heat generated due to polymerization was found to increase with temperature linearly (Figure 26).

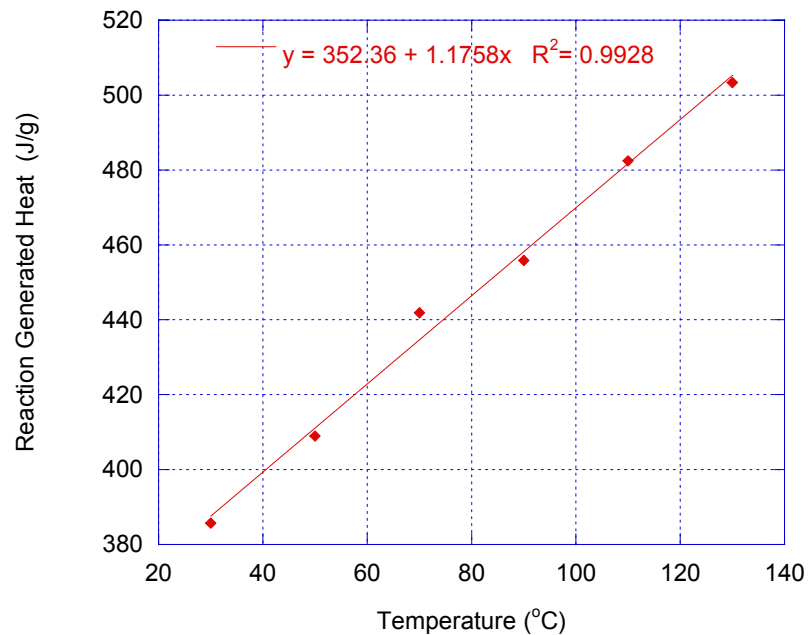


Figure 26 Effect of Temperature on Heat Generated by Polymerization

Additional standard DSC experiments were conducted at elevated temperatures (till 350 °C at a rate of 10 °C/min) for samples irradiated at 130 °C. A small amount of residual heat was detected and added to give the maximum total heat of 540 J/g generated at light intensity = 0.36 mW/cm².

The DPC and subsequent DSC experiments were repeated for higher light intensities (30, 40, 50, and 60 mW/cm²) and no more heat due to reaction was detected.

Therefore, 540 J/g can be taken as the heat of polymerization of the model material used.

The heat of polymerization was also calculated to be 650 J/g from the theoretical enthalpy of 20.6 kcal/mol per acrylate double bond (Anseth et al., 1994b). This value is within 20 % of the experimental result.

4.7 Absorption Coefficient

The absorption coefficient of photoinitiator, DMPA, was determined by using a UV-VIS spectrometer (Lambda 19, Perkin Elmer) and Beer's law. To obtain the absorption spectrum of DMPA in its E4PETeA solution, spectral subtraction (Smith, 1996) was performed.

$$A(\text{DMPA}) = A(\text{solution}) - \text{subtraction factor} \times A(\text{monomer}) \quad (51)$$

where A represents the absorption spectrum. The 0.05, 0.1, 0.2 wt% DMPA in E4PETeA were used as sample and pure E4PETeA monomer as reference in the spectrometer. The absorption spectrum thus obtained is the direct subtraction of the absorption of pure

monomer from that of solution. The subtraction factor the reference absorption is multiplied by was taken as 1.0 due to the low concentrations investigated. The investigated system assumed to obey the Beer's law, the extinction coefficient spectra of the three solutions of different concentrations overlap with one another (Figure 27).

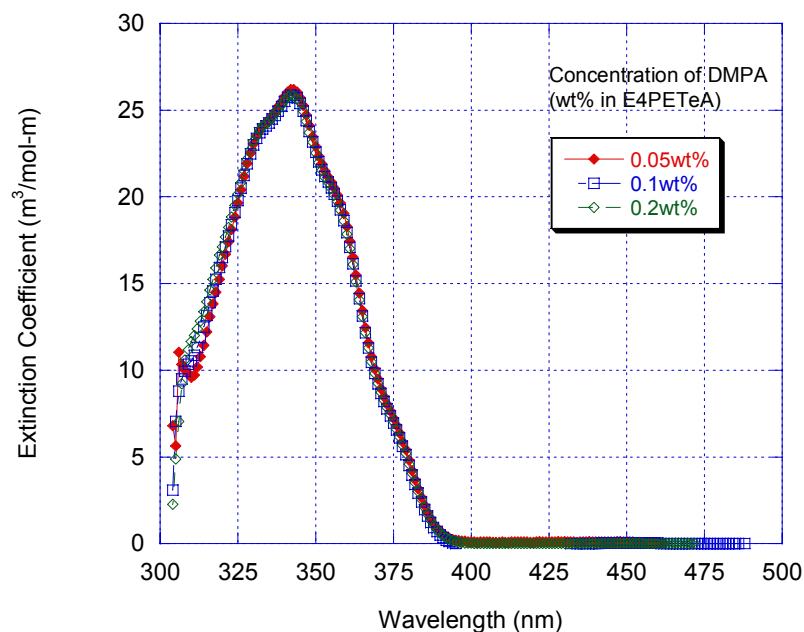


Figure 27 Absorption Coefficient Spectrum of DMPA

4.8 Summary

In this chapter, the material thermal and physical properties are measured experimentally and verified by the theoretical calculation and literature values for similar materials. These values are listed in Table 5 and used in the SL process model established in Chapter 2.

Table 5 Characterized Material Properties

Material Parameters	Values	Units
thermal conductivity	0.142	W/m-K
heat of polymerization	2.85e5	J/mol
absorptivity (initiator)	19.9	m ³ /mol-m
quantum yield of initiation	0.6 ⁷	
coefficient of thermal expansion (monomer)	0.00177	1/K
coefficient of thermal expansion (polymer)	0.00012	1/K
glass transition temperature (monomer)	205.65	K
glass transition temperature (polymer)	488.35	K
heat capacity (monomer)	$C_{P,M} = 5.6 \times T(K) + 218.6$	J/kg-K
heat capacity (polymer)	$C_{P,P} = 9.1 \times T(K) - 1535.5$	J/kg-K
heat capacity (curing system)	$C_P = C_{P,M} (1 - X) + C_{P,P} X$	J/kg-K
density (monomer)	$1128 / (1 + \alpha_M (T - 298))$	kg/m ³
density (polymer)	$1200 / (1 + \alpha_P (T - 308))$	kg/m ³
density (curing system)	$\rho = \rho_M \phi_M + \rho_P (1 - \phi_M)$	kg/m ³

⁷ Goodner et al., 2002

CHAPTER 5

SIMULATIONS

With the kinetic parameters determined in Chapter 3 (Table 4), material properties evaluated in Chapter 4 (Table 5), and laser and process parameters recorded in the part building process, the SL cure process model established in Chapter 2 is solved using the multiphysics modelling and simulation code FEMLAB. FEMLAB is a product of the COMSOL Group ⁸ and has many model types available for use (application models). It also supports equation-based modelling, enabling users to enter their specific differential field equations. Application models were used in this research.

The process model established earlier can be easily customized in the FEMLAB environment. Since SL curing is a coupled mass and energy balance problem, two application models, diffusion and heat transfer by conduction, have been employed to accomplish the description of the cure process model. The transient analysis mode is selected. The 2D geometry described in Chapter 2 is the domain in which the balance equations apply when the laser draws a single line. As mentioned earlier, a small domain size has been adopted initially, which has then increased until no significant deviation in the modeling results from different domain sizes is observed, i.e., the domain should be large enough to accommodate the phenomena occurring physically. The balance equations established in the process model are consistent with those described in FEMLAB application models. The initial conditions are applied to the domain and boundary conditions applied to each boundary of the domain. The numerical values or

⁸ COMSOL Group, <http://www.comsol.com/>

formula descriptions of the material, process, and kinetic parameters also enter the software. Triangular, quadratic, and Lagrange elements have been selected for domain discretization. The area where the reaction occurs and the resin properties vary significantly has finer mesh. The initial and upper limit of the time step size can be set manually. The absolute tolerance has been set for each individual dependent variable based on their initial values. The absolute and relative tolerances determine the limit for the error estimated in each integration step⁹. The model is then solved using a time-dependent nonlinear solver in the software.

Three basic cases of the laser drawing patterns in SL are simulated (Figure 28): a single laser drawn line (also see Figure 5), overlapping single-layer lines with certain spacing, and stacked single lines with certain layer thickness.

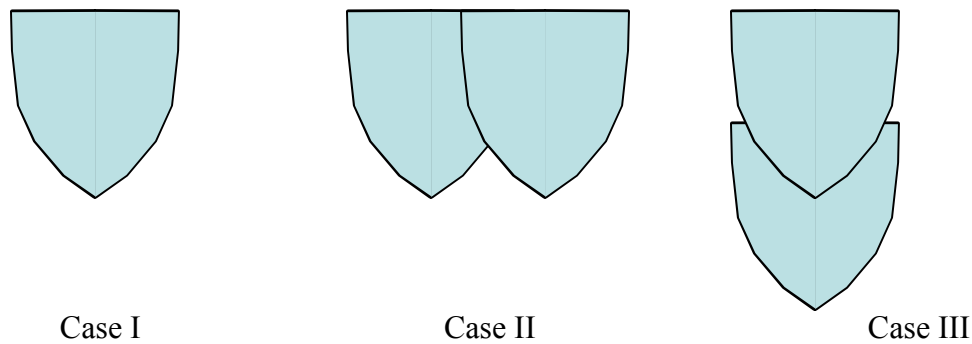


Figure 28 Three Basic Laser Drawing Patterns: Case I. Single Laser Drawn Line, Case II. Overlapping Single-Layer Lines, Case III. Stacked Single Lines

For each case, the mesh convergency, time stepping convergency, and domain convergency (i.e. the solution is converging to a stable value as the mesh is refined, the

⁹ “User’s Guide – FEMLAB 3.0”, COMSOL Group.

time step size is reduced, or the domain is enlarged) have been performed to ensure valid and accurate solution.

All the simulations presented here have used ethoxylated (4) pentaerythritol tetraacrylate loaded with 2 wt% 2,2-dimethoxy-2-phenylacetophenone as photoinitiator. The values of the process and laser parameters used for the simulations are listed below.

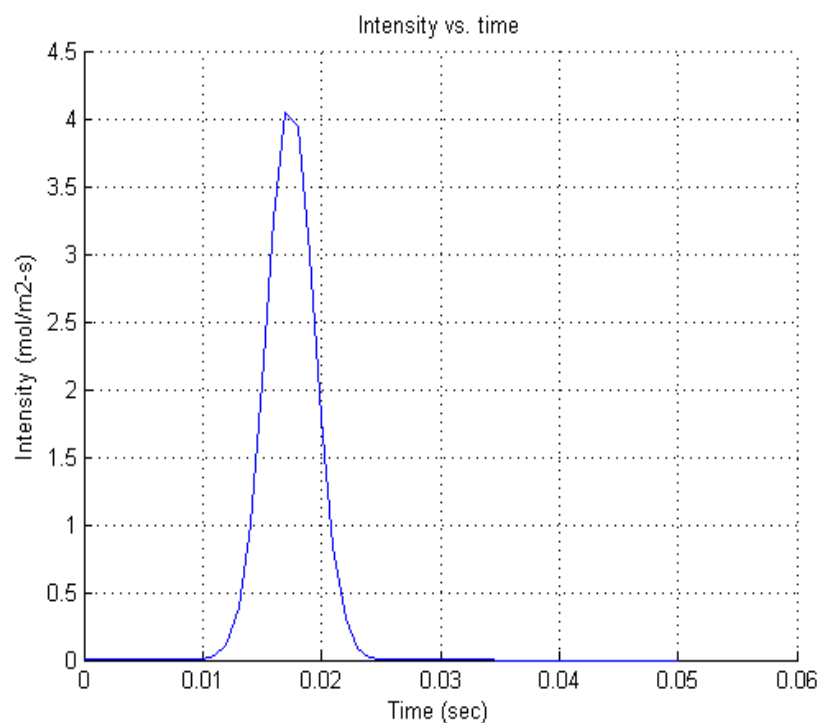
Table 6 Process and Laser Parameter Values Used for Simulations

	Parameters	Values	Units
Process Parameters	laser scanning velocity	0.0272	m/s
	bath temperature	304.55	K
	thermal convection coefficient	4.18	W/m ² -K
	chamber temperature	300.48	K
Laser Parameters	laser power	0.0288	W
	wavelength	325	nm
	beam radius	1.1×10^{-4}	m

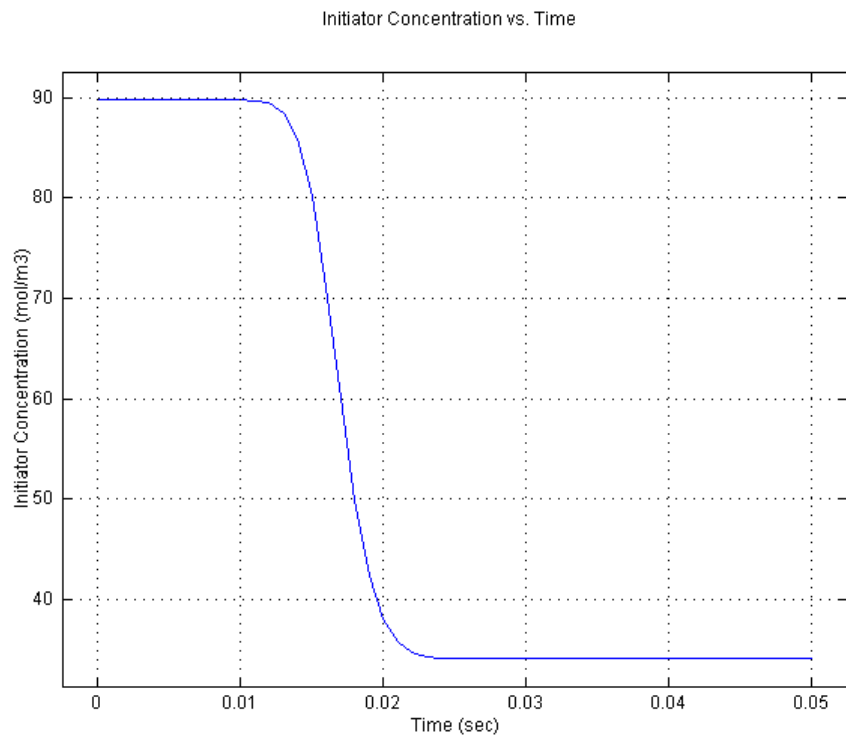
5.1 Single Laser Drawn Line

The process model (consisting of governing equations, domain, initial and boundary conditions) for this case has been established in Chapter 2. The profile of the transient intensity exposed on the resin is also described in Chapter 2. The graphs in Figure 29 demonstrate how the monomer conversion, temperature, radical concentration, and initiator concentration at a particular spatial point (x,0,0) (any point on centerline of the cured line at the surface) vary with time. The curing reaction occurs immediately upon the laser exposure. The temperature increases rapidly due to the rapid exothermic reaction (approximately 30°C increase during the first 0.1sec), and then decreases as the

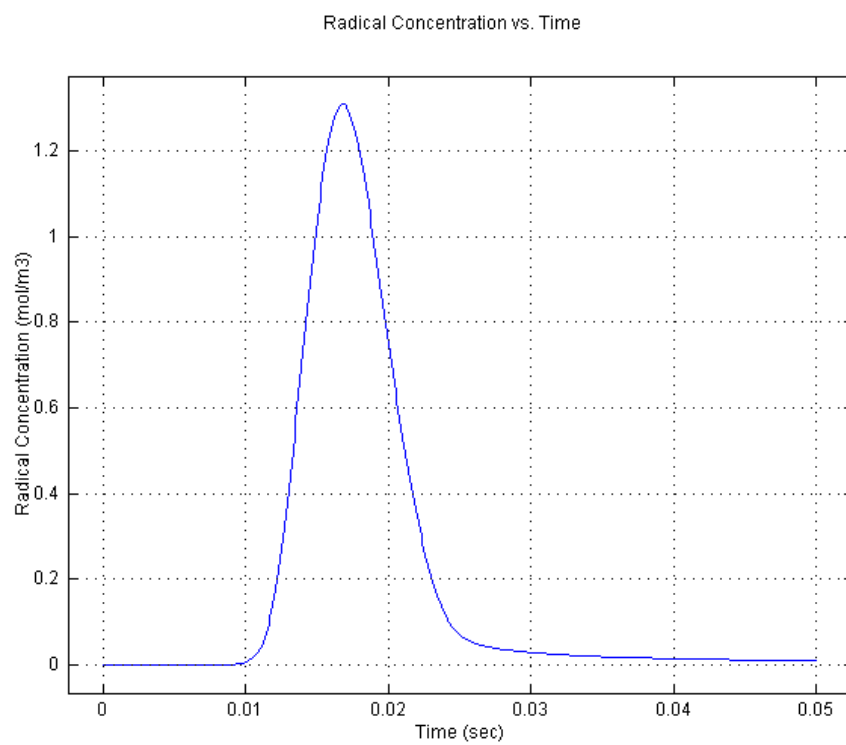
reaction slows down and heat conduction plays a role. Due to the very fast reactions, the radicals are rapidly exhausted and the monomer is consumed significantly in the first 0.1s as well. The transient intensity caused by laser movement (Figure 29a) has induced “Gaussian” radical concentration profile. In Figure 29, the laser directly exposes the investigated point at $t = 16\text{ms}$, which gives the highest intensity ($\text{mol/m}^2\text{-s}$) and leads to most consumption of the initiator and most generation of the radicals. The initial delay is due to the absence of irradiation. The initiator is consumed and the radicals are generated during the very short irradiation period. In the subsequent dark period, no more initiator is consumed to produce radicals.



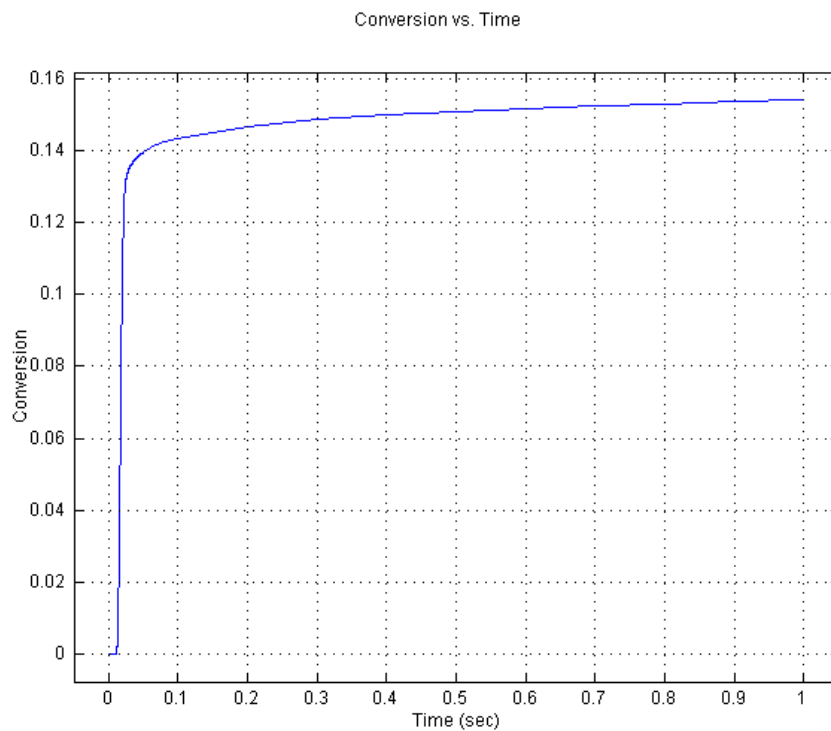
(a)



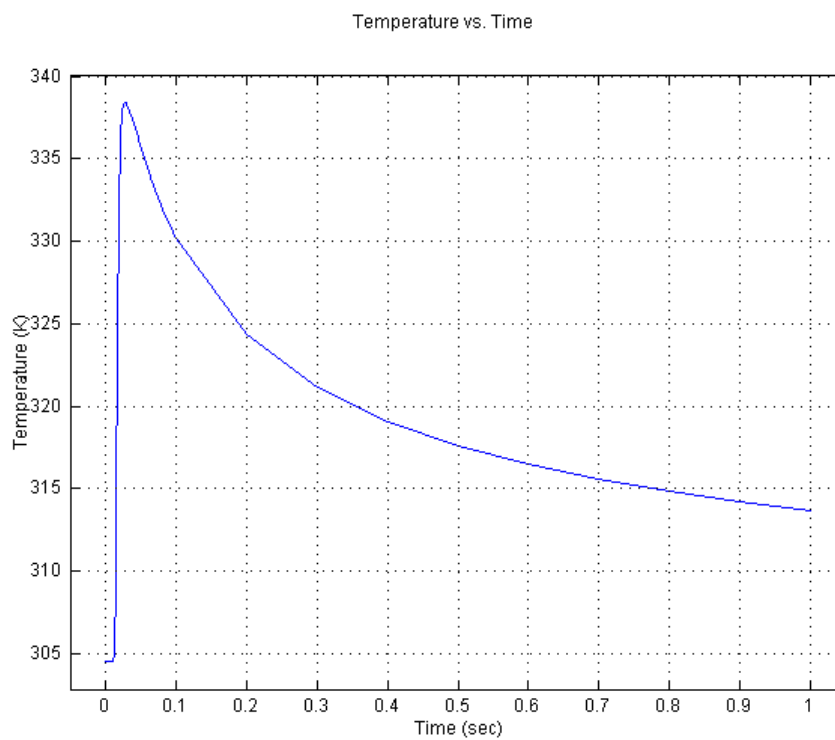
(b)



(c)



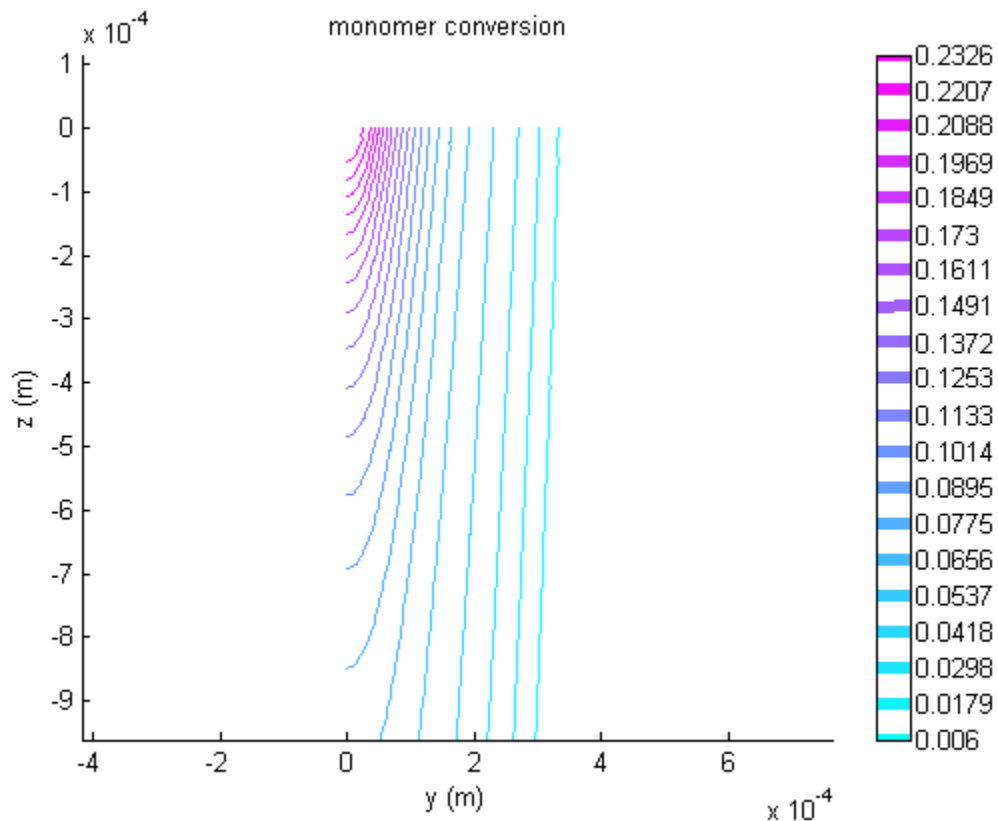
(d)



(e)

Figure 29 Transients of (a) Intensity, (b) Initiator Concentration, (c) Radical Concentration, (d) Monomer Conversion, and (e) Temperature at Point (x, 0, 0)

Figure 30 shows when the radicals are used up and the temperature returns to the bath temperature, the sectional view of the monomer conversion and initiator concentration profiles. Upon a single laser scan (with scan conditions listed in Table 6), a maximum of 25% monomer can be converted, which occurs at the center of the single line where the resin receives the most exposure and the most initiator is consumed. From the conversion contour in Figure 30 (a), it can be expected that the cross section of the cured line would be of bullet shape. Figure 30 (b) demonstrates the consumption status of the initiator after a single laser scan and half an hour of post-curing in the bath. A longer stay in the bath wouldn't lead to significant change to the initiator distribution due to the dark environment and extremely low diffusion.



(a)

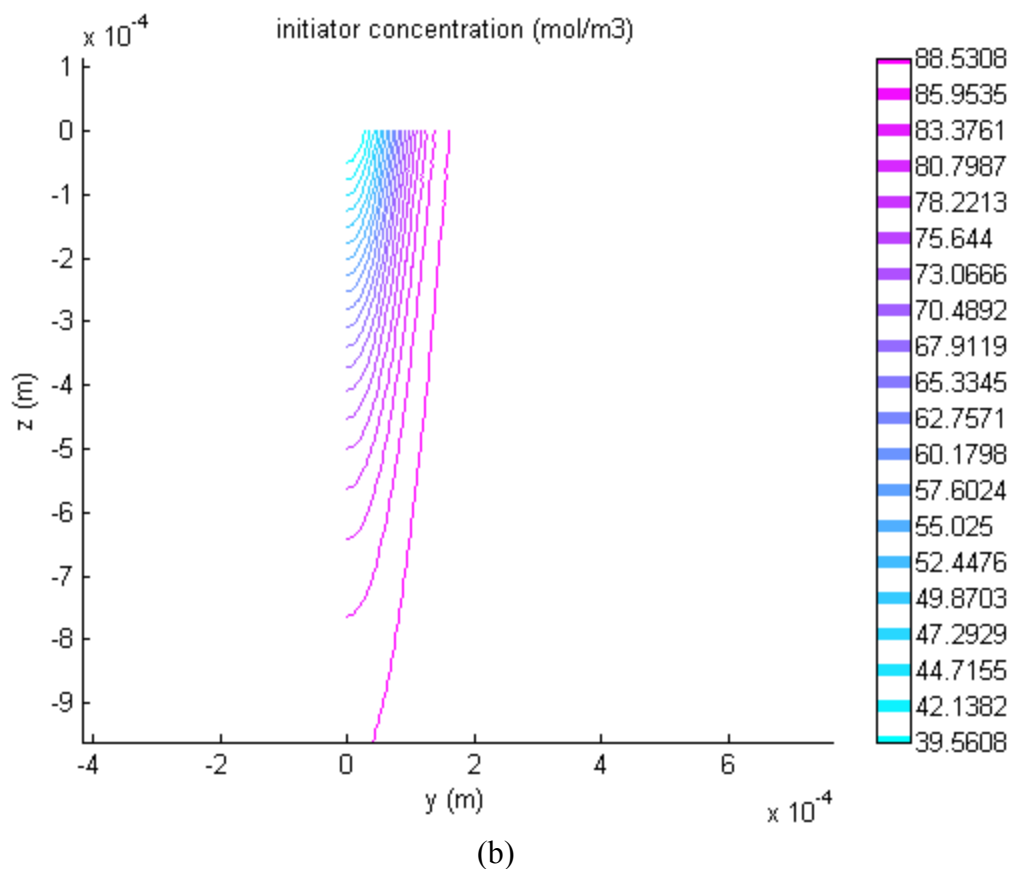


Figure 30 Distribution of (a) Monomer Conversion and (b) Photoinitiator Concentration upon a Single Laser Scan

Figures 31 and 32 demonstrate the evolution of monomer conversion along the width at the resin surface (y axis in Figure 2) and along the depth centerline (z axis in Figure 2) of the single line part, respectively. It can be seen that the reaction starts rapidly upon irradiation (as shown in Figure 29a, irradiation starts at $t = 0.01$ sec and ends at $t = 0.025$ sec). In about 20 ms, the reaction slows down in the dark. At the center of the irradiation ($y = 0$) where more radicals are generated during exposure, the dark reaction contributes to about 10% conversion of monomer.

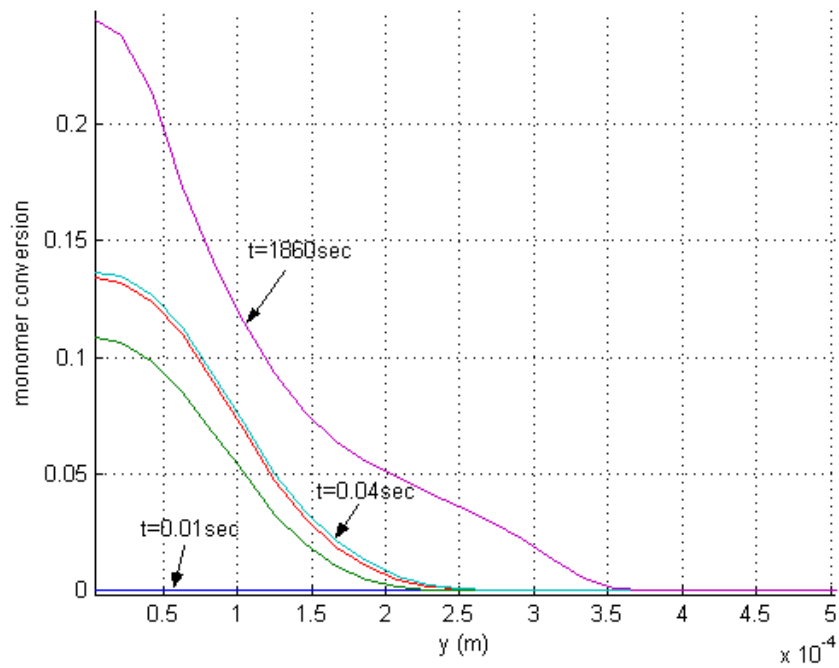


Figure 31 Monomer Conversion vs. Width at the Top Surface of the Single Line Part
(Plot Interval = 0.01 sec, except for $t = 1860$ sec)

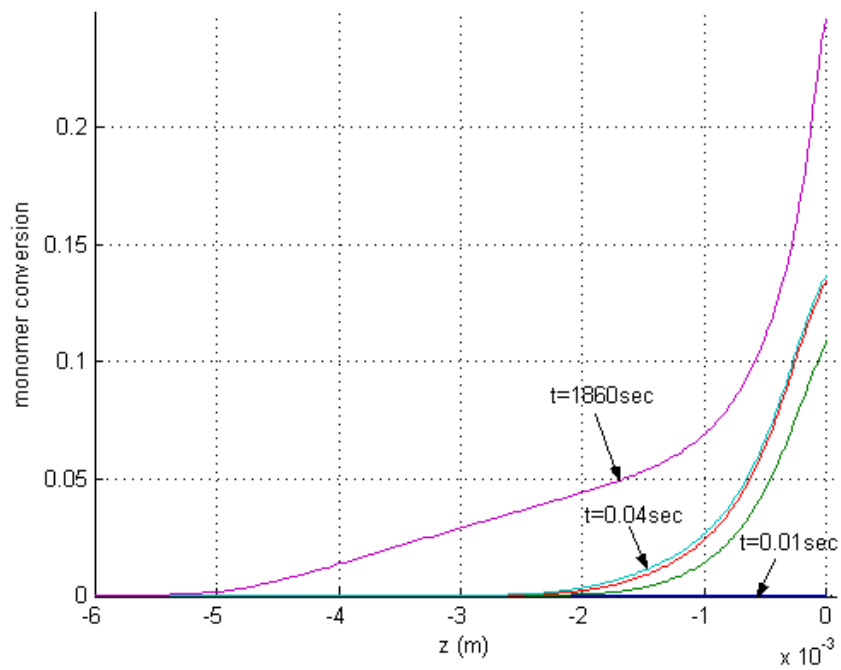


Figure 32 Monomer Conversion vs. Depth along the Centerline of the Single Line Part
(Plot Interval = 0.01 sec, except for $t = 1860$ sec)

5.2 Overlapping Lines

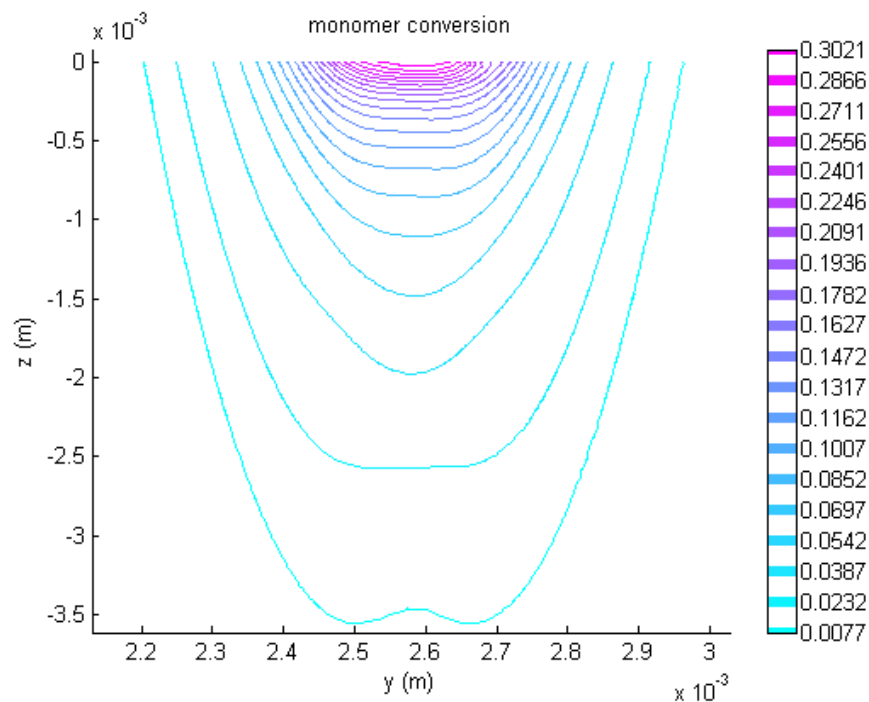
The governing equations established for single laser drawn line in Chapter 2 are also valid for the overlapping line case, while the domain and boundary conditions need to vary accordingly to accommodate multiple lines. The full cross section of the drawn overlapping lines (rather than half cross section investigated in single line case where symmetry can be easily determined) is considered here. As for the single line case, the 3D problem is reduced to a 2D one due to, ignoring the line ends, the repetitive cure behavior along the laser scanning direction (x axis). The jump time of the laser from the end of one line to the start of a second line is negligible (within 1ms). With the same laser moving speed as in single line case (see Table 6), it takes about 940 ms to draw a single 1 inch line or pass the same x location for a second time.

The laser irradiation is imposed line by line. The curing situation upon previous drawing(s) is employed as the initial condition for the next scanning. Equation (52) describes the transient intensity profile for the nth line.

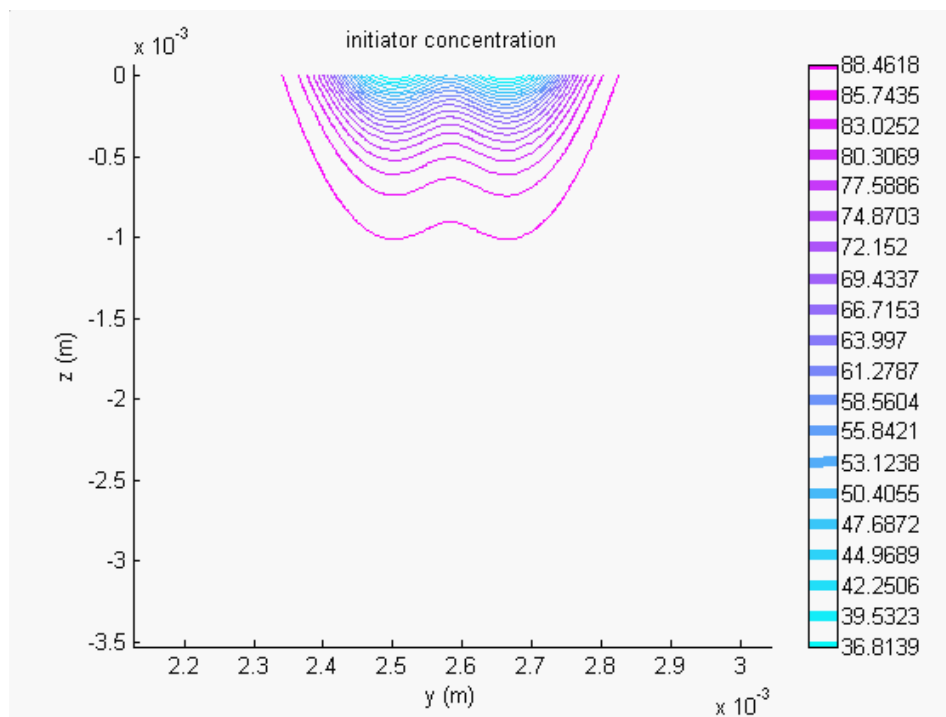
$$I = I_0 \exp\left\{-2\left[\left(V_s(t - (n-1)0.94 - t_0)\right)^2 + (y - 0.0025 - (n-1)h_s)^2\right]/w_o^2\right\} \exp(-z/D_p) \frac{\lambda(\text{nm})}{1.196 \times 10^8} \quad (52)$$

where I_0 is the maximum intensity incident on the resin surface (W/m^2), I is the intensity incident on any point (y, z) in the resin ($\text{mol/m}^2\text{-s}$), h_s is the hatching space (i.e. line spacing), 0.0025 is used to position the first drawn line in a 0.005 m wide domain, and the time point at which the laser starts to draw the first line is taken as $t = 0$.

Figure 33 demonstrates for two overlapping lines with hatching space $h_s = 1.5w_0$ when the radicals generated are used up and the temperature returns to bath temperature, the distributions of monomer conversion and initiator consumption. The monomer conversion and temperature rise are found to be up to 32 % and 40°C, while for the single line drawn with same speed and same laser power, they are 25 % and 30°C, respectively, as mentioned earlier. The size of the same conversion outline (indicating part size) in Figure 33 (a) is obviously larger comparing with that in Figure 30 (a). The initiator consumption profile in Figure 33 (b) represents the two adjacent laser irradiations, which, considering the limited diffusion in the crosslinked network, is basically Figure 30 (b) added with a second laser drawing at a h_s distance. However, in Figure 33 (a), the two scans cannot be easily distinguished from each other because the reaction also occurs in the joint area of the two scans. As the hatching space varies from large to small, the cured lines generated can be separated, with an uneven bottom surface, or with a flat bottom surface (as in this case). More discussions on superposition of adjacent scans and the effect of hatching space on the cured part shape can be found in Jacobs (1992).



(a)



(b)

Figure 33 (a) Monomer Conversion (b) Initiator Concentration (mol/m^3) Distributions upon Two Overlapping Scans

Figure 34 demonstrates the evolution of monomer conversion along the width at the resin surface of the two-overlapping-line part. It can be seen that the second line grows rapidly (a noticeable increase in conversion is observed at the right of the first line) upon irradiation (as discussed earlier, the laser starts to draw the second line at $t = 0.94\text{sec}$). More monomer is converted in the first line region near the second line due to the extra exposure from the second line drawing. In about 20 ms, the reaction in all regions slows down in the dark. Similar to the single line case, the dark reaction contributes to about 10 % conversion of monomer at the locus where more irradiation is received.

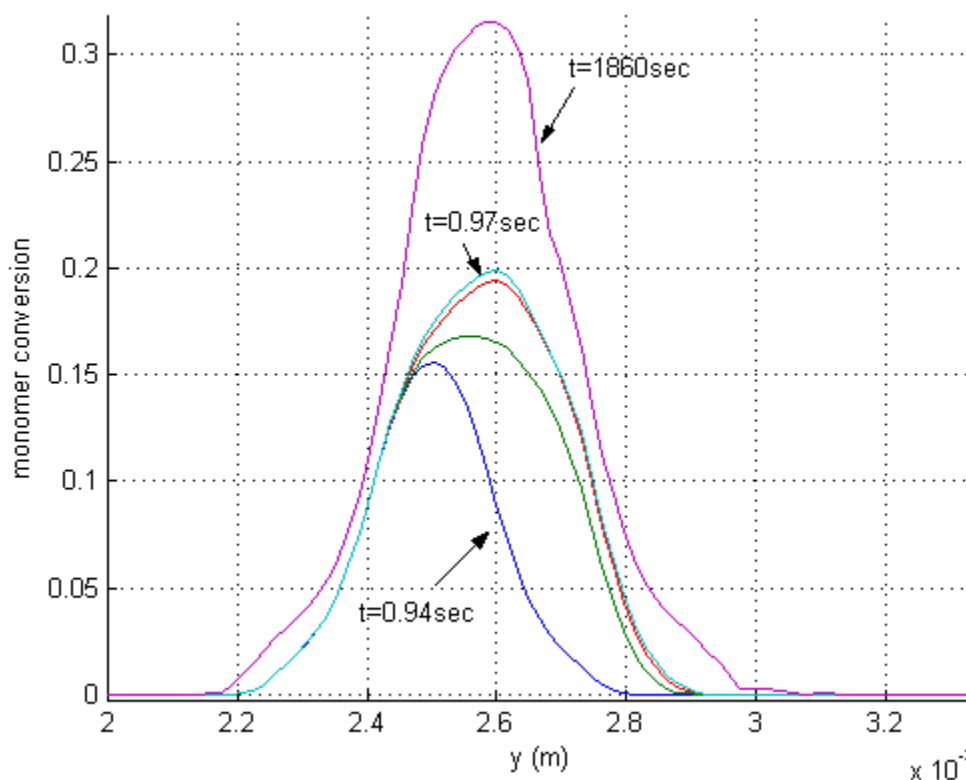


Figure 34 Monomer Conversion vs. Width at the Top Surface of Two-Overlapping-Line Part (Plot Interval = 0.01 sec, except for $t = 1860\text{ sec}$)

5.3 Stacked Single Lines

In this case, single lines are built layer by layer with each line drawn on the top of the previous one(s). The simulation of the first layer is exactly the same as of the single line case. Additional sub-domains for subsequent layers (or lines) are added layer by layer at the top of the previous domain. The depth of each sub-domain is the layer thickness. Also as in the single line case, the 3D problem is reduced to a 2D one due to, ignoring the edge effect, the repetitive cure behavior along the laser scanning direction (x-axis).

The laser irradiation is imposed layer by layer. The curing situation upon previous drawn layer(s) is employed as the initial condition for the next layer. The time delay between drawing two neighboring layers is estimated to be 40sec, including resin recoating and laser beam analyzing time. Equation (53) describes the transient intensity profile for the nth layer.

$$I = I_0 \exp\left\{-2\left[\left(V_s(t - (n-1)40 - t_0)\right)^2 + y^2\right]/w_o^2\right\} \exp[-(z - (n-1)L_T)/D_p] \frac{\lambda(\text{nm})}{1.196 \times 10^8} \quad (53)$$

where L_T is the layer thickness; the time point at which the laser starts to draw the first layer is taken as $t = 0$.

Figure 35 demonstrates for two stacked lines with layer thickness $L_T = 4$ mils when the radicals generated are used up (except the small amount of radicals trapped in the first layer due to high crosslinking) and the temperature returns to bath temperature, the distributions of monomer conversion and initiator consumption. The monomer conversion and temperature rise are found to be up to about 40 % and 35 °C, respectively,

comparing with 25 % and 30 °C for the single line drawn with same speed and same laser power. The same conversion outline (indicating part size) in Figure 35 (a) is obviously wider and deeper than that in Figure 30 (a) as well. The maximum monomer conversion and initiator consumption obviously occur in the first layer near the joint boundary where the resin receives the maximum exposure during the first laser scan and still receives extra exposure during the second scan. Two layers can be easily distinguished from each other as shown in Figure 35, which, however, doesn't necessarily mean that these two layers are separate physically. The cure at the joint area could be enough to hold two layers together. The layer thickness affects how well the two adjacent layers are attached to each other. Too large of a specified layer thickness causes two layers to partially join together or even separate; too small a layer thickness makes two layers well connected, however, it increases the part building time.

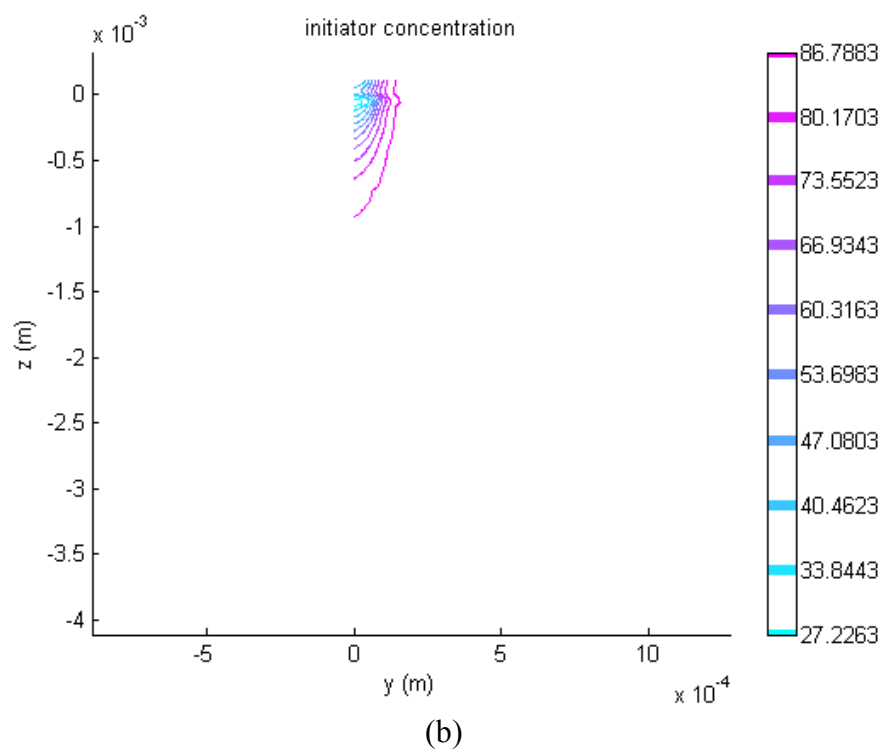
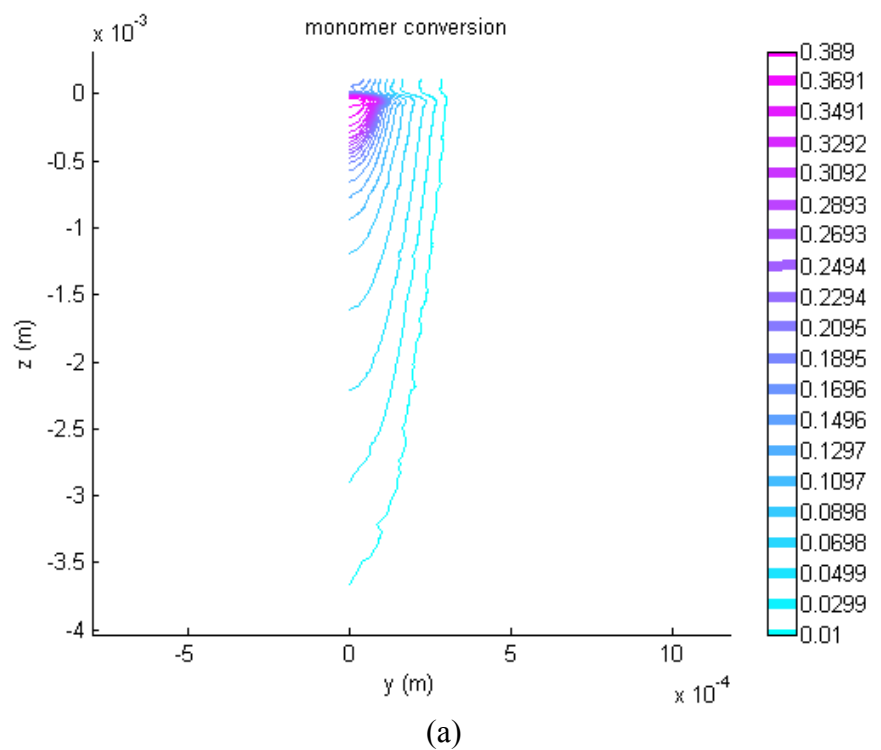


Figure 35 (a) Monomer Conversion (b) Initiator Concentration (mol/m^3) Distributions upon Two Stacked Scans

Figure 36 demonstrates the evolution of monomer conversion along the centerline in depth of the two-layer-line part. It can be seen that the second line grows rapidly (a noticeable increase in conversion is observed at the top of the first line) upon irradiation (as discussed earlier, the laser starts to draw the second line at $t = 40$ sec). More monomer is converted in the first layer region near the second layer due to the extra exposure from the second line drawing. In about 20 ms, the reaction in all regions slows down in the dark. Similar to the single line case, the dark reaction contributes to about 10 % conversion of monomer at the locus where more irradiation is received. As shown in Figure 36, the maximum $+z = 1 \times 10^{-4}$ m (the top surface of the first layer is at $z = 0$), verifying the second layer at the top of the first one is 4 mils (layer thickness) thick.

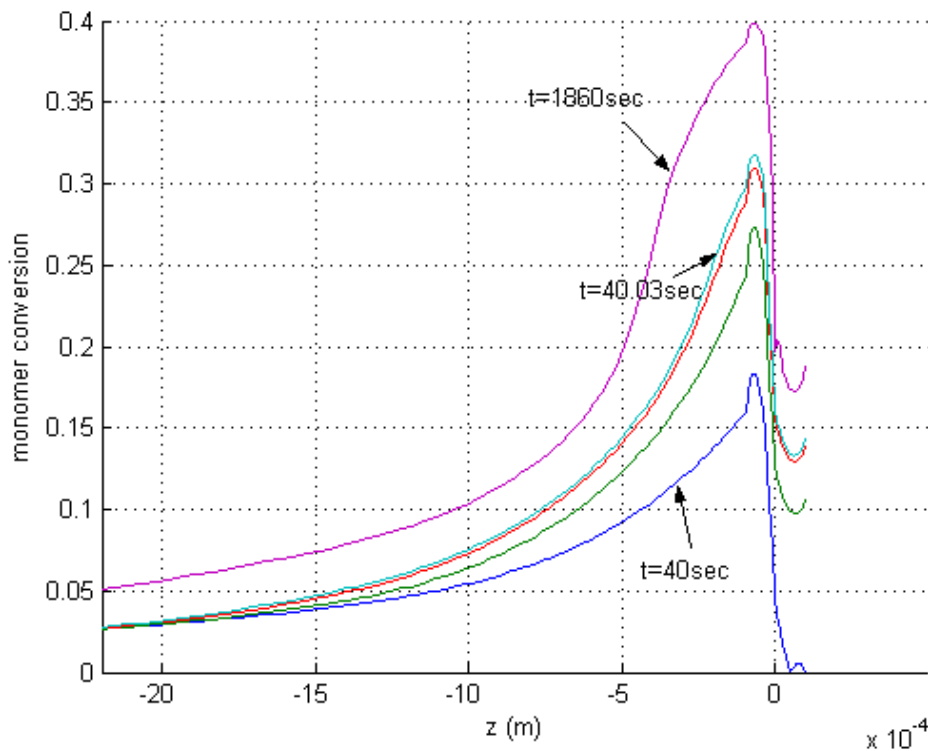


Figure 36 Monomer Conversion vs. Depth at the Centerline of Two-Layer-Line Part (Plot Interval = 0.01 sec, except $t = 1860$ sec)

CHAPTER 6

MODEL VERIFICATION

To verify the process model, the single-line, overlapping-line, and stacked-line parts have been fabricated in SLA and their dimensions measured to compare with the simulation results. It's found that a certain degree of cure (DOC) contour outlines the built part within minimal error. For this reason, the SL cure process model established and solved earlier can also be referred to as a "DOC threshold model" when used to predict the fabricated part shape and dimensions. This DOC threshold model is valid not only for single line parts, but for overlapping-line and stacked-line parts. While the exposure threshold model predicts the cured part dimensions with up to 50% error, this model has reduced the prediction error to 25 %.

6.1 DOC Threshold Model

The E4PETeA acrylate with 2 wt % DMPA initiator was used to grow single line parts in SLA-250/50. The parts were elevated out of the resin vat 30 minutes after laser scanning was finished, and drained on the platform for another 15 minutes. They were cleaned for one minute in TPM (tri-propylene glycol monomethyl ether) and another minute in water at room temperature using a Branson 5210 cleaning system in ultra-sonic mode. The parts were then dried using compressed air and broken to expose their cross sections, the image and dimensions of which were taken and measured by scanning electron microscopy (SEM, Hitachi S800 FEG). The SEM measurements were calibrated

using a standard grid with known dimensions. Figure 37 shows a typical image of the cross section of a single line part, which as expected is of parabolic shape.

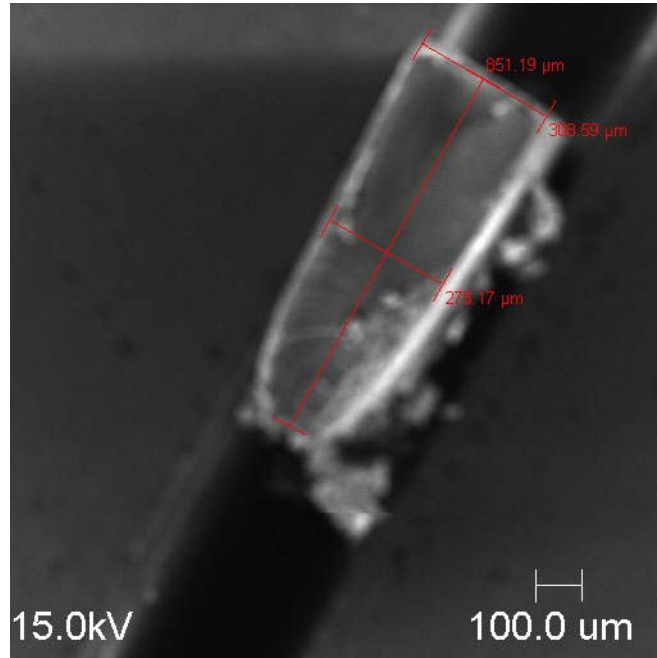


Figure 37 SEM Image of Cross Section of a Single Line Part

The part building process has then been simulated and Figure 38 gives the DOC contour of the built part which corresponds to half the image in Figure 37. For this single line part, the outline is close to the 9% DOC contour. The DOC corresponding to this contour line is defined as the critical DOC, above which the solid part can be formed while below this DOC the resin has not been solidified enough and can be washed away during the postprocessing step. In this sense, the SL cure process model developed in this work can also be referred to as a DOC threshold model. Unlike the exposure threshold model which only incorporates the exposure, the DOC threshold model takes the reaction and transient intensity effects into account.

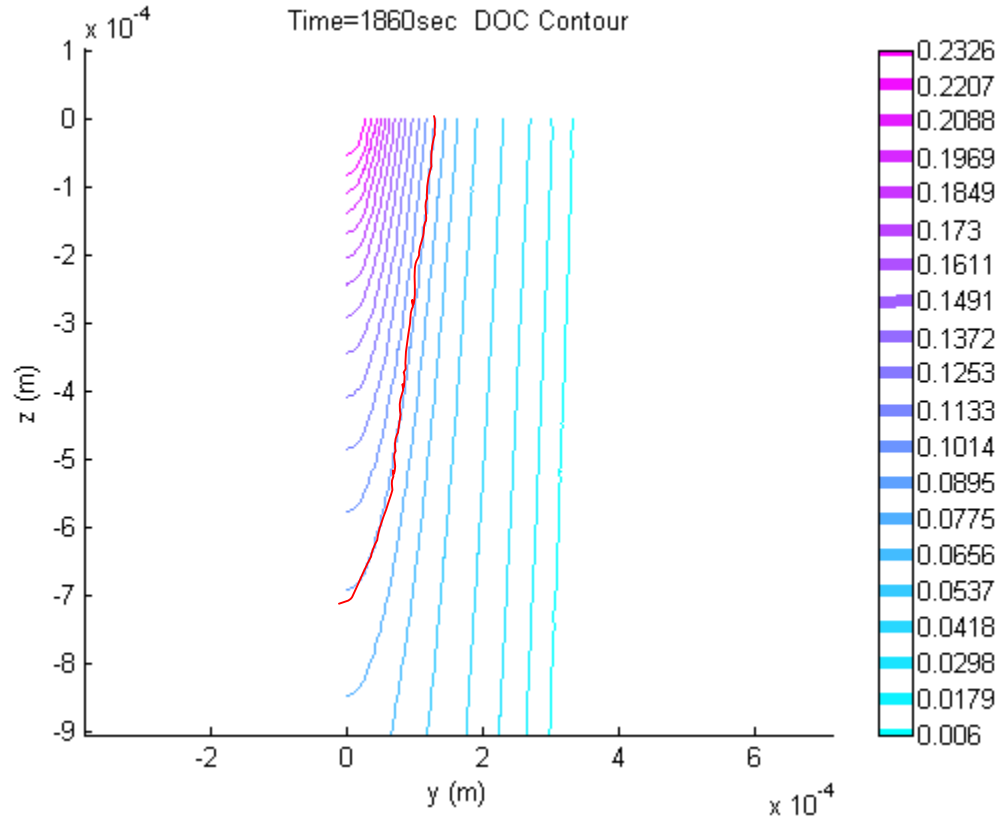


Figure 38 Degree of Cure Contour for Parts Built at $V_s = 1.071 \text{ in/sec}$ (with the measured part contour shown in red)

About 20 single line parts were built and measured at the laser drawing speed $V_s = 1.071 \text{ in/sec}$ (the scanning speed needs to be low enough for such a small part as a single line to be formed as well as be strong enough to handle and measure). Their measured outlines fall between the $\sim 9\%$ and $\sim 10\%$ DOC contours (Figure 38 shows a case where it overlaps with the 9% DOC contour), which defines the range of the critical DOC. This range can be applied to the simulated DOC profile to predict the cured part dimensions. The critical DOC is lower than the gel point of the curing material ($\sim 14\%$, Appendix C), which indicates that the cured polymer does not have to achieve an infinite molecular weight to form a solid part.

The part building process has to be consistent in order for the fabricated parts to have predictability. Obviously different part cleaning procedures could cause differences in the part size or shape, therefore, it is important that parts be fabricated consistently, i.e. following exactly the same building and postprocessing steps. On the other hand, it's not necessary to stick with the operating procedures described above. A different set of postprocessing steps can be adopted, which could give a different value for the critical DOC, but wouldn't affect the prediction of the DOC threshold model. The part building and cleaning procedure itself is not important; the consistency is important, i.e., the steps have to be followed consistently once they are designed and adopted.

6.2 DOC Threshold Model Prediction

Three types of parts have been built and measured to verify the SL cure process model or the prediction capability of the DOC threshold model: single line parts, overlapping cured lines (nine lines), and stacked single lines (three layers).

6.2.1 Single Line Part Prediction

The single line parts have also been built at a laser scanning speed of 0.466 in/sec. To verify the size of these parts is different from that of those built at $V_s = 1.071$ in/sec, the pairwise comparison (Neter et al., 1996) has been used:

$$\begin{aligned} H_0 : D &= \mu_i - \mu_{i'} = 0 \\ H_a : D &= \mu_i - \mu_{i'} \neq 0 \end{aligned} \tag{54}$$

where μ_i is the mean of the i th part dimension (here $i = 1$ for $V_s = 1.071$ in/sec and $i = 2$ for $V_s = 0.466$ in/sec), and D is the difference between the two means. The t test is utilized to decide to conclude H_0 or H_a , i.e., to conclude to support or to not support the hypothesis that the part dimensions fabricated at these two scanning speeds are the same. As shown in Table 7, for both part depth and width the magnitude of test statistics t^* is much greater than $t(0.9995, 36) = 3.589$. Therefore, H_a is concluded with 99.9 % or higher confidence. Parts built at $V_s = 0.466$ in/sec have different (larger) size than those built at $V_s = 1.071$ in/sec.

Table 7 Dimensions of Single Line Parts Built at Two Laser-Scanning Speeds:
1. $V_s = 1.071$ in/sec; 2. $V_s = 0.466$ in/sec

scanning speed i	Depth (μm)		Full Width (μm)	
	$i = 1$	$i = 2$	$i = 1$	$i = 2$
Measurement	724	922	262	311
	703	945	275	309
	761	963	268	317
	738	899	266	321
	763	901	259	349
	762	956	265	272
	738	951	256	324
	727	980	268	329
	753	958	256	332
	741	988	267	277
	725	990	260	335
	727	978	267	333
	757	945	273	302
	759	907	261	316
	768	998	255	347
	757	972	275	331
	774	1008	283	334
	737	964	260	345
		938		328
		982		334
average	745	957	265	322
Difference	-212		-57	
MSE	706.65		247.54	
t*	-24.56		-11.15	

The building process at a laser moving speed $V_s = 0.466$ in/sec has also been simulated. The critical DOC range (9~10%) is applied to the DOC profile to predict the cure depth and cure width. They are found to be in good agreement with the fabrication results (Table 8). The prediction error is defined as follows:

$$\text{prediction error} = \frac{\text{simulated value} - \text{experimental value}}{\text{experimental value}} \times 100\% \quad (55)$$

Table 8 Single Line Part Prediction by DOC Threshold Model

V_s (in/sec)	depth (μm)				full width (μm)			prediction error (%)
	experiment (95% C.I.)	critical DOC	Xc model	prediction error (%)	experiment (95% C.I.)	critical DOC	Xc model	
1.071	745 ± 10	9%	660	-10	265 ± 4	9%	260	-2
		10%	560	-25		10%	236	-10
0.466	957 ± 15	9%	1050	10	322 ± 10	9%	322	0
		10%	940	-2		10%	306	-5

*Xc model: DOC threshold model; C.I.: confidence interval

Part building at a higher scanning speed of 10.71 in/sec was attempted. It turns out, however, that the resin is not cured enough to form a solid part. The simulation for this faster writing speed process also demonstrates that the part cannot be formed. Figure 39 shows DOC contours for the 10.71 in/sec scanning speed. No DOC above 7% is observed anywhere in the simulated vat, and thus since this is lower than the required 9% DOC no solid polymer structure is predicted. This agreement also demonstrates and verifies the model's predictive ability.

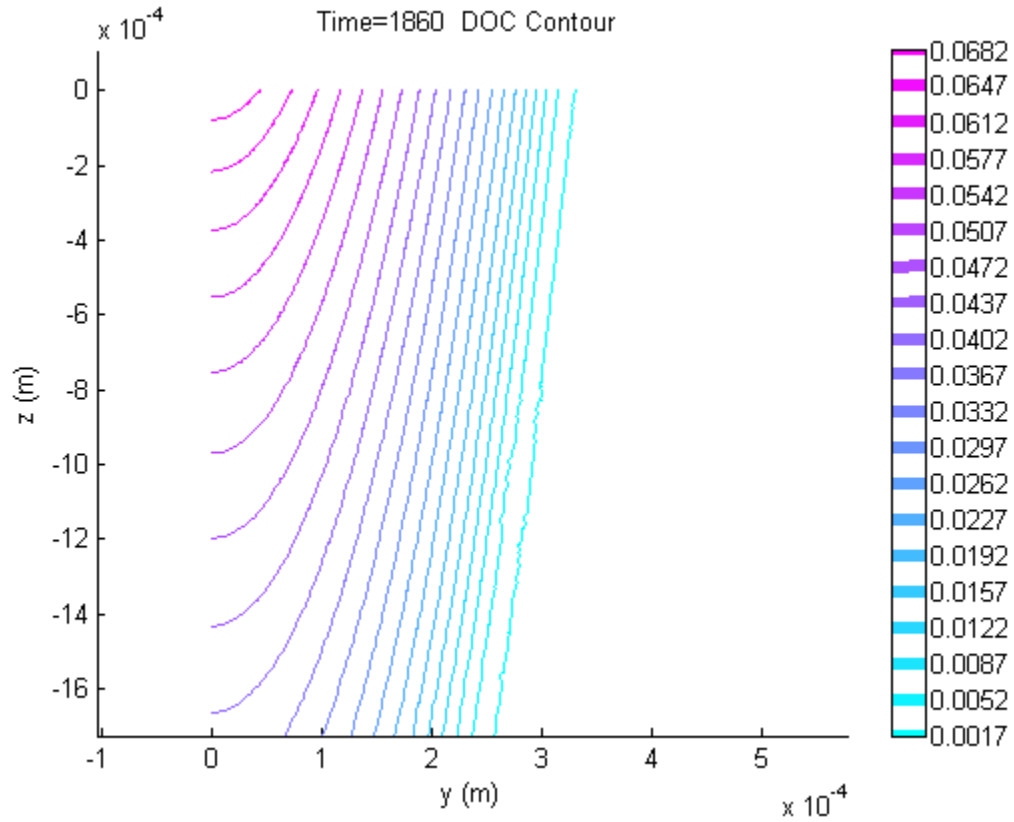


Figure 39 Degree of Cure Contour for Parts Built at $V_s = 10.71$ in/sec

6.2.2 Overlapping Line Part Prediction

The overlapping line parts have been built at $V_s = 17.967$ in/sec and with a hatching space $h_s = 0.5$ mils. The shape of the cured lines is similar to that of the single cured line due to the narrow line spacing and limited number ($n = 9$) of drawn lines. The size is larger as shown in Table 9.

Table 9 Dimension Measurements of Overlapping Line Parts

Measurement	Depth (μm)	Full Width (μm)
	1457	429
	1406	435
	1442	467
	1449	463
	1412	431
	1370	446
	1446	467
	1004	494
	1429	455
	1454	519
	1432	434
	1042	563
	1346	406
	1431	513
Mean	1349	468
Standard Deviation	149.7	43.0
Coefficient of Variation	0.1	0.09
Half Length of 95% C.I.	86	25
Lower Limit	1278	448
Upper Limit	1420	489

This multiple-line part building process is simulated and the critical DOC is applied to the DOC contour plot. The predicted dimensions are within 25 % of the experimental measurements, as shown in Table 10.

Table 10 DOC Threshold Model Prediction for Overlapping Line Parts

depth (μm)				full width (μm)			
experiment (95% C.I.)	critical DOC	Xc model	prediction error (%)	experiment (95% C.I.)	critical DOC	Xc model	prediction error (%)
1349 \pm 86	9%	1220	-10	468 \pm 25	9%	364	-20
	10%	1120	-20		10%	349	-25

*Xc model: DOC threshold model; C.I.: confidence interval

6.2.3 Stacked Line Part Prediction

The 3-layer stacked single line parts have been built at $V_s = 1.052$ in/sec and with the layer thickness $L_T = 4$ mils. The cured lines have similar shape to the single cured line with deeper and wider size. The dimension measurement results are shown in Table 11.

Table 11 Dimension Measurements of 3-Layer Stacked Line Parts

Measurement	Depth (μm)	Full Width (μm)
	977	347
	1146	341
	951	356
	1257	335
	1178	319
	1108	326
	1073	376
	995	362
	904	338
	941	361
	932	353
	1021	365
	1018	358
	1044	345
	1040	326
	890	342
	945	367
Mean	1025	348
Standard Deviation	101.8	16.0
Coefficient of Variation	0.1	0.05
Half Length of 95% C. I.	52	8
Lower Limit	982	341
Upper Limit	1068	355

This layer-by-layer part building process is simulated and the critical DOC is applied to the DOC contour plot. The predicted dimensions are within 25 % of the experimental measurements, as shown in Table 12.

Table 12 DOC Threshold Model Prediction for 3-Layer Stacked Line Parts

depth (μm)				full width (μm)			
experiment (95% C.I.)	critical DOC	Xc model	prediction error (%)	experiment (95% C.I.)	critical DOC	Xc model	prediction error (%)
1025 ± 52	9%	1285	25	348 ± 8	9%	346	-1
	10%	1150	10		10%	330	-5

*Xc model: DOC threshold model; C.I.: confidence interval

The prediction results of all three types of cured lines using DOC threshold model have been demonstrated. The good agreement between experimental results and simulation results (within 25 % error) validates the SL cure process model (i.e. DOC threshold model). The critical DOC taken outside the 9~10% range leads to high prediction error.

6.3 Exposure Threshold Model Prediction

The exposure threshold model has been widely used to guide the SL prototyping in industry. As mentioned earlier, it assumes a critical exposure, E_c , is necessary for a part to be formed. The cure depth, C_d , and linewidth, L_w , (referring to the maximum depth and width of the cured line, respectively) can be obtained from the following (Jacobs, 1992):

$$C_d = D_p \ln\left(\frac{E_{\max}}{E_c}\right) \quad (56)$$

$$L_w = 2w_0 \sqrt{\frac{C_d}{2D_p}} \quad (57)$$

where E_{max} is the maximum exposure incident on the resin surface centerline during laser scanning, w_0 is the laser beam radius, and D_p is the penetration depth of the laser into the resin at which the irradiance would be about 37 % of the surface irradiance. E_c and D_p are regarded as the resin characteristic parameters and can be determined from WINDOWPANETM experiments (Jacobs, 1992).

6.3.1 E_c and D_p Determination

In SLA-250/50, the WINDOWPANETM experiments were conducted to characterize E_c and D_p of the model acrylate resin. The laser drawing speed was varied to achieve a wide range of cure depth. According to Equation (56), the best linear fit was performed in the semilog plot of cure depth, C_d , versus maximum exposure, E_{max} , as shown in Figure 40. E_c and D_p were thus found to be 7.22 mJ/cm² and 9.43 mils, respectively, for the model resin: E4PETeA acrylate with 2 wt % DMPA.

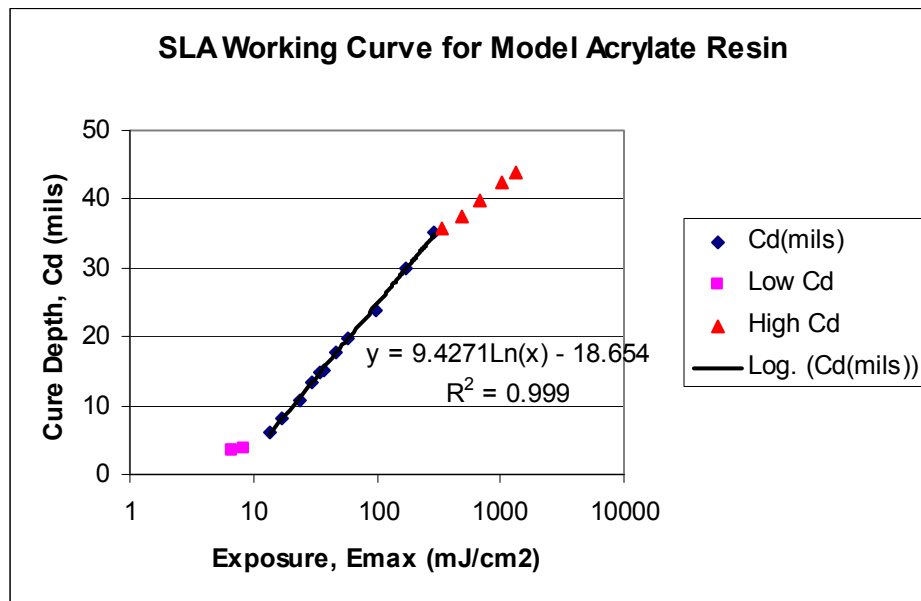


Figure 40 Working Curve from WINDOWPANETM Experimental Data

The “reverse WINDOWPANETM” experiments (Jacobs, 1992) were performed to verify the determined E_c and D_p values. The SL system uses these two values and sets the desired cure depth for part building. The test parts were built, measured, and then compared to the specified cure depth. It turned out that all cure depth values of the produced windowpane parts are within 1 mil of the specified values, which guarantees the correctness of E_c and D_p values determined above.

6.3.2 Single Line Part Prediction

Equations (56) and (57) have been used to calculate the cure depth and full width of the cured line. For a single drawn line, the maximum exposure incident on the resin surface can be expressed as follows (Jacobs, 1992):

$$E_{\max} = \sqrt{\frac{2}{\pi}} \frac{P_L}{w_0 V_s} \quad (58)$$

Table 13 shows the calculated results for the case of single line parts. Obviously the exposure threshold model has much larger prediction error than DOC threshold model (within 25% error), with up to 50% for the depth and 27% for the width.

Table 13 Single Line Part Prediction Results Based on Exposure Threshold Model

V_s (in/sec)	depth (μm)			full width (μm)		
	experiment (95% C.I.)	Ec model	prediction error (%)	experiment (95% C.I.)	Ec model	prediction error (%)
1.071	745 \pm 10	1118	50	265 \pm 4	336	27
0.466	957 \pm 15	1310	37	322 \pm 10	364	13

*Ec model: exposure threshold model; C.I.: confidence interval

The error of the exposure threshold model to predict the cure depth is quite large. This is probably due to the inappropriate assumption of Gaussian laser beam intensity distribution. Figure 41 is a picture of beam intensity profile taken by a digital camera. It is apparent that the beam is not exactly a Gaussian distribution. The beam is not symmetric, either, and time-varying. The picture below shows the beam width ratio in two directions $X/Y = 1.08$.

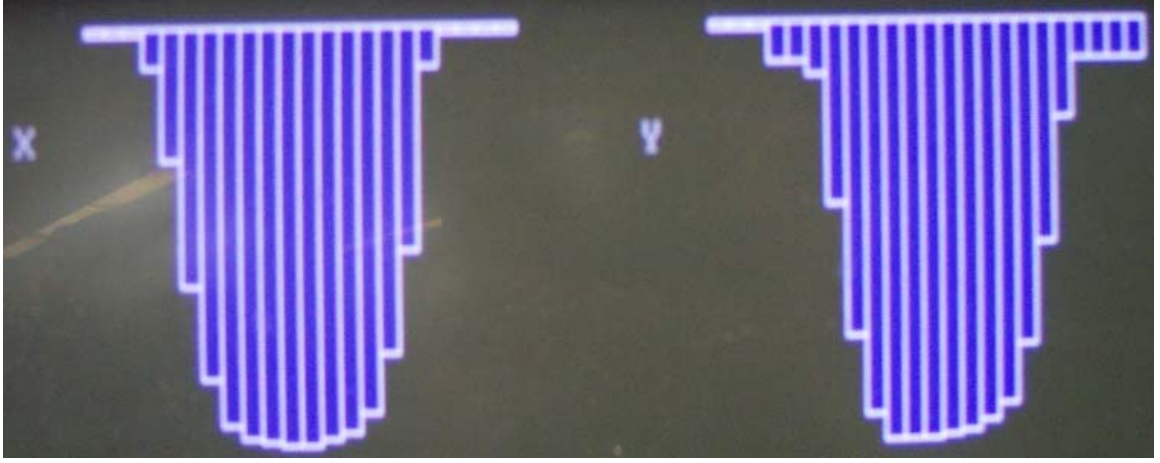


Figure 41 Beam Intensity Profile of HeCd Laser in SLA-250/50

To obtain a better simulation of the beam profile, a top-hat distribution is introduced:

$$I = \begin{cases} I_0 & 0 \leq r \leq w_0 \\ 0 & r > w_0 \end{cases} \quad (59)$$

The Gaussian assumption is modified by equally combining with the top-hat distribution as follows (i.e. taking the average of Gaussian and top-hat beam):

$$I = \begin{cases} 0.5I_0 \exp(-2r^2 / w_0^2) + 0.5I_0 & 0 \leq r \leq w_0 \\ 0.5I_0 \exp(-2r^2 / w_0^2) & r > w_0 \end{cases} \quad (60)$$

The integral of the surface irradiance over the exposed region must be equal to the laser power P_L incident on the resin surface. Therefore, the peak surface irradiance at $r = 0$ can be obtained as:

$$I_0 = \frac{4}{3} P_L / (\pi w_0^2) \quad (61)$$

The integration of the surface irradiance over time gives the surface exposure:

$$E(y,0) = \begin{cases} 0.5\sqrt{\frac{\pi}{2}} \frac{w_0 I_0}{V_s} \exp(-2y^2 / w_0^2) + \frac{I_0}{V_s} \sqrt{w_0^2 - y^2} & |y| \leq w_0 \\ 0.5\sqrt{\frac{\pi}{2}} \frac{w_0 I_0}{V_s} \exp(-2y^2 / w_0^2) & |y| > w_0 \end{cases} \quad (62)$$

Furthermore, the following equation gives the exposure into any depth z :

$$E(y,z) = E(y,0) \exp(-z / D_p) \quad (63)$$

Applying the critical exposure E_c to the above equation, the cure depth can be obtained by setting $y = 0$ and the linewidth obtained by setting $z = 0$.

As seen in Table 14, a better prediction can be achieved using the equally weighted combination beam than using a pure Gaussian or a pure top-hat distribution. Varying the weighting factors doesn't improve the prediction accuracy because more weighted top-hat distribution increases the width prediction error without reducing the depth error significantly, and more weighted Gaussian distribution increases error in both depth and width. It can also be observed that even the improved exposure threshold model prediction results are not as good as those of the DOC threshold model using the raw Gaussian beam. This also indicates a relatively low requirement of the DOC threshold model for beam profile simulation accuracy comparing with the exposure threshold model. On the other hand, a better simulation of beam profile might improve the prediction of the DOC threshold model as well.

Table 14 Exposure Threshold Model Prediction Results using Modified Beam Profile

$V_s = 1.071$ in/sec	depth(μm)	prediction error (%)	full width(μm)	prediction error (%)
Experiment (95% C.I.)	745 ± 10		265 ± 4	
Ec model (G beam)	1118	50	336	27
Ec model ($\frac{1}{2}\text{G} + \frac{1}{2}\text{T}$ beam)	1076	44	293	10
Ec model (T beam)	1064	43	220	-17
$V_s = 0.466$ in/sec	depth(μm)	prediction error (%)	full width(μm)	prediction error (%)
Experiment (95% C.I.)	957 ± 15		322 ± 10	
Ec model (G beam)	1310	37	364	13
Ec model ($\frac{1}{2}\text{G} + \frac{1}{2}\text{T}$ beam)	1276	33	325	1
Ec model (T beam)	1256	31	220	-32

* G: Gaussian distribution; T: top-hat distribution; $\frac{1}{2}\text{G} + \frac{1}{2}\text{T}$: equally weighted combination of Gaussian and top-hat distribution.

6.3.3 Overlapping Line Part Prediction

As mentioned earlier, the exposure threshold model basically derives the exposure expression for a part building process, and then applies the critical exposure, which then gives the equation that calculates the outline of the cured part. Suppose the laser starts drawing at $y = 0$ (as shown in Figure 42), the exposure incident on any point of the resin Q when the laser draws n overlapping lines with hatching space h_s can be expressed as:

$$E(y, z) = \sqrt{\frac{2}{\pi}} \frac{P_L}{w_0 V_s} \left\{ \exp(-2y^2 / w_0^2) + \exp[-2(y + h_s)^2 / w_0^2] + \cdots + \exp[-2(y + (n-1)h_s)^2 / w_0^2] \right\} \exp(-z / D_p) \quad (64)$$

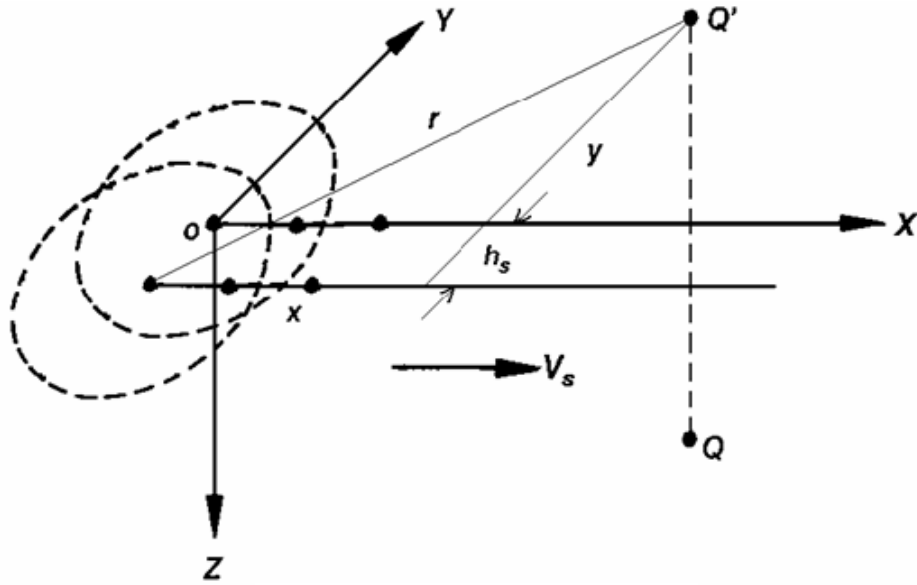


Figure 42 Laser Movement when Drawing Overlapping Lines

Letting $E(y, z) = E_c$, Equation (64) reduces to:

$$E_c = \sqrt{\frac{2}{\pi}} \frac{P_L}{w_0 V_s} \left\{ \exp(-2y^{*2} / w_0^2) + \exp[-2(y^* + h_s)^2 / w_0^2] + \dots + \exp[-2(y^* + (n-1)h_s)^2 / w_0^2] \right\} \exp(-z^* / D_p) \quad (65)$$

where y^* and z^* describe the outline of the cured part. When $z^*=0$, two values will be obtained for y^* : $+y_{\max}$ and $-y_{\max}$. The sum of their absolute values is the cured linewidth. Setting $y^*=0$, $-h_s$, $-2h_s$, ..., $-[\text{rounded}(n/2-1)] h_s$, the corresponding number of z^* values can be obtained as local maxima, the global maximum of which is the maximum cured depth of the part.

For the case of overlapping line parts with nine drawn lines $n = 9$ and hatching space $h_s = 0.5$ mils and laser scanning speed $V_s = 17.967$ in/sec (i.e. the example tested in section 6.2.2), $+y_{\max} = 126 \mu\text{m}$, $-y_{\max} = -227 \mu\text{m}$, and thus the cured linewidth turns out to be $353 \mu\text{m}$, which is 25 % smaller than the measured result. The cure depth is found to be $925 \mu\text{m}$, which underestimates the experimental value by 30 %. As discussed in section 6.2.2, the prediction errors for the part width and depth by the DOC threshold model are within 25 % and 20 %, respectively.

6.3.4 Stacked Line Part Prediction

When the laser draws n stacked single lines with layer thickness L_T , the exposure incident on the resin at the bottom layer can be expressed as (let $z = 0$ at the top layer surface):

$$E(y, z) = \sqrt{\frac{2}{\pi}} \frac{P_L}{w_0 V_s} \exp(-2y^2 / w_0^2) [\exp(-z / D_p) + \exp(-(z - L_T) / D_p) + \cdots + \exp(-(z - (n-1)L_T) / D_p)] \quad (66)$$

where $z = C_d$ when $y = 0$, letting $E(y, z) = E_c$. For the case of 3-layer stacked single line parts built at $V_s = 1.052$ in/sec and with layer thickness $L_T = 4$ mils (i.e. the example tested in section 6.2.3), the cure depth is calculated to be 1,497 μm , which overestimates the measured value by 46 %.

The exposure received at a point on the top of the n th layer is (Rosen, 2002):

$$E(y, (n-1)L_T) = \sqrt{\frac{2}{\pi}} \frac{P_L}{w_0 V_s} \exp(-2y^2 / w_0^2) [1 + \exp(-L_T / D_p) + \exp(-2L_T / D_p) + \cdots + \exp(-(n-1)L_T / D_p)] \quad (67)$$

Letting $E(y, (n-1)L_T) = E_c$, the maximum full width is calculated to be 336 μm at the top of the first layer, 354 μm at the top of the second layer, and 362 μm at the top of the third layer. This indicates that the width of the rib built by three stacked single vectors is not uniform. Although this stair effect is not distinguishable in the experimental results,

the exposure threshold model gives a good prediction of the rib width. None of these three values has deviated from the measured value by more than 5 %.

6.3.5 Comparison of DOC and Exposure Threshold Model

The predicted results by both the DOC threshold and exposure threshold models for all three building types (single line, overlapping lines, and stacked lines) are summarized in Table 15. The prediction error of the exposure threshold model is up to about 50 %, while the DOC threshold model can predict within 25 % error. For the cases tested here, the exposure threshold model appears to give better prediction of width than depth, which is probably due to the inappropriate assumption of a Gaussian laser beam. It also appears that the exposure threshold model is more sensitive to beam profile assumptions than is the new DOC threshold model.

Table 15 Comparison of Prediction Results by Two Threshold Models

<i>Single line part @ 1.071 in/sec</i>	depth (μm)	prediction error (%)	full width (μm)	prediction error (%)
Experiment (95 % C.I.)	745 ± 10		265 ± 4	
Xc model, Xc = 9 %	660	-10	260	-2
Xc = 10 %	560	-25	236	-10
Ec model	1118	50	336	30
<i>Single line part @ 0.466 in/sec</i>	depth (μm)	prediction error (%)	full width (μm)	prediction error (%)
Experiment (95 % C.I.)	957 ± 15		322 ± 10	
Xc model, Xc = 9 %	1050	10	322	0
Xc = 10 %	940	-2	306	-5
Ec model	1310	40	364	15
<i>Overlapping line part</i>	depth (μm)	prediction error (%)	full width (μm)	prediction error (%)
Experiment (95 % C.I.)	1349 ± 86		468 ± 25	
Xc model, Xc = 9 %	1220	-10	364	-20
Xc = 10 %	1120	-20	349	-25
Ec model	925	-30	353	-25
<i>Stacked line part</i>	depth (μm)	prediction error (%)	full width (μm)	prediction error (%)
Experiment (95 % C.I.)	1025 ± 52		348 ± 8	
Xc model, Xc = 9 %	1285	25	346	-1
Xc = 10 %	1150	10	330	-5
Ec model	1497	50	336	-5

*Xc model: DOC threshold model; Ec model: exposure threshold model; C.I.: confidence interval

One might argue that the exposure threshold model is also very dependent on what range of the working curve for the resin is used. Therefore, different regions of the working curve were fit and these new E_c and D_p values were used for the exposure threshold model prediction. For example, one option is to choose E_c and D_p in the higher working range, as shown in Figure 43. E_c and D_p are fit to be 0.98 mJ/cm² and 6.08 mils, respectively, in this range.

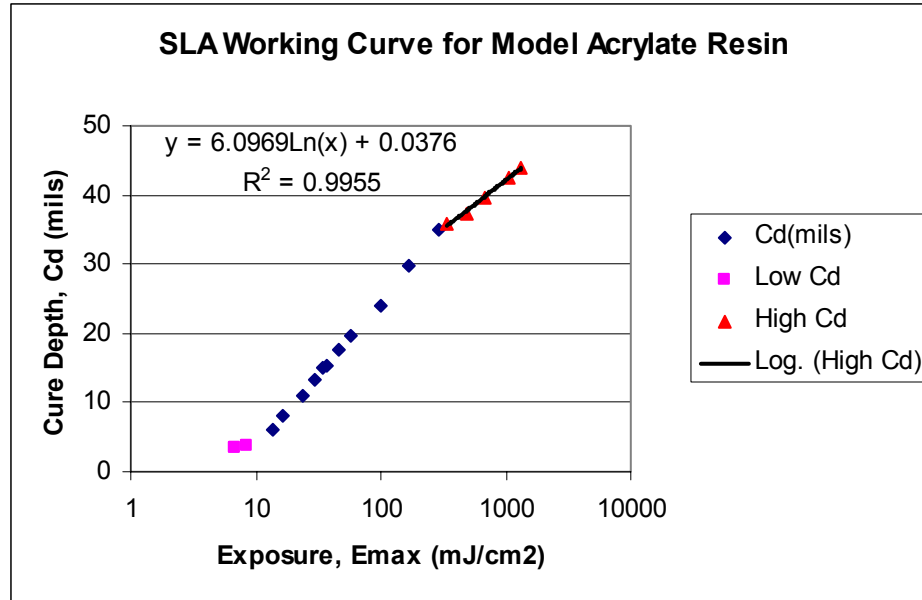


Figure 43 High Working Range for Model Acrylate Resin in SLA

However, the adoption of E_c and D_p from the higher working curve range of the resin doesn't improve the predictive ability of the exposure threshold model. As shown in Table 16, the prediction error is up to 40% for the cured depth and 50% for the part width.

Table 16 Exposure Threshold Model Prediction (high working range): 1. Single Line (1) $V_s = 1.071$ (2) $V_s = 0.466$ in/sec, 2. Overlapping-line, and 3. Stacked-line Parts

Line Type	depth (μm)			full width (μm)		
	experiment (95% C.I.)	E_c model	prediction error (%)	experiment (95% C.I.)	E_c model	prediction error (%)
1 (1)	745 ± 10	1029	40	265 ± 4	402	50
1 (2)	957 ± 15	1153	20	322 ± 10	425	30
2	1349 ± 86	905	-35	468 ± 25	430	-10
3	1025 ± 52	1322	30	348 ± 8	402	15

It should be mentioned that for the parts built and tested, the exposure doses fall in the higher range of the working curve. This indicates that in order to predict these part dimensions, the higher range of the curve should be used to determine E_c and D_p for the exposure threshold model. However, as we can see above, the adoption of the higher range of data gives similarly poor predictions.

6.3.6 Model Prediction using E_c and D_p Evaluated by a Different Protocol

In the previous sections where the exposure threshold model was used for part dimension prediction, the 3D Systems WINDOWPANE procedure¹⁰ was used to fabricate and post-process the windowpane parts to evaluate E_c and D_p . However, the washing procedure used in building parts or determining the critical DOC for our new DOC threshold model is different from the 3D systems WINDOWPANE procedure. Therefore, one might argue that the exposure threshold model would perform as well or better than the DOC threshold model if identical washing procedure was used. Therefore, in this study, an exposure threshold model was employed for part prediction in which E_c and D_p were determined by fabricating the windowpane parts using the same post-processing protocol as that for the DOC model development and regular part building (see 6.1 “DOC Threshold Model”). E_c and D_p were found to be 5.24 mJ/cm² and 9.48 mils, respectively (Figure 44). Recall when the 3D System’s procedure was used, E_c and D_p were found to be 7.22 mJ/cm² and 9.43 mils, respectively. As shown in Figure 44, two different protocols generated curves with similar slopes. This indicates that the depth of penetration, D_p , of the resin (the slope of the curve) does not depend on the post-processing procedure. This is expected because D_p is a characteristic property of the

¹⁰ AccuMax™ ToolKit User Guide for use with SLA-190, 250, 350, 500, 3D Systems.

resin, which is related to the molar concentration and absorptivity of the initiator in the resin, $D_p = 1/(2.3\epsilon S) = 9.59$ mils. Both D_p values obtained by these two different protocols are within 2% of this calculated value. The critical exposure, E_c (the natural log of E_c is proportional to the intercept of the curve), however, is found to be affected by the post-processing procedure significantly. This indicates that E_c is not an inherent property of the resin. For the same resin, it varies with the part processing procedure varying. E_c is an ambiguous concept, which leads to the poor predictive ability of the exposure threshold model which takes both E_c and D_p as the resin characteristics.

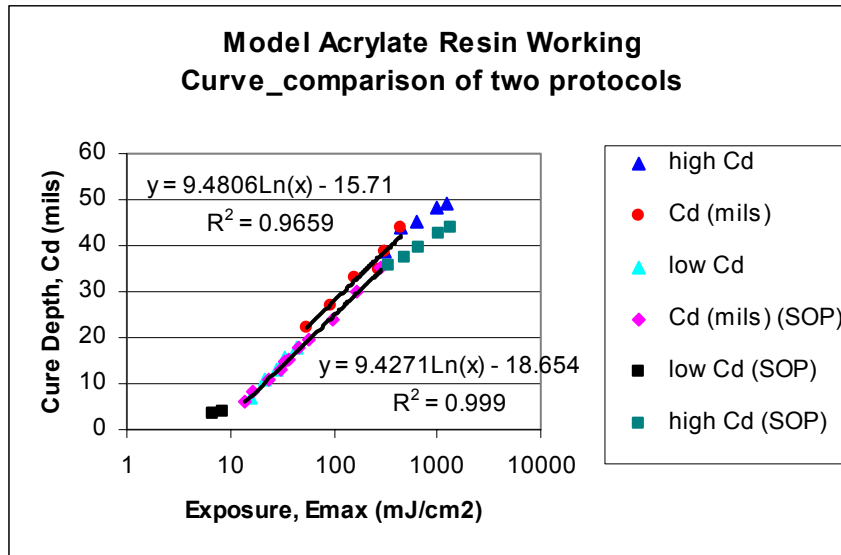


Figure 44 Comparison of Working Curves Obtained by the 3D Systems WINDOWPANE Procedure (labeled “SOP” in the figure) and by the Part Building Protocol

As shown in Figure 44, the correlation coefficient for the fitting is about 97%, while it is more than 99% when the 3D Systems’ procedure is used. The reverse windowpane parts were built using this set of E_c and D_p and it was found that the cured depth values

could be over 7 mils out of the nominal values (relatively, 15% different from the specified values). Recall when the 3D Systems WINDOWPANE procedure was used to determine E_c and D_p , all cure depth values of the produced windowpane parts were found to be within 1 mil of the specified values (within 5% of nominal values). These facts demonstrate that using the post-processing protocol is not an effective way to characterize the resin working curve due probably to the non-uniform effect of this protocol (draining, solvent washing, etc) on the part.

As shown in Table 17, the E_c and D_p characterization using the same post-processing step as the regular part building worsens the prediction of the exposure threshold model with the prediction error up to 60% (~10% less accurate than using the 3D Systems' procedure). This is expected since the resin properties (E_c and D_p) were not characterized properly by using this washing procedure as demonstrated by the poor predictive performance of the reverse windowpane parts. In the 3D Systems' procedure, rather than draining or washing using solvent and ultrasonic equipment or compressed air drying, after building the windowpane parts are placed with wet side (bottom side) down inside the SLA chamber (the heat inside the chamber is nearly optimum for the draining¹⁰) with the paper towel underneath. The paper towel strips are also placed with equal weights on top of parts (ideal weight for drainage is 10-13g¹⁰) to drain the excess resin. The parts are then put in the post-cure apparatus, PCA-250 (3D Systems), with dry side (top side) down on a clean glass plate for further cure. It can be seen that the 3D Systems' procedure is most likely much more effective at removing excess resin without damaging the parts than the post-processing steps used for regular part building. The ultrasonic vibration or air blowing used in our part building procedure may not clean the

windowpanes uniformly or they harm the cured dimensional uniformity. Such factors could cause the correlation of working curve and model prediction to be worse than those using E_c and D_p determined by the 3D Systems' procedure.

Table 17 Exposure Threshold Model Prediction (protocol): 1. Single Line (1) $V_s = 1.071$ in/sec (2) $V_s = 0.466$ in/sec, 2. Overlapping-line, and 3. Stacked-line Parts

Line Type	depth (μm)			full width (μm)		
	experiment (95% C.I.)	E_c model	prediction error (%)	experiment (95% C.I.)	E_c model	prediction error (%)
1 (1)	745 ± 10	1201	60	265 ± 4	347	30
1 (2)	957 ± 15	1395	45	322 ± 10	374	15
2	1349 ± 86	1007	-25	468 ± 25	367	-20
3	1025 ± 52	1581	55	348 ± 8	347	0

Again, one can argue about what range of the working curve to use. The adoption of the high range of the new working curve (Figure 45) produces an $E_c = 1.29$ mJ/cm² and $D_p = 7.25$ mils, but again this does not improve the model performance (Table 18).

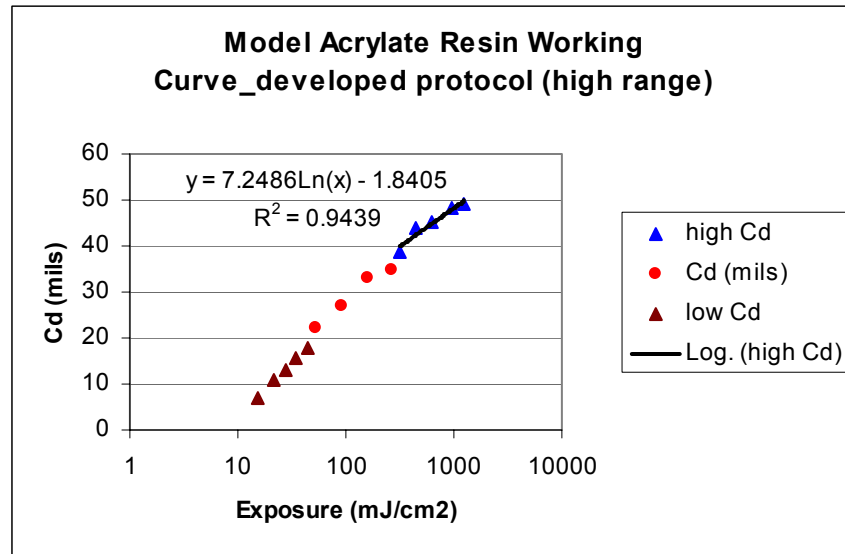


Figure 45 E_c and D_p Determined in the High Range using Part Building Protocol

Table 18 Exposure Threshold Model Prediction (protocol; high working range): 1. Single Line (1) $V_s = 1.071$ in/sec (2) $V_s = 0.466$ in/sec, 2. Overlapping-line, and 3. Stacked-line Parts

Line Type	depth (μm)			full width (μm)		
	experiment (95% C.I.)	Ec model	prediction error (%)	experiment (95% C.I.)	Ec model	prediction error (%)
1 (1)	745 ± 10	1177	60	265 ± 4	393	50
1 (2)	957 ± 15	1325	40	322 ± 10	417	30
2	1349 ± 86	1028	-25	468 ± 25	420	-10
3	1025 ± 52	1499	50	348 ± 8	393	15

Likewise, the adoption of the low range of the curve (Figure 46) produces an $E_c = 7.90$ mJ/cm² and $D_p = 10.51$ mils, and this does not improve the model predictions and in fact even makes them worse (Table 19).

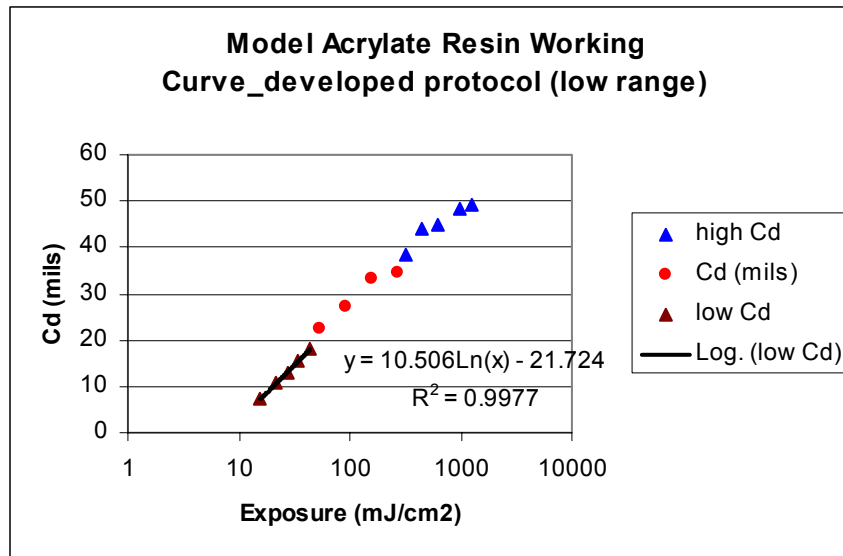


Figure 46 E_c and D_p Determined in the Low Range using Part Building Protocol

Table 19 Exposure Threshold Model Prediction (protocol; low working range): 1. Single Line (1) $V_s = 1.071$ in/sec (2) $V_s = 0.466$ in/sec, 2. Overlapping-line, and 3. Stacked-line Parts

Line Type	depth (μm)			full width (μm)		
	experiment (95% C.I.)	Ec model	prediction error (%)	experiment (95% C.I.)	Ec model	prediction error (%)
1 (1)	745 ± 10	1222	65	265 ± 4	332	25
1 (2)	957 ± 15	1436	50	322 ± 10	361	10
2	1349 ± 86	1007	-25	468 ± 25	349	-25
3	1025 ± 52	1630	60	348 ± 8	333	-5

It should be mentioned that for the parts built and tested, the exposure doses fall in the higher range of the protocol working curve. This indicates that in order to predict these part dimensions, the higher range of the curve (Figure 45) should be used to determine Ec and Dp for the exposure threshold model. However, as we can see above, the adoption of the higher range of data also gives similarly poor predictions.

6.4 Summary

The DOC threshold model was found to be more accurate at predicting the dimensions of single line and multiple line and stacked line parts than the current exposure threshold model. It was also found that evaluating Ec and Dp with the same post-processing as used in regular part building, or adopting different ranges of the resin working curve does not improve the predictive ability of the exposure threshold model, and in fact generally, makes it worse. A more accurate beam profile approximation does improve the predictions of the exposure threshold model, but it is still not as good as the DOC threshold model (about 20% less accurate, see Table 15). Furthermore, the new beam approximation makes the exposure threshold model more complex to utilize in SL.

CHAPTER 7

MODEL APPLICATIONS

As discussed earlier, given any part building condition, the DOC profile can be simulated and the critical DOC applied to predict the cured part dimensions. This capability of the SL cure process model (or critical DOC model) is not only a good verification but a good application of the model.

This chapter demonstrates that the process model can also be used to investigate the effects of material and process parameters on the SL performance, and identify factors that affect the fabrication results significantly. The material and process optimization can be performed for best performance, which also provides guidelines for SL material development and process or laser improvement.

The SL performance properties that are investigated and addressed in this chapter are the following: resolution, speed, maximum temperature rise in the resin bath, and maximum DOC of the green part (i.e. the part that is formed right after the SL building and has not been put in the post-cure apparatus, PCA, for further cure yet). Here SL resolution is defined as the dimensions of the smallest parts that can be obtained providing certain equipment and materials. The full width and maximum depth of a single cured line part hence are referred to as the width and depth resolution, respectively. Note the resolution decreases when the part size increases. The speed refers to the part curing speed only; the reduction of the speed by the building delay between layers, part draining and cleaning, etc., is not taken into account. The speed defined in the width (or

depth) direction is characterized by the time that is taken to obtain a single line part with certain width (or depth).

The software Minitab (Minitab Inc.) has been employed for parameter effect investigation and Evolver (Palisade Corporation) for parameter optimization.

7.1 Parameter Effect Investigation

Any of the parameters involved in the process model (as listed in Tables 1 and 4 in Chapter 3) could affect the SL fabrication results. Among these parameters, the effects of kinetic parameters are not investigated due to the complexity, their strong correlation with one another, and the variety of ways people have employed to describe the photopolymerization kinetics. The effect of CTE of the monomer is not tested either since it strongly affects the kinetic values f_{cp} and f_{ct} and thus its factorial effect cannot be tested without kinetic parameters also under investigation. This leaves 24 parameters to screen to identify the important ones. The resolution III Plackett-Burman design with 32 runs (corresponding to 2_{III}^{24-19} fractional factorial design, Neter et al. 1996) has been chosen for this purpose. Table 20 lists these 24 factors and their two level values which are determined based on SLA systems specifications (Rosen, 2002), polymer handbook (Brandrup and Immergut, 1989), acrylate monomer descriptions in Sartomer¹¹, photoinitiator descriptions in Ciba¹², polymer properties (Van Krevelen, 1990), Yaws' chemical handbook (Yaws, 2003), as well as experience and knowledge about SLA operations.

¹¹ www.sartomer.com

¹² www.cibasc.com

Table 20 Potential Sensitive Parameters and Their Level Values

Parameters	Symbols	Low Level (-1)	High Level (+1)	Units
laser scanning speed	Vs	0.02	0.1	m/s
bath temperature	Tb	301.15	308.15	K
laser power	PL	0.024	0.1	W
beam radius	wo	1.00E-04	2.00E-04	m
heat of polymerization	deltH	3.45E+04	2.85E+05	J/mol
absorption coefficient of initiator	ebx	20	60	m ³ /mol-m
quantum efficiency of initiation	phi	0.1	0.6	
Initiator wt% loading	wt	1	5	wt%
chamber temperature	Ta	296.15	303.15	K
heat convection coefficient	hfc	0	4.18	W/m ² -K
laser wavelength	wL	325	354.7	nm
thermal conductivity	cond	0.1	0.25	W/m-K
heat capacity (monomer)	CpM	1500	3300	J/Kg-K
heat capacity (polymer)	CpP	585	2500	J/Kg-K
diffusion coefficient (monomer)	Dm	1.00E-18	1.00E-10	m ² /s
diffusion coefficient (macroradical)	DR	1.00E-20	1.00E-12	m ² /s
diffusion coefficient (initiator)	Ds	1.00E-18	1.00E-10	m ² /s
CTE (polymer)	alphaP	7.50E-05	1.23E-04	1/K
glass transition temp. (monomer)	Tgm	173.15	223.15	K
glass transition temp. (polymer)	Tgp	373.15	497.6	K
density (monomer)	rouM	980	1128	Kg/m ³
density (polymer)	rouP	1200	1800	Kg/m ³
molecular weight (monomer)	MWm	0.198	2.156	Kg/mol
molecular weight (initiator)	MWs	0.164	0.418	Kg/mol

For each run of the Plackett-Burman experiment, six responses are recorded including width and depth resolution, curing speed defined in width and depth direction, maximum DOC of the cured part, and maximum temperature rise during the curing process. Each response is fitted versus these 24 factors. The absolute size of effects, P-values, effects plot, normal plot, and results from stepwise selection have been inspected to screen out the unimportant ones. Particularly, 10 factors appear to affect the depth resolution, in which case a resolution III 1/64 fractional factorial experiment (2_{III}^{10-6}) is conducted for further screening; 12 factors could affect the maximum temperature rise, for which a

resolution III 1/256 fractional factorial design (2_{III}^{12-8}) is employed for further screening.

Table 21 lists for each response the parameters that are identified as significant from the final screening experiment.

Table 21 Significant Factors Identified from Screening Experiment

Responses Factors	width resolution	depth resolution	speed (width)	max DOC	max T rise
beam radius (wo)	X		X		
monomer diffusion coefficient (Dm)	X	X	X	X	
monomer glass transition temperature (Tgm)	X			X	
monomer molecular weight (MWm)			X	X	X
initiator loading wt% (wt)		X			
initiator molecular weight (MWs)		X			
initiator absorptivity (ebx)		X			
quantum efficiency of initiation (phi)		X			
heat of polymerization (deltH)					X
laser scanning speed (Vs)					X
monomer heat capacity (CpM)					X

The interactions among significant factors are investigated in follow-up 2^3 full factorial experiments for each of the responses: width resolution, speed in width direction, and maximum DOC, and a follow-up 2^4 full factorial design for maximum temperature rise. A resolution V half-fraction 2^{5-1} factorial design is used to study the factor effects for depth resolution. No parameter seems significant for the speed evaluated in depth direction, as shown in Table 21.

7.1.1 Sensitive Parameters for Width Resolution

Table 22 shows the full factorial design for the three parameters that have been identified as important for width resolution. The response is evaluated and recorded for each run. The other 21 parameters are fixed at values of the original process model (as used in Chapter 6 for single-line part building).

Table 22 Full Factorial Design and Response Values (Width Resolution)

Run	Beam radius (wo)	Monomer diffusion coefficient (Dm)	Monomer glass transition temperature (Tgm)	Width Resolution (μm)
1	-1	-1	-1	250
2	1	-1	-1	494
3	-1	1	-1	270
4	1	1	-1	500
5	-1	-1	1	462
6	1	-1	1	890
7	-1	1	1	480
8	1	1	1	892

The initial inspection of the absolute size of the effects (Table 23) and normal plot (Figure 47) demonstrate that the active effects are the main effects for laser beam radius and monomer glass transition temperature, and the interaction effect between them. This is confirmed by a formal test Lenth's method (Wu and Hamada, 2002) which provides quantitative evidence for effect significance (Table 23): these three effects can be declared significant at the 0.001 level or even smaller, i.e., with at least 99.9% confidence. Besides, the monomer diffusion coefficient can be claimed important with almost 90% confidence.

Table 23 Estimated Factorial Effects and Lenth's Test for Width Resolution

Term	Effect	Coef	abs(tp _{SE,i})	P-value
Constant		529.75		
Beam radius (wo)	328.5	164.25	48.67	<0.001
Monomer diffusion coefficient (Dm)	11.5	5.75	1.70	0.101
Monomer glass transition temperature (Tgm)	302.5	151.25	44.81	<0.001
wo*Dm	-7.5	-3.75	1.11	0.233
wo*Tgm	91.5	45.75	13.56	<0.001
Dm*Tgm	-1.5	-0.75	0.22	>0.4
wo*Dm*Tgm	-0.5	-0.25	0.07	>>0.4

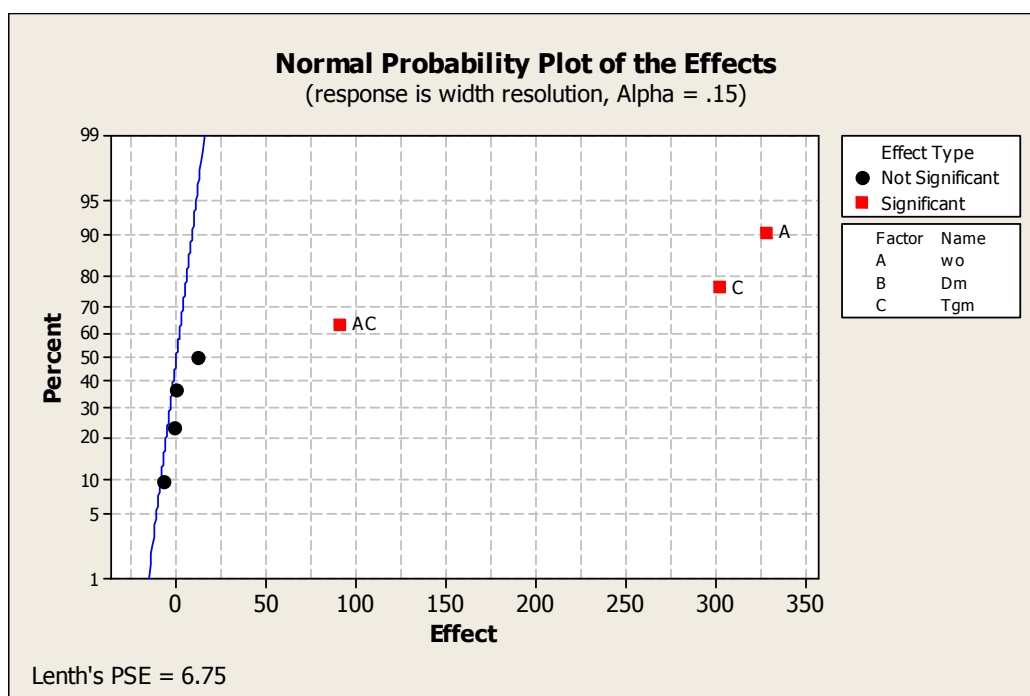
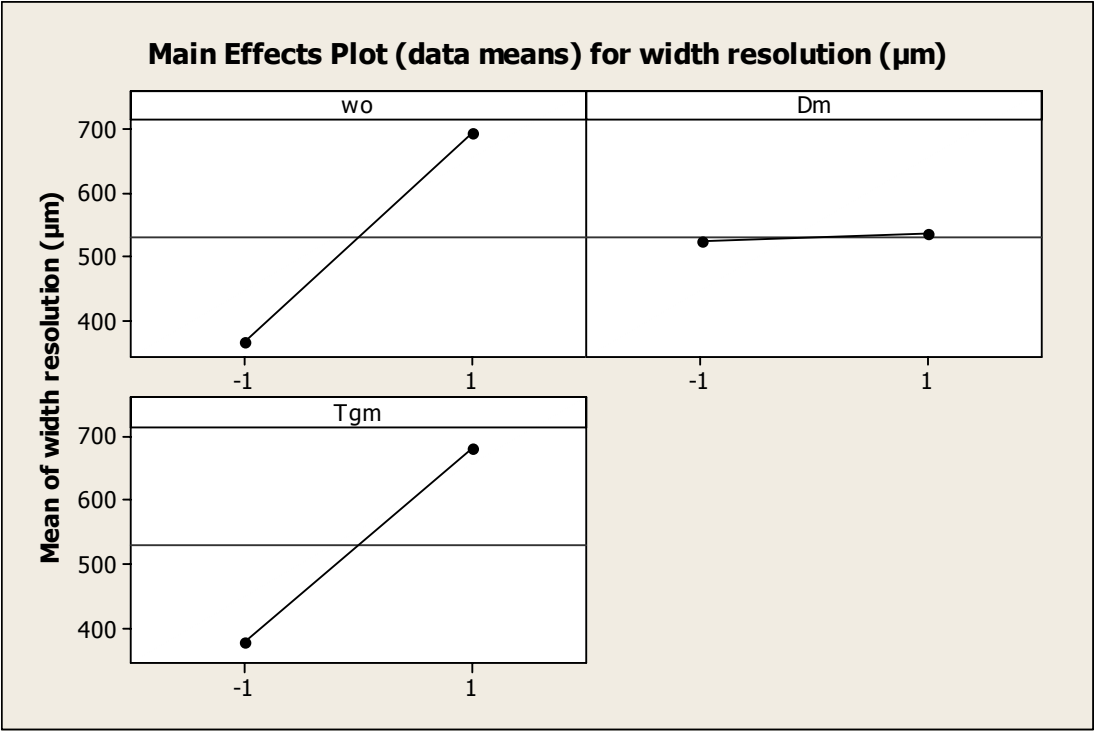


Figure 47 Normal Plot for Width Resolution

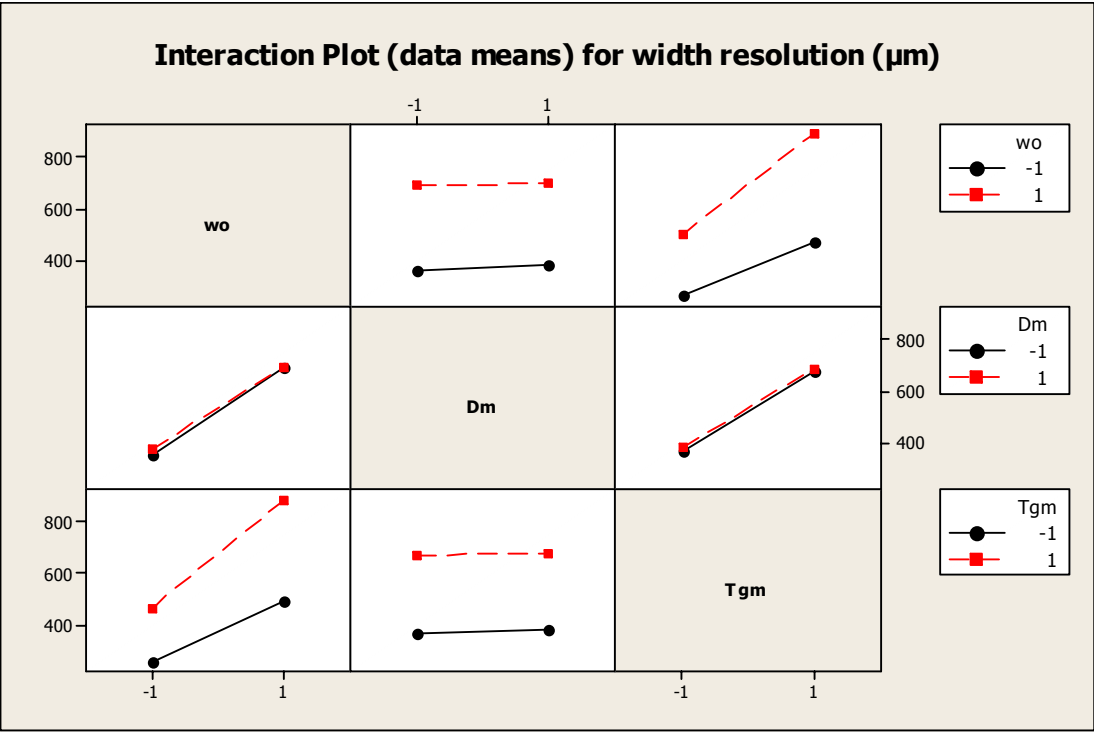
The regression model is then reduced to retain only the effects that are identified as active. As shown in Appendix D, the fit of the reduced model appears to be good and it has great predictive ability ($R^2_{\text{pred}} = 99.63\%$). The statistical significance of the two main effects and one interaction is confirmed as well: almost no risk is taken when claiming these three effects are significant (P-value = 0 for all three effects).

The stepwise selection result also demonstrates the importance of these three effects. Furthermore, it also indicates the less importance of two additional effects: main effect for monomer diffusion coefficient and interaction between beam radius and monomer diffusion coefficient (Appendix E). This is demonstrated by Lenth's test results (Table 23) as well: the confidence to claim them significant is about 10% and 20%, respectively.

The effect significance of the parameters can also be observed from the main effects and interaction plots (Figure 48). From the main effects plot, it appears that monomer diffusion coefficient doesn't have a noticeable effect on the width resolution, while with beam radius or monomer T_g increasing, the width resolution decreases (part width increases) significantly. It makes sense that the cured part gets wider when the incident beam gets wider. An increase in monomer T_g reduces the free volume of the curing system. Suppose the critical free volume for propagation and termination are constant, then a decrease in free volume decreases the termination effect relative to propagation. Thus, a bigger part is built. Further investigation later demonstrates that effect of monomer T_g on the width resolution is not a simple linear relationship.



(a) Main Effects Plot



(b) Two-Factor Interaction Plot

Figure 48 Factorial Effects Plot for Width Resolution: (a) main effect (b) interaction

From the interaction plot, it can be seen that at high or low level of beam radius, there is little effect of monomer diffusion coefficient on the width resolution, which leads to unimportant interaction between these two factors as well. This relation is also illustrated by the Dm-against-wo plot in which the two joined lines are almost overlapped with each other. Furthermore, the large vertical distance of the overlapped lines in Dm-against-wo plot and correspondingly the large space between two separate lines in wo-against-Dm plot reflect an active effect of beam radius on the width resolution. Both wo-against-Tgm and Tgm-against-wo plot are synergistic, which indicates a simple relation: whether beam radius (and respectively, monomer Tg) is high or low, the width resolution decreases with monomer Tg (and respectively, beam radius) increasing. On the other hand, the degree to which the width resolution decreases when beam radius (and monomer Tg, respectively) increases depends on high or low monomer Tg (and beam radius, respectively) being adopted. Beam radius (and respectively, monomer Tg) affects the width resolution more significantly at high monomer Tg (and respectively, high beam radius) than at low monomer Tg (and respectively, low beam radius). The relation between monomer diffusion coefficient and monomer Tg won't be detailed here since it is similar to the relation between monomer diffusion coefficient and beam radius.

In summary, laser beam radius and monomer glass transition temperature are two sensitive parameters that affect the width resolution significantly. The width resolution decreases (part width increases) with either of these two factors increasing. The sensitivity of beam radius (and respectively, monomer Tg) depends on the level of monomer Tg (and respectively, beam radius). The beam radius (or monomer Tg) is more sensitive at high monomer Tg (or high beam radius).

7.1.2 Sensitive Parameters for Speed (Width Direction)

Similarly, a 2^3 full factorial design is employed for speed defined in width direction to investigate the interaction among beam radius, monomer diffusion coefficient, and monomer molecular weight. The speed is characterized by the time taken to cure a 200 μm wide single line part.

The inspection of effects size, normal plot, and effects plot as well as the results of Lenth's test, stepwise selection, and reduced model regression reaches a consistent agreement on active effects. The active effects are identified to be main effects for beam radius and monomer molecular weight and interaction between them. Table 24 shows the Lenth's test results, from which we can see that these three effects can be declared significant with 99.5% confidence.

Table 24 Estimated Factorial Effects and Lenth's Test for Speed (Width)

Term	Effect	Coef	$\text{abs}(t_{\text{PSE},i})$	P-value
Constant		0.3994		
Beam radius (w_0)	-0.7276	-0.3638	97.01	$<<0.001$
Monomer diffusion coefficient (D_m)	0.0061	0.0031	0.81	0.361
Monomer molecular weight (MW_m)	0.0504	0.0252	6.72	0.005
$w_0 * D_m$	-0.0064	-0.0032	0.85	0.340
$w_0 * MW_m$	-0.0511	-0.0256	6.81	0.005
$D_m * MW_m$	0.0036	0.0018	0.48	>0.4
$w_0 * D_m * MW_m$	-0.0039	-0.0019	0.52	>0.4

Although the size and sign of the regression coefficients can reveal some information on how the sensitive parameters affect the response, the effects plot provides more information regarding to interactions between parameters in a graphical view. The main effects plot below clearly demonstrates the speed increases significantly when beam

radius increases and increases slightly when monomer molecular weight decreases. Little time is needed when the beam size is large. Further investigation later (Section 7.2.3) demonstrates that the effect of beam radius on curing speed is quite nonlinear. The decrease in monomer molecular weight leads to the increase in monomer molar concentration, and thus the increase in curing speed.

From the interactions plot, beam radius is found to be a more sensitive parameter than monomer molecular weight for width speed. The effect of beam radius is slightly more significant at higher monomer molecular weight than at lower molecular weight. On the other hand, monomer molecular weight seems more important at low beam radius than at high beam radius.

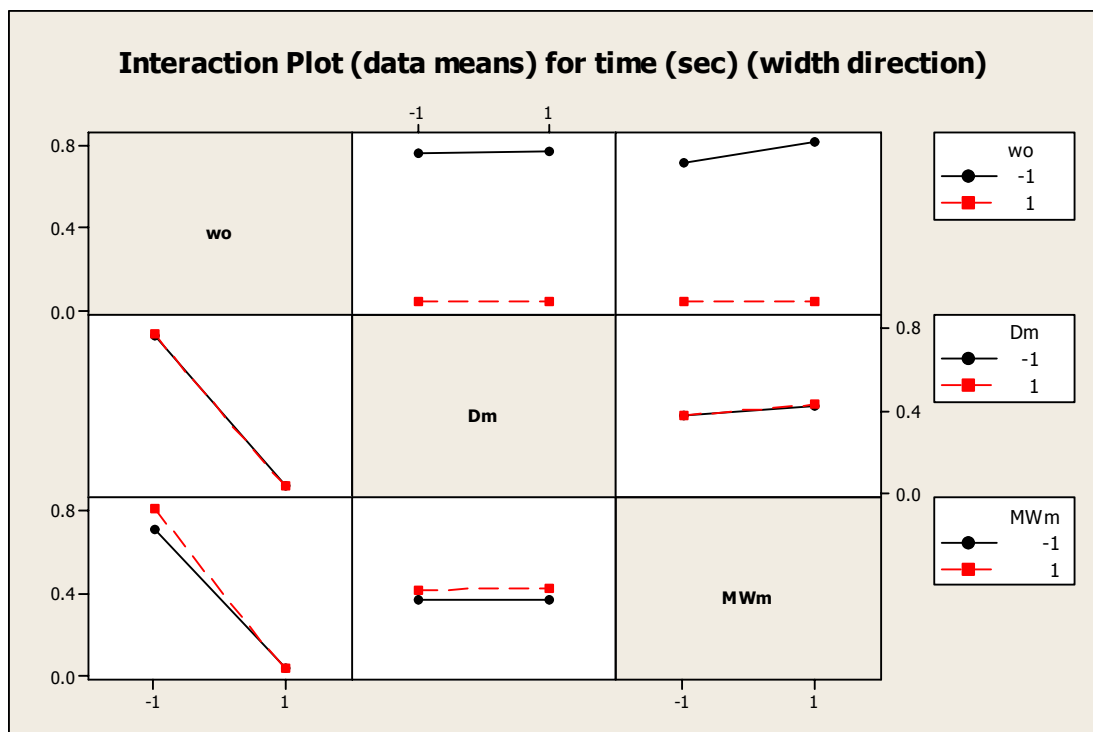
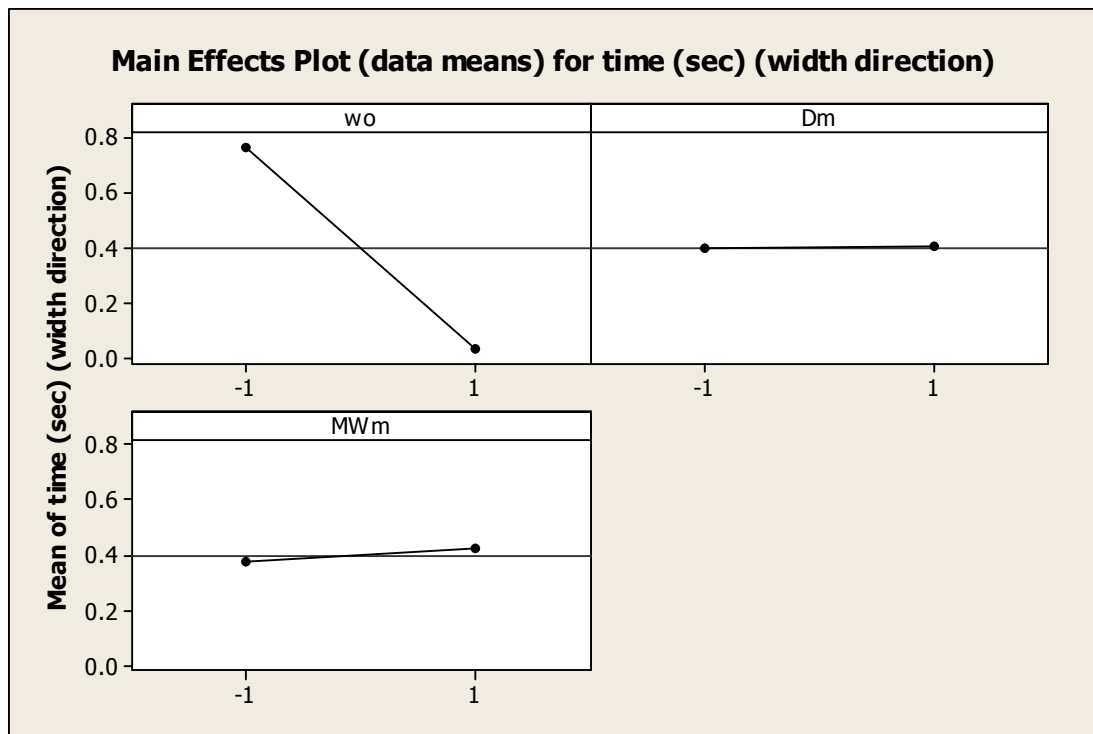


Figure 49 Factorial Effects Plot for Speed (Width): (a) main effect (b) interaction

7.1.3 Sensitive Parameters for DOC

Similarly, a 2^3 design full factorial experiment has been conducted for maximum DOC to investigate the interaction among monomer diffusion coefficient, monomer molecular weight, and monomer glass transition temperature.

The active effects are identified to be main effects for all three parameters mentioned above as well as interaction between monomer molecular weight and monomer Tg. The Lenth's test (Table 25) shows the main effects for monomer Tg and molecular weight and interaction between them can be declared significant with at least 99.9% confidence, while the main effect for monomer diffusion coefficient is identified as active with 95.2% confidence. Both Lenth's test and stepwise selection also show that the interaction effect between monomer diffusion coefficient and monomer Tg could be important as well.

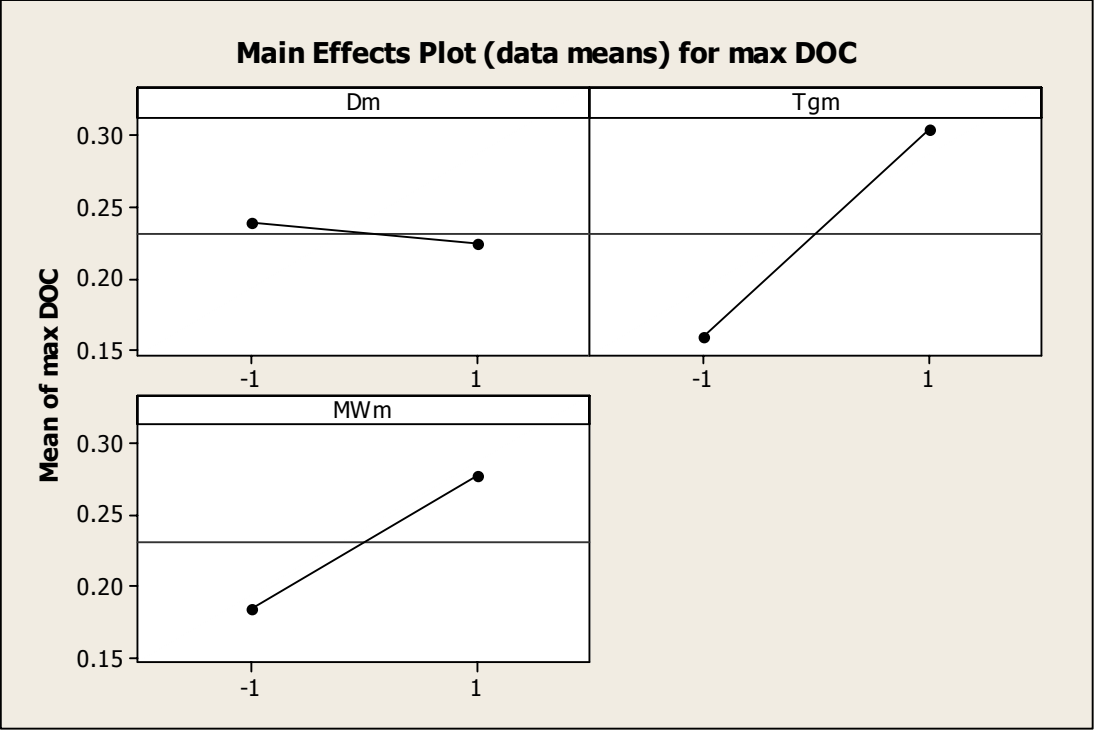
Table 25 Estimated Factorial Effects and Lenth's Test for Maximum DOC

Term	Effect	Coef	abs(tp _{SE,i})	P-value
Constant		0.23125		
Monomer diffusion coefficient (Dm)	-0.015	-0.0075	2.35	0.048
Monomer glass transition temperature (Tgm)	0.1455	0.07275	22.82	<0.001
Monomer molecular weight (MWm)	0.093	0.0465	14.59	<0.001
Dm*Tgm	0.008	0.004	1.25	0.189
Dm*MWm	-0.0005	-0.00025	0.078	>>0.4
Tgm*MWm	0.094	0.047	14.75	<0.001
Dm*Tgm*MWm	0.0005	0.00025	0.078	>>0.4

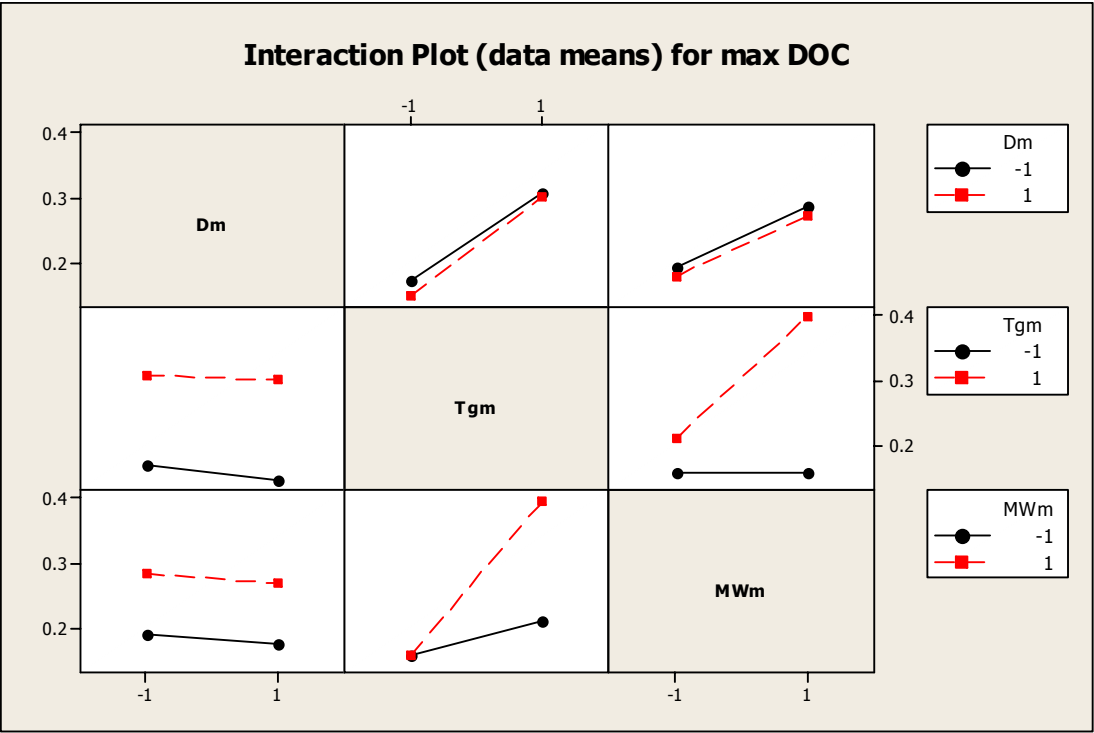
The main effects plot below demonstrates that the DOC of the part increases with monomer Tg or molecular weight increasing. As mentioned earlier, an increase in monomer Tg decreases termination effect, thus increases DOC. High monomer molecular weight (Low monomer concentration) decreases the curing speed, but could eventually contribute to DOC considering diffusion limitation. Further investigation later shows a

slight curvature in monomer molecular weight and significant nonlinear behavior in monomer Tg. High monomer diffusion increases monomer composition at the centerline of the part, and leads to a slight decrease in DOC.

As shown in interaction plot above, the interaction between monomer Tg and monomer molecular weight appears significant. Furthermore, molecular weight is much more sensitive at high than at low monomer Tg, which again demonstrates characteristics of diffusion-limited reaction. Similarly, monomer Tg is more sensitive at high than at low monomer molecular weight.



(a) Main Effects Plot



(b) Two-Factor Interaction Plot

Figure 50 Factorial Effects Plot for Max DOC: (a) main effect (b) interaction

7.1.4 Sensitive Parameters for Temperature Rise

A full factorial (2^4) design is adopted to investigate interactions between the four parameters that are identified as important for temperature rise in the resin vat.

The Lenth's test (Table 26) shows heat of polymerization and monomer molecular weight are sensitive parameters. Main effects for these two factors and their interaction effect can be declared important at a risk of <10%. The normal plot also illustrates these three effects are significant. The main effect for scanning speed is claimed to be active with >85% confidence. The significance of these four effects has been confirmed by the regression of the reduced model (only four effects are included in the model) which turns out to have a good fit quality. The stepwise regression selects nine additional factorial effects such as main effect for monomer heat capacity, interactions between scanning speed and monomer molecular weight, etc. These additional effects are identified by Lenth's method as less likely to be important (about 70% or even less).

Table 26 Estimated Effects and Lenth's Test for Maximum Temperature Rise

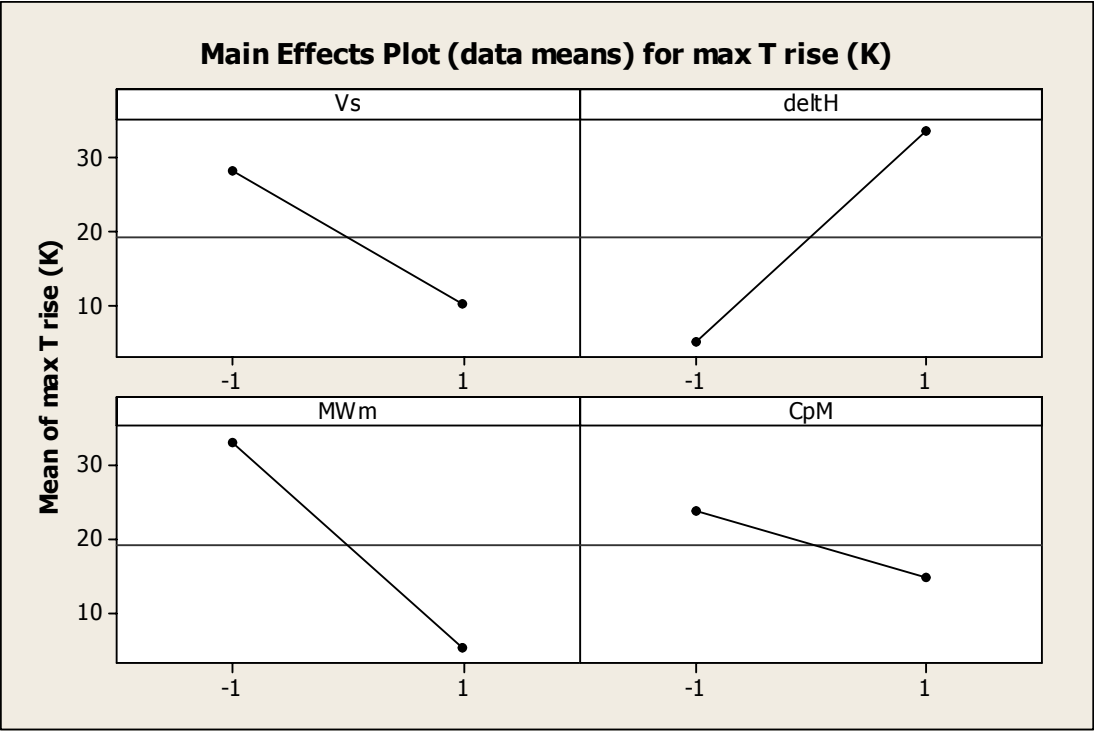
Term	Effect	Coef	abs($t_{PSE,i}$)	P-value
Constant		19.2		
Laser scanning speed (Vs)	-18.12	-9.06	1.53	0.138
Heat of polymerization (ΔH)	28.59	14.3	2.41	0.035
Monomer molecular weight (MWm)	-27.77	-13.89	2.34	0.039
Monomer heat capacity (CpM)	-8.95	-4.48	0.75	0.418
Vs* ΔH	-12.6	-6.3	1.06	0.27
Vs*MWm	12.12	6.06	1.02	0.29
Vs*CpM	2.01	1.01	0.17	>0.4
ΔH *MWm	-20.26	-10.13	1.71	0.099
ΔH *CpM	-5.83	-2.91	0.49	>0.4
MWm*CpM	5.58	2.79	0.47	>0.4
Vs* ΔH *MWm	7.91	3.95	0.67	>0.4
Vs* ΔH *CpM	0.34	0.17	0.029	>>0.4
Vs*MWm*CpM	-0.22	-0.11	0.019	>>0.4
ΔH *MWm*CpM	3.18	1.59	0.27	>0.4
Vs* ΔH *MWm*CpM	1.07	0.54	0.09	>>0.4

The effects plot (Figure 51) demonstrates how the significant parameters affect the temperature rise.

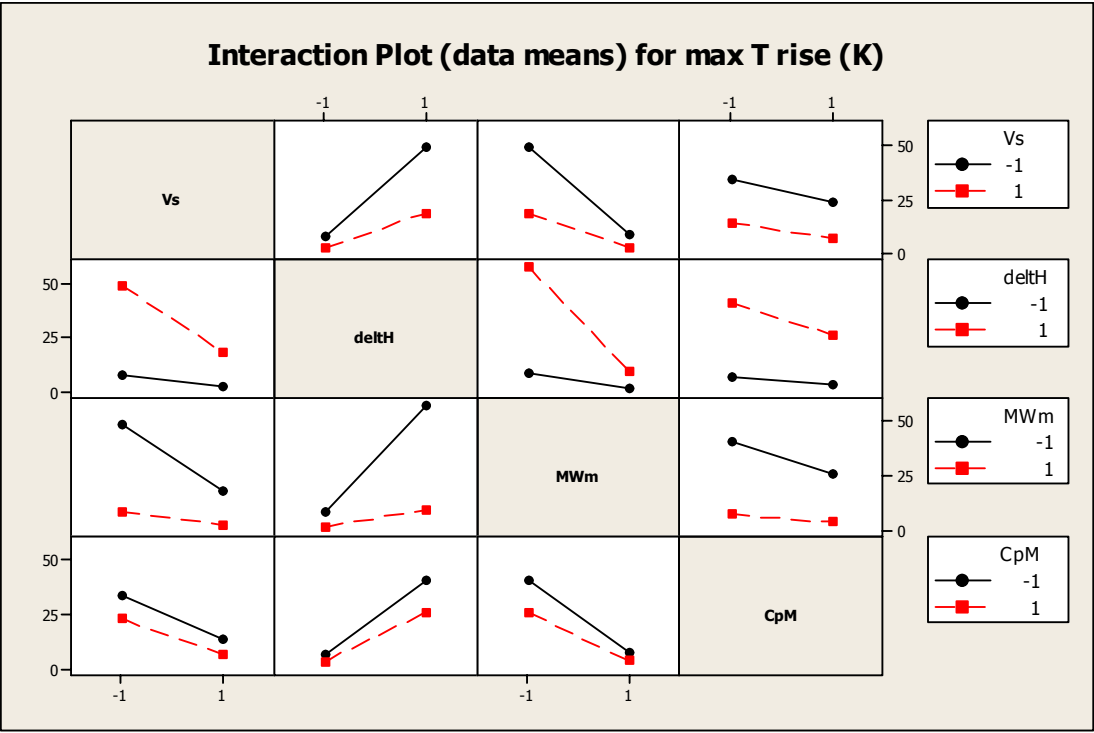
An increase in heat of polymerization (“ ΔH ”) leads to more heat generated for the same amount of reaction and thus larger temperature rise in the resin, as shown in the main effects plot in Figure 51. The temperature rise decreases as laser scanning speed (“ V_s ”), monomer molecular weight (“ MW_m ”), or monomer heat capacity (“ C_{pM} ”) increases. This makes physical sense since higher laser moving speed deposits less energy to the resin, and higher monomer molecular weight causes lower monomer concentration. Both of them lead to less amount of reaction and thus generate less heat. For the same amount of heat generated, higher monomer heat capacity leads to smaller temperature rise. The effect of monomer heat capacity is less significant as observed.

The interactions plot shows that the temperature rise is more sensitive to the heat of polymerization at low monomer molecular weight. Monomer molecular weight is a more sensitive parameter at high heat of polymerization.

Other interaction effects shown in Figure 51 (b) are less significant and not discussed here.



(a) Main Effects Plot



(b) Two-Factor Interaction Plot

Figure 51 Factorial Effects Plot for Temperature Rise: (a) main effect (b) interaction

7.1.5 Sensitive Parameters for Depth Resolution

A resolution V five-factor half-fraction (2^{5-1}) factorial design is adopted to investigate interactions between the five parameters that are identified as important. For a design of this resolution, all main effects are clear of other main effects and two-factor as well as three-factor interactions, and confounded with four-factor interactions. All two-factor interactions are clear of other two-factor interactions, and aliased with three-factor interactions. Ignoring high order interactions, all main effects and two-factor interactions can be clearly evaluated.

Table 27 Estimated Effects and Lenth's Test for Depth Resolution

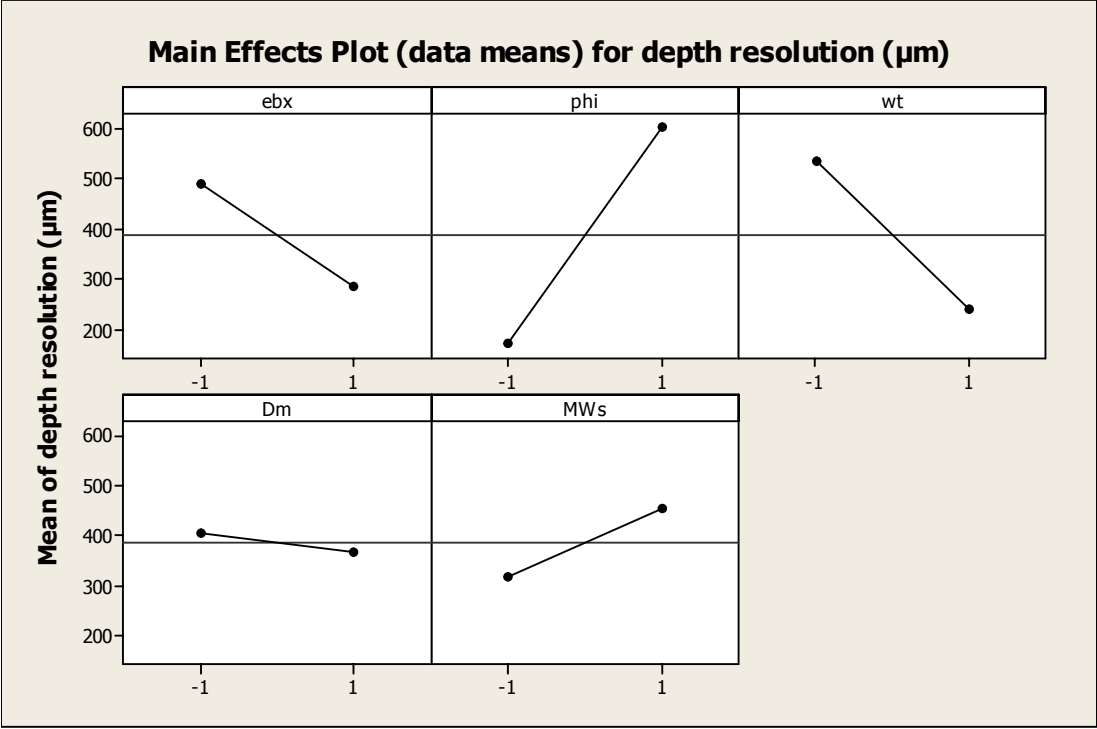
Term	Effect	Coef	abs(tp _{SE,i})	P-value
Constant		386		
Initiator absorptivity (ebx)	-204.2	-102.1	1.32	0.184
Quantum efficiency of initiation (phi)	434.5	217.2	2.81	0.023
Initiator wt% (wt)	-297.7	-148.9	1.93	0.070
Monomer diffusion coefficient (Dm)	-36.8	-18.4	0.24	>0.4
Initiator molecular weight (MWs)	136.3	68.1	0.88	0.354
ebx*phi	-179.3	-89.6	1.16	0.234
ebx*wt	41	20.5	0.27	>0.4
ebx*Dm	-108	-54	0.70	0.445
ebx*MWs	-10	-5	0.065	>>0.4
phi*wt	-303.2	-151.6	1.96	0.067
phi*Dm	-37.8	-18.9	0.25	>0.4
phi*MWs	186.8	93.4	1.21	0.216
wt*Dm	-7	-3.5	0.045	>>0.4
wt*MWs	3.5	1.8	0.023	>>0.4
Dm*MWs	98	49	0.63	0.478

As shown in Table 27, the Lenth's test illustrates that the quantum efficiency of initiation and initiator loading are sensitive parameters. Main effects for these two factors and their interaction effect can be declared important at a risk of less than 10%. The normal plot also illustrates these three effects are significant. The stepwise selection

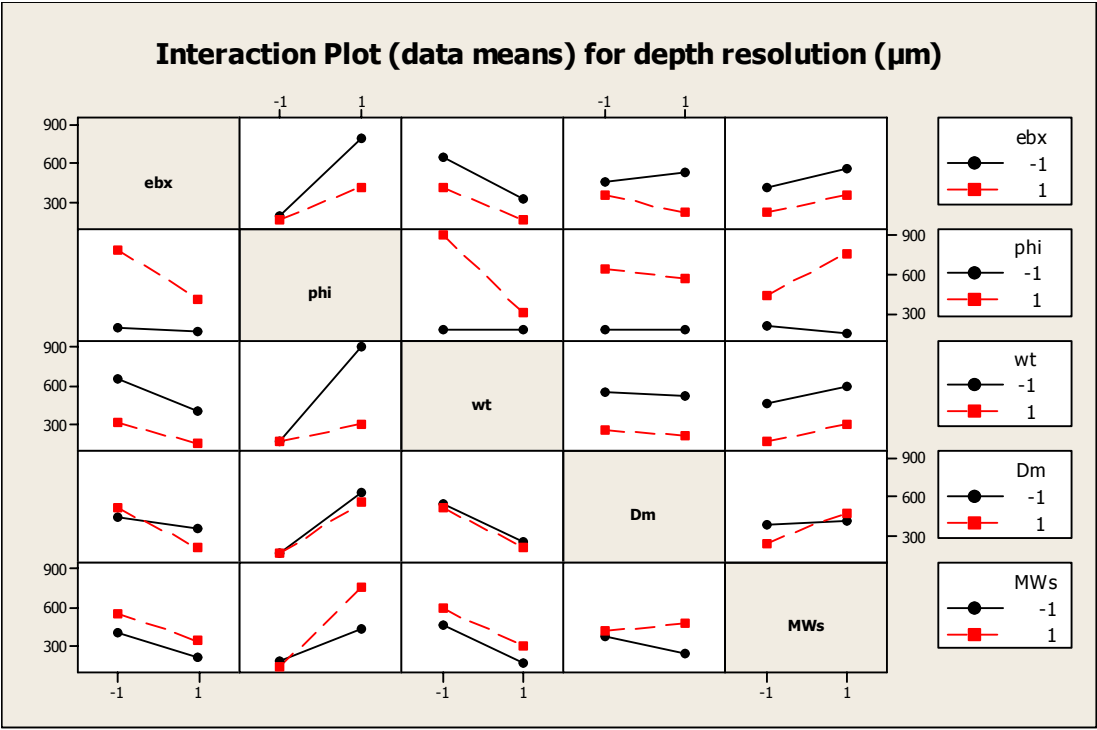
demonstrates six additional important factorial effects such as main effects for initiator absorptivity and initiator molecular weight and interactions between quantum efficiency and initiator molecular weight, etc. These additional effects are identified by Lenth's method as less likely to be important (about 80% or even less, see items in red and not bold in Table 27).

Either an increase in initiator wt% loading ("wt") or initiator absorption coefficient ("ebx") leads to a smaller beam penetration depth and thus an increase in depth resolution, as shown in Figure 52 (a). Higher quantum efficiency of initiation ("phi") generates more radicals to grow a bigger part. The effects of monomer diffusion coefficient ("Dm") and initiator molecular weight ("MWs") are much less significant.

The interactions plot in Figure 52 (b) shows that quantum efficiency ("phi") plays a bigger role at low absorption coefficient ("ebx") and low initiator loading, while absorption coefficient and initiator loading are more sensitive at high quantum efficiency. The interaction between "ebx" (or "MWs") and "Dm" is antagonistic. At low absorption coefficient (or high initiator molecular weight), the cure depth increases slightly with monomer diffusion increasing. This reveals another side of monomer diffusion effect: faster diffusion facilitates the movement and reaction of the species thus to form a bigger part. The phi-against-MWs plot is antagonistic as well. At low quantum efficiency, the cure depth decreases when the initiator molecular weight increases (beam penetration depth increases). This indicates that an increase in penetration depth does not necessarily lead to an increase in the cure depth. There might not be enough radicals (in this case, quantum efficiency is low) to cure the part tip enough. Other interaction effects shown in Figure 52 (b) are minor and are not discussed here.



(a) Main Effects Plot



(b) Two-Factor Interaction Plot

Figure 52 Factorial Effects Plot for Depth Resolution: (a) main effect (b) interaction

Table 21 from the screening experiment is revised according to the follow-up effect significance investigation above for each response. In Table 28, “XX” denotes more significant parameters, while “X” denotes relatively less important ones.

Table 28 Significant Factors for Investigated Responses

Factors \ Responses	width resolution	depth resolution	speed (width)	max DOC	max T rise
beam radius (wo)	XX		XX		
monomer diffusion coefficient (Dm)	X			XX	
monomer glass transition temperature (Tgm)	XX			XX	
monomer molecular weight (MWm)			XX	XX	XX
initiator loading wt% (wt)		XX			
initiator molecular weight (MWs)		X			
initiator absorptivity (ebx)		X			
quantum efficiency of initiation (phi)		XX			
heat of polymerization (deltH)					XX
laser scanning speed (Vs)					X
monomer heat capacity (CpM)					

7.2 Resolution and Speed Prediction by Regression Model

As is well known, SL curing resolution and speed can be influenced by a lot of factors such as material properties, reaction kinetics, and process or laser parameters. To obtain an explicit function of resolution or speed in terms of these properties is almost impossible. A useful assumption is made that the function is bilinear in which the linear terms model the effect of influential factors and bilinear terms model the important interaction effects. In case of the existence of curvature effect, the square of the factor actual value is used to represent the quadratic effect. The response is then fitted versus the involved parameters and combinations. The predictive ability of regression models is verified.

7.2.1 Regression Prediction Model for Depth Resolution

Recall that the active effects for depth resolution are main effects for quantum efficiency of initiation and initiator wt% loading and their interaction effect. The regression model based on these three effects, however, doesn't have a good fit or good predictive ability. The other important effects identified by stepwise selection are then included into the regression model as well. The regression equation of this revised model as well as its good fit quality and predictive ability is demonstrated in Appendix F.

To verify this regression model, three simulations have been conducted using the SL cure process model. The conditions for the simulations are shown in Table 29, and the results and comparison with regression model predicted results are shown in Table 30. The prediction error of the regression model is found to be within 15 %.

Table 29 Simulation Conditions to Test Predictive Ability of Regression Models

Condition	I	II	III	units
beam radius (wo)	1.10E-04	1.50E-04	2.00E-04	m
monomer diffusion coefficient (Dm)	1.00E-14	1.00E-14	1.00E-14	m ² /s
monomer glass transition temperature (Tgm)	208.74	180	210	K
monomer molecular weight (MWm)	0.53	1	1.5	Kg/mol
initiator loading wt% (wt)	2	1	5	wt%
initiator molecular weight (MWs)	0.26	0.2	0.4	Kg/mol
initiator absorptivity (ebx)	19.87	40	60	m ³ /mol-m
quantum efficiency of initiation (phi)	0.6	0.3	0.1	

Table 30 Depth Resolution Predicted by Regression Model

Condition	I	II	III
simulation results (μm)	810	525	155
predicted results (μm)	872	474	175
prediction error (%)	7.7	-9.8	12.7

7.2.2 Regression Prediction Model for Width Resolution

The prediction error of the fitted bilinear model versus the important effects (main effects for beam radius and monomer Tg and interaction between them) is up to 60%. The addition of the two less active effects (main effect for monomer diffusion coefficient and its interaction with beam radius) makes the residual plot versus the predictor monomer diffusion coefficient appear like a parallel band centered about zero, as it should be, but doesn't improve the model predictive ability significantly. Further investigation reveals the possibility of curvature presence in monomer diffusion coefficient and monomer Tg predictors (Figure 53). A three-factor-mixed-level (two levels for beam radius; three levels for monomer diffusion coefficient and monomer Tg) full factorial design is then adopted in order to capture the curvature effect.

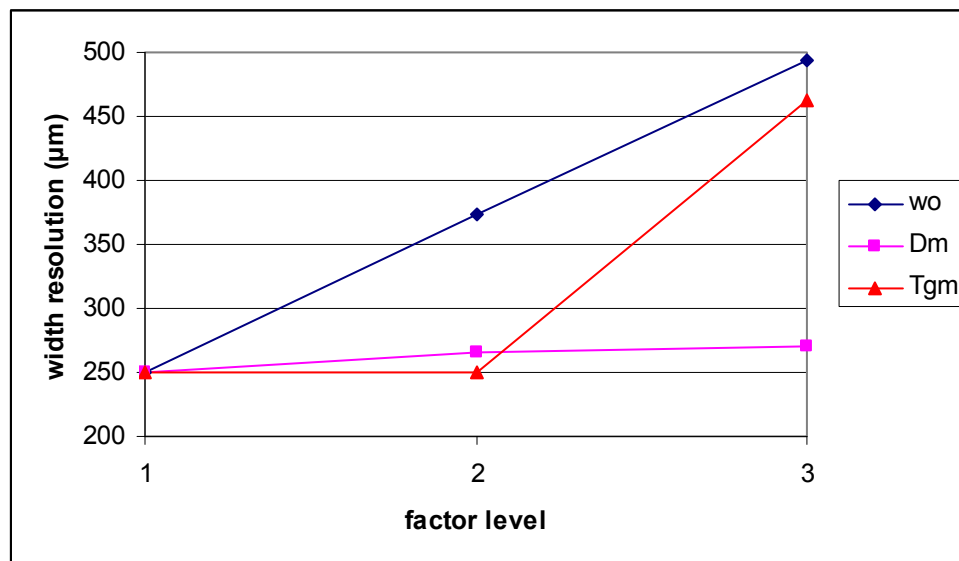
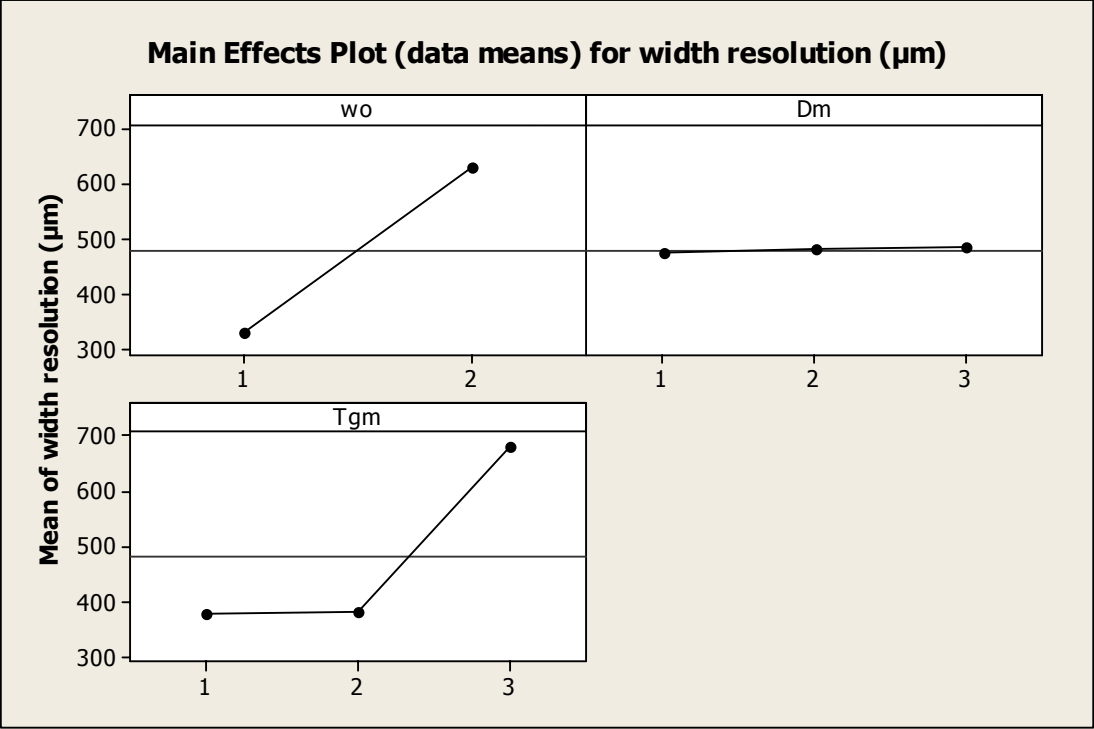
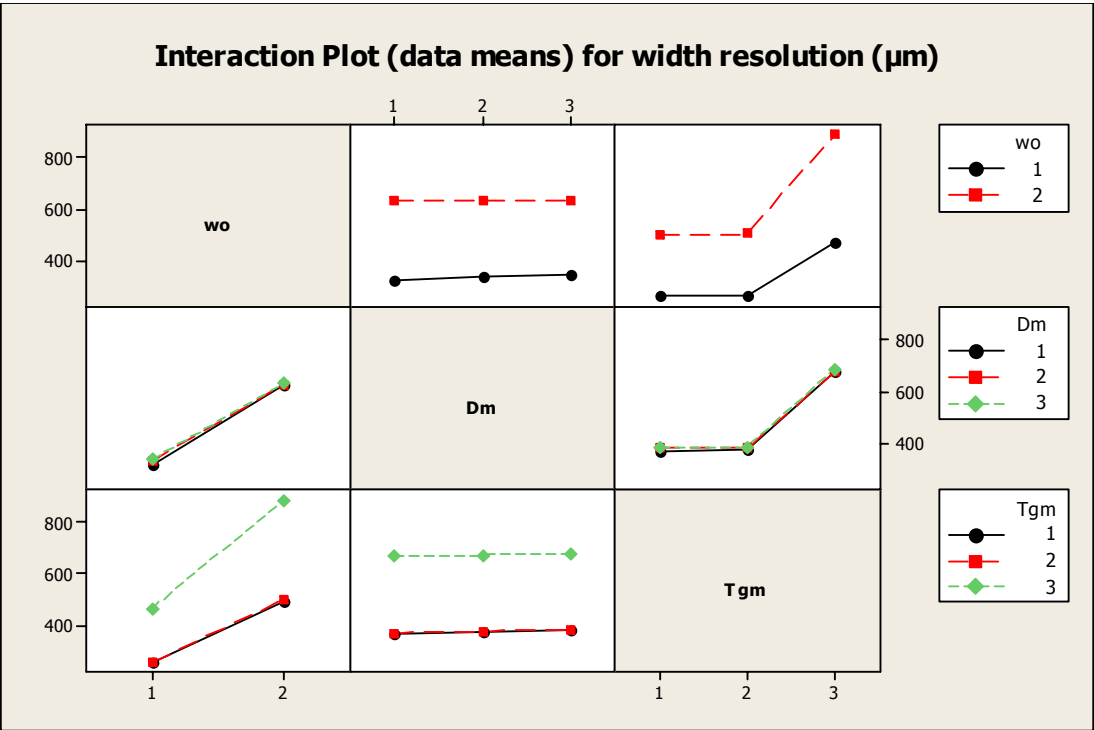


Figure 53 Curvature in Factors for Width Resolution

The effects plot below demonstrates significant linear effect in beam radius, less significant and almost linear effect in monomer diffusion coefficient, and significant curvature effect in monomer glass transition temperature.



(a) Main Effects Plot



(b) Interaction Plot

Figure 54 Curvature Effect for Width Resolution: (a) main effect (b) interaction

As shown in Appendix G, regression analysis has been performed based on stepwise selection results, using Tgm to represent the linear effect of monomer Tg, and Tgm² to represent the quadratic effect of monomer Tg, and wo*Tgm to represent the interaction between beam radius and monomer Tg. The regression model appears to have a good fit and good predictive ability. The verification is shown in Table 31.

Table 31 Width Resolution Predicted by Regression Model

Condition	I	II	III
simulation results (μm)	281	342	488
predicted results (μm)	332	329	613
prediction error (%)	18.3	-4.0	25.6

7.2.3 Regression Prediction Model for Speed (Width Direction)

Curvature has been found in beam radius and in monomer molecular weight (Figure 55) for this response. Further investigation demonstrates that the effect of beam radius on the curing speed is quite nonlinear (Figure 56).

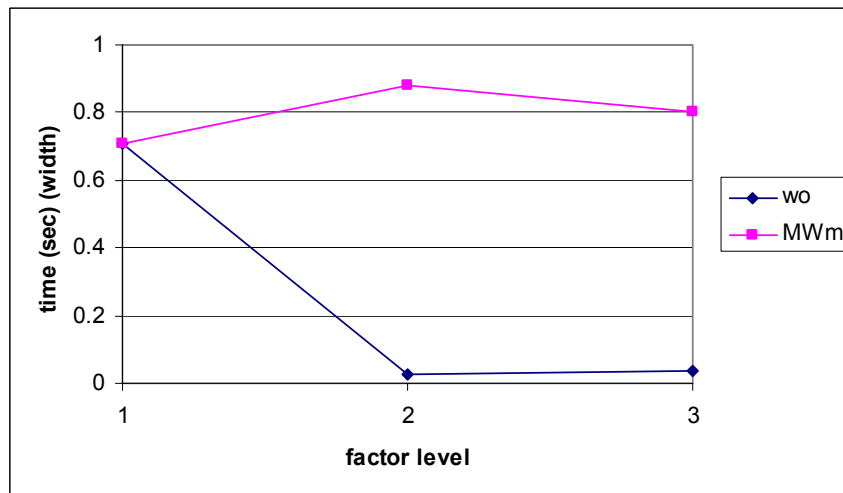


Figure 55 Curvature in Factors for Speed (Width)

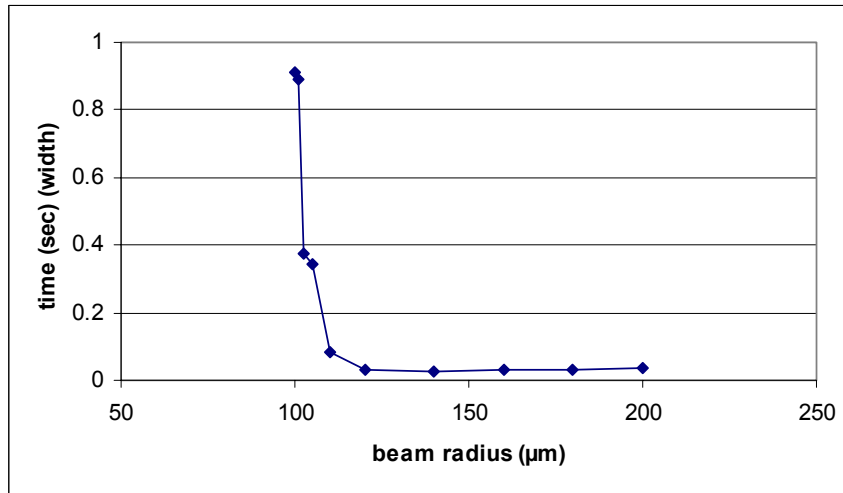
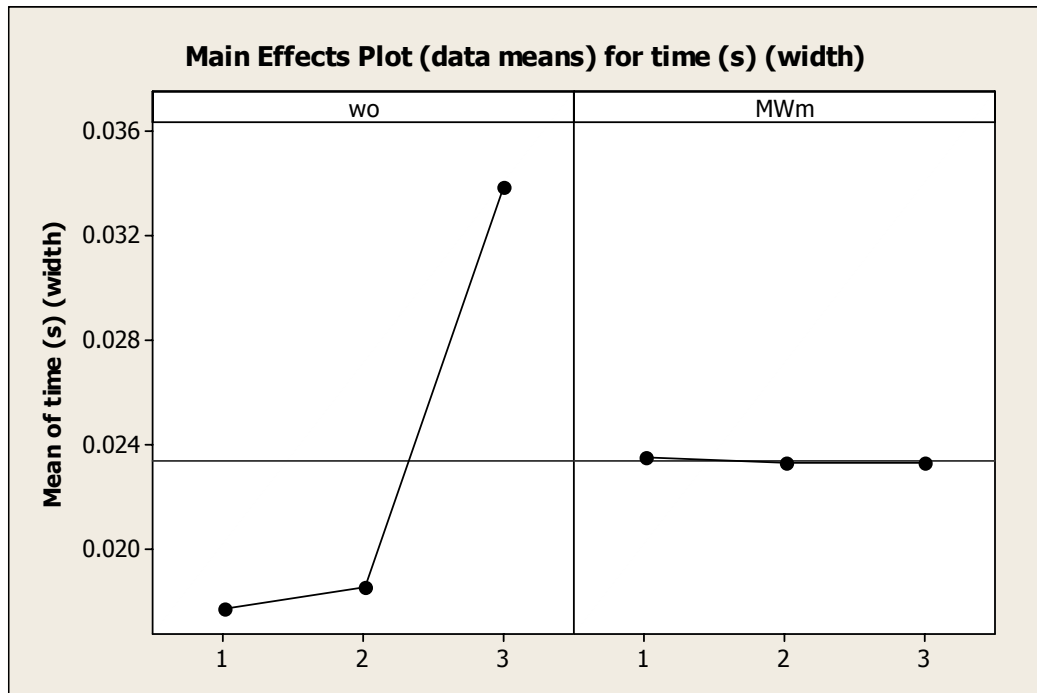


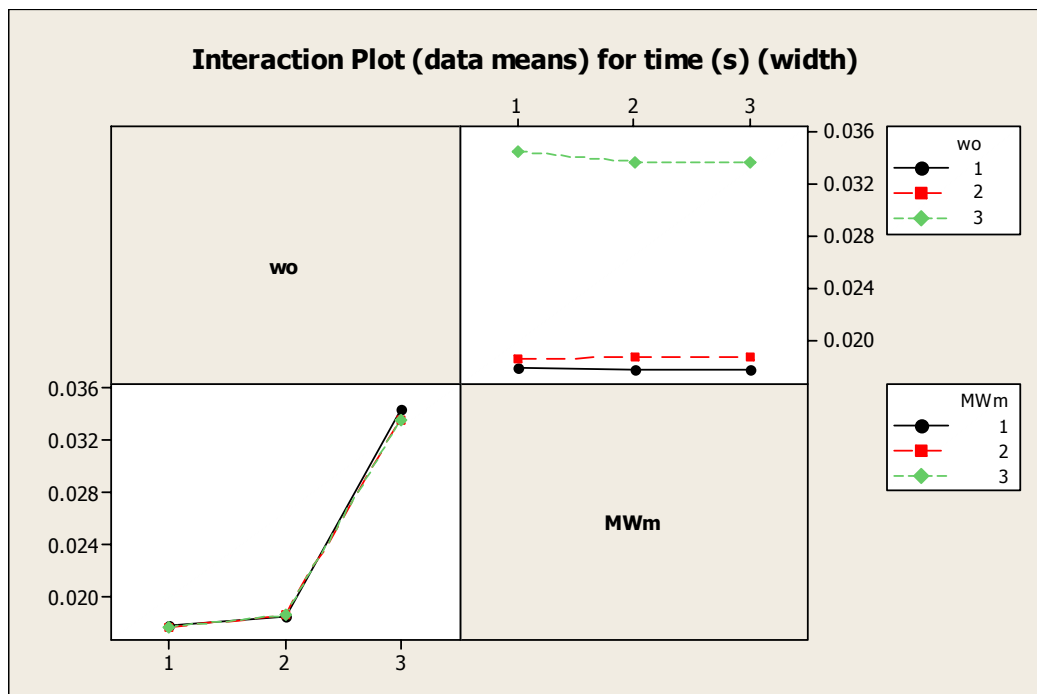
Figure 56 Nonlinear Behavior of Beam Radius for Speed (Width)

The speed increases dramatically when spot size (beam diameter) increases slightly above 200 μm and then almost keeps constant when the spot size increases further. This makes sense recalling the speed is characterized by the time taken to cure 200 μm wide part, 200 μm taken as the low level of spot size, and the laser assumed to be Gaussian. This, however, brings complexity to the regression analysis. It's inappropriate to find a single model to capture all the behavior. To go around this issue, the time consumed to cure 100 μm wide part is used to characterize the curing speed (200 μm wide part is critical here because it overlaps the low level value of spot size). A two-factor-three-level 3^2 design is performed to capture the curvature effect. The effects plot is shown in Figure 57.

As shown in Figure 57, the curing time increases as laser beam radius increases because for the same power and bigger beam size, a lower intensity irradiates the resin inside the 100 μm diameter spot.



(a) Main Effects Plot



(b) Interaction Plot

Figure 57 Factors Curvature for Speed (Width): (a) main effect (b) interaction
(Level “2” value of beam radius = 110 μ m)

A regression analysis has been performed (as shown in Appendix H) based on stepwise selection results. The regression model appears to have a good fit and good predictive ability. The verification is shown in Table 32.

Table 32 Curing Time (Width Direction) Predicted by Regression Model

Condition	I	II	III
simulation results (sec)	0.0185	0.0294	0.0368
predicted results (sec)	0.0185	0.0235	0.0336
prediction error (%)	0	-20.1	-8.7

7.2.4 Regression Prediction Model for Maximum DOC

Similarly, curvature has been found in monomer glass transition temperature and slightly in monomer molecular weight (Figure 58). A three-factor-three-level 3^3 design has been performed to detect and capture the curvature effect. The effects plot is shown in Figure 59.

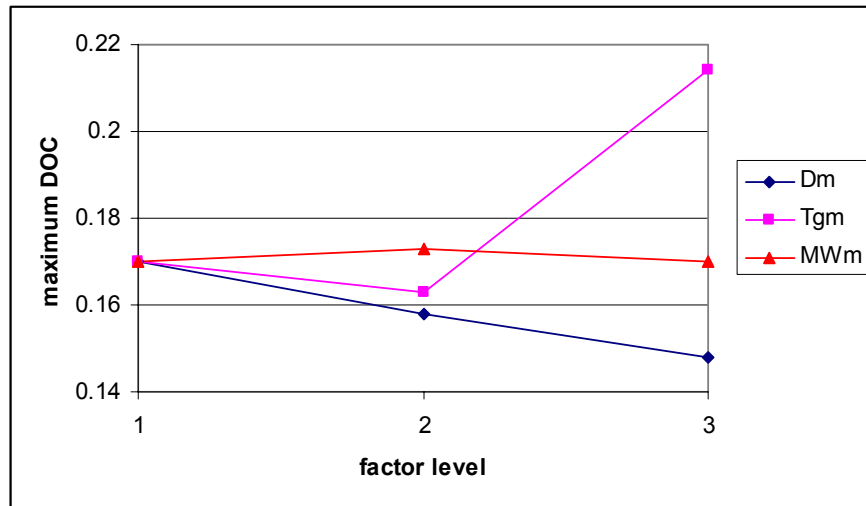
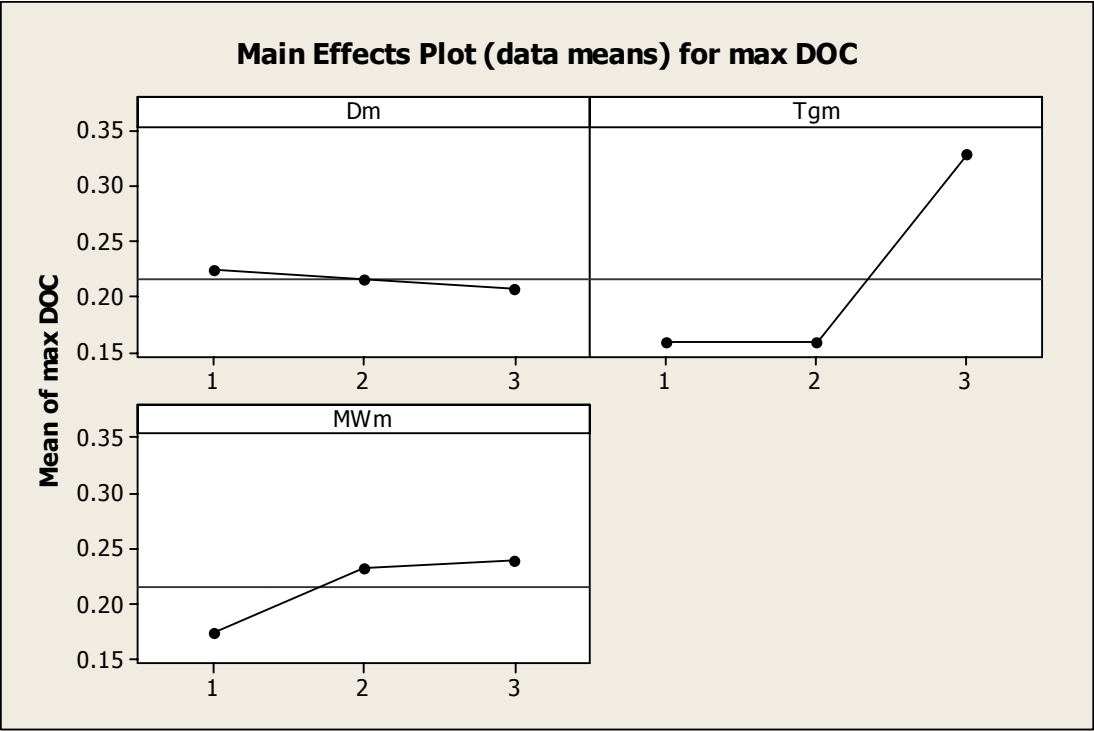
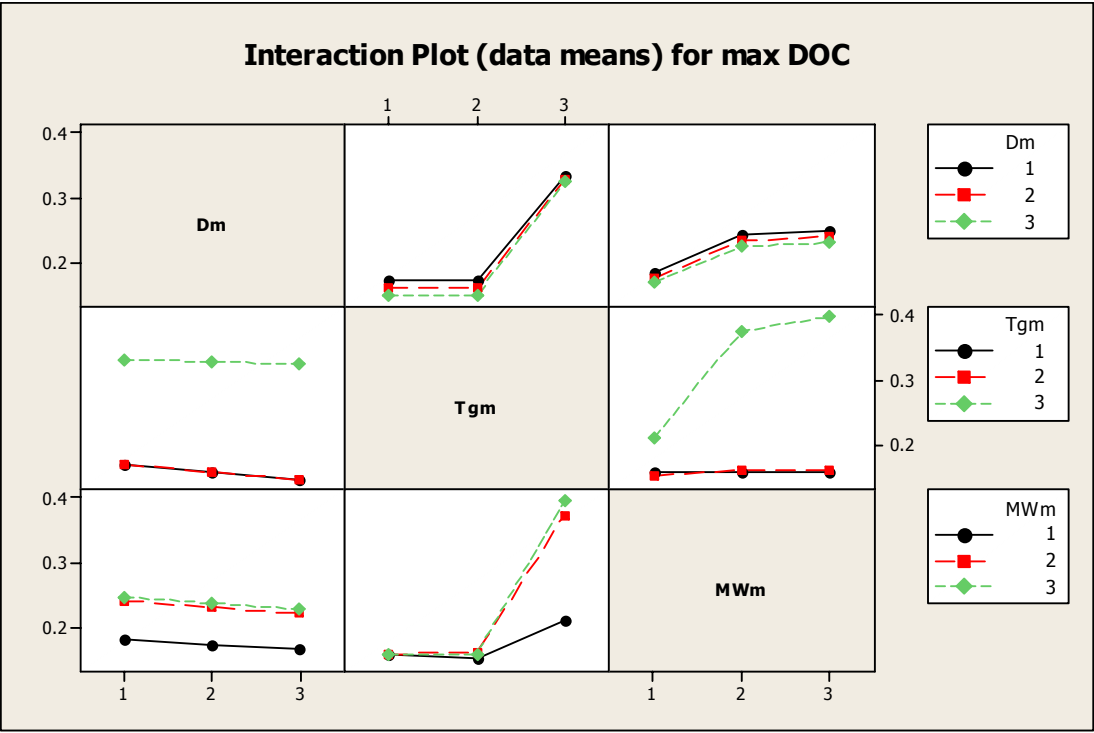


Figure 58 Curvature in Factors for Maximum DOC



(a) Main Effects Plot



(b) Interaction Plot

Figure 59 Factors Curvature for Maximum DOC (a) main effect (b) interaction

As shown in Appendix I, regression analysis has been performed based on stepwise selection results. The regression model appears to have a good fit and good predictive ability. The verification is shown in Table 33.

Table 33 Maximum DOC Predicted by Regression Model

Condition	I	II	III
simulation results	0.247	0.137	0.193
predicted results	0.180	0.125	0.198
prediction error (%)	-27.1	-8.8	2.6

7.2.5 Regression Prediction Model for Maximum Temperature Rise

Curvature has been found more significant in monomer molecular weight, laser scanning speed, and heat of polymerization, and negligible in monomer heat capacity (Figure 60). A three-factor-three-level 3^3 design has been conducted to detect and capture the curvature effect. The effects plot is shown in Figure 61.

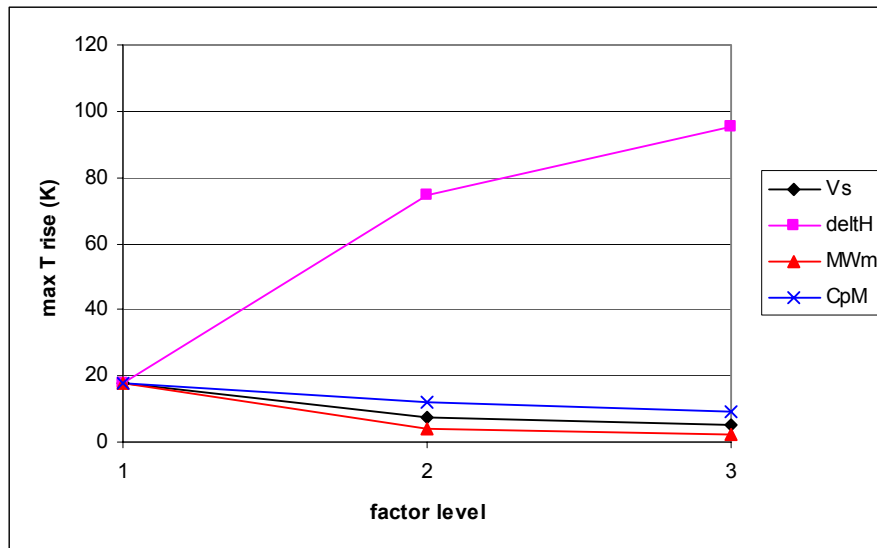
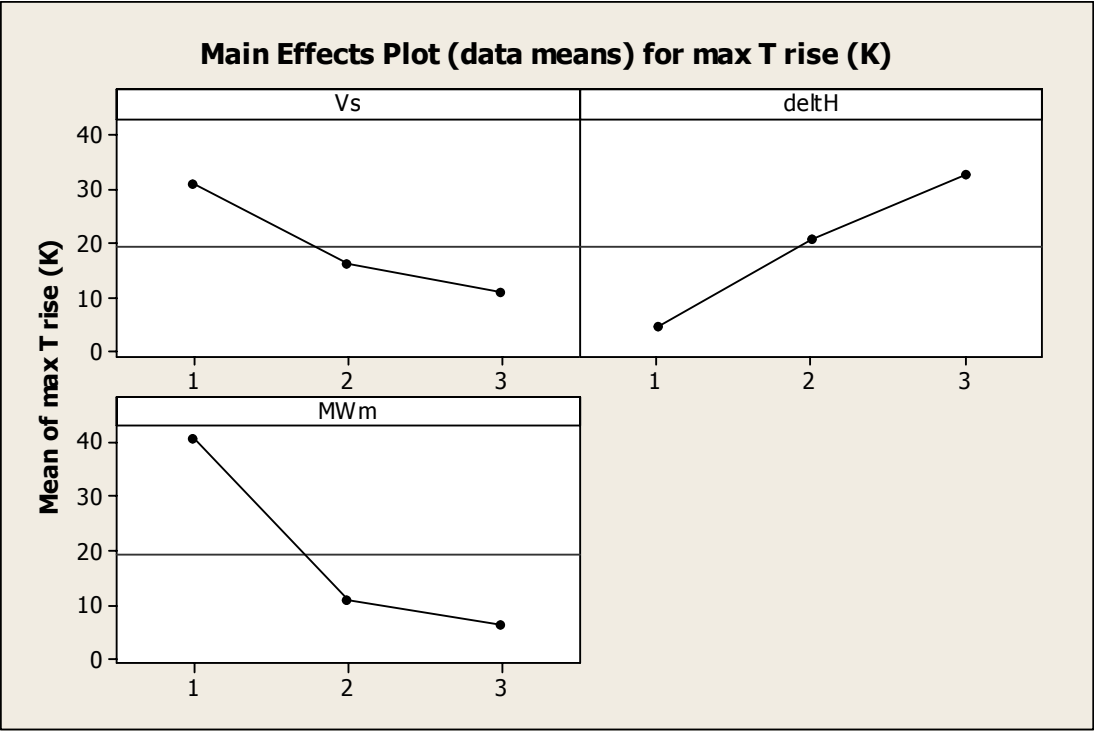
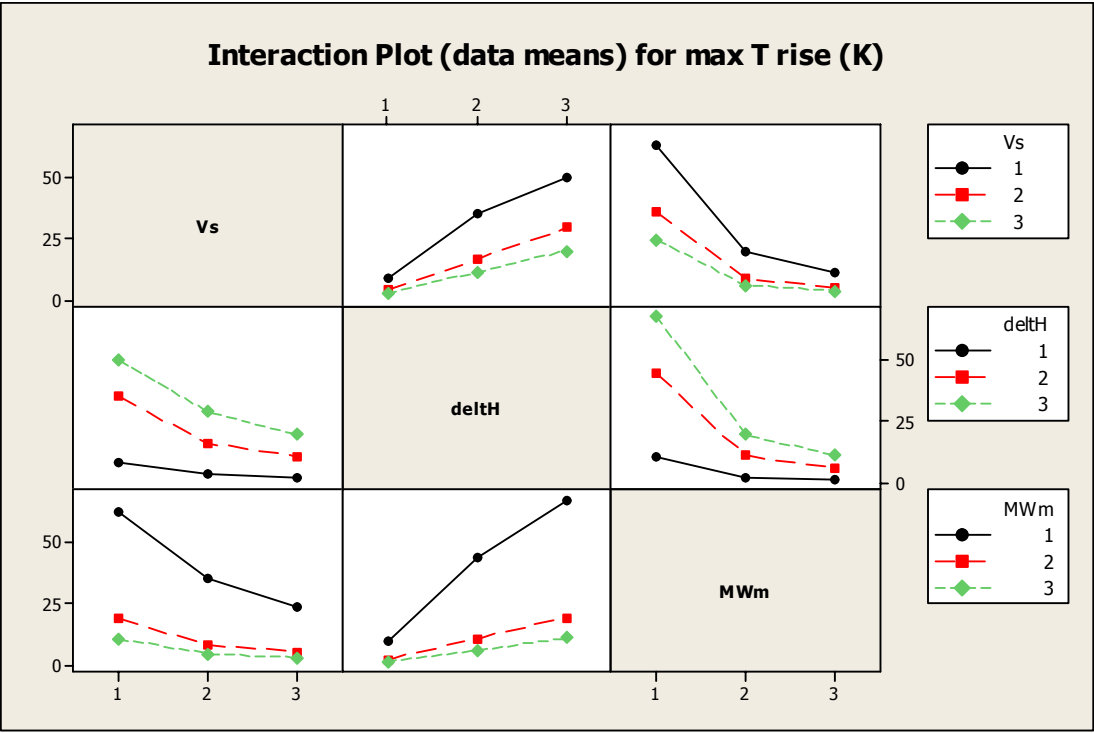


Figure 60 Curvature in Factors for Maximum Temperature Rise



(a) Main Effects Plot



(b) Interaction Plot

Figure 61 Factors Curvature for Max Temp Rise (a) main effect (b) interaction

Regression analysis is performed referring to stepwise selection results. It turns out that monomer heat capacity needs to be considered in order for the model to have a good fit. As shown in Appendix J, the regression model appears to have a good fit and good predictive ability. The verification is shown in Table 34. Table 35 lists the conditions used to test the regression model.

Table 34 Maximum Temperature Rise Predicted by Regression Model

Condition	I	II	III
experimental results	43.7	1.7	0.9
predicted results	55.8	2.0	1.0
prediction error (%)	27.7	15.9	23.3

Table 35 Conditions used for Test of Temperature Rise Regression Model

Condition	I	II	III	units
MWm	0.528	1.5	1	Kg/mol
deltH	2.85E+05	8.00E+04	3.45E+04	J/mol
Vs	0.0272	0.06	0.1	m/s
CpM	1500	2000	1850	J/Kg-K

7.3 Parameter Optimization

For a given stereolithography apparatus and given photosensitive material, Chockalingam and coworkers (2003) performed optimization on operation parameters such as layer thickness, hatch spacing, hatch style, hatch over cure, and fill cure depth in order to obtain parts with desired dimensions. In this work, the optimization performed for part dimensions is more focused on the smallest feature that SL can build given any material or apparatus available.

Based on the regression prediction models established in the previous section, response optimization can be performed to find the highest resolution or speed or maximum DOC as well as their corresponding parameter settings. Equation (68) shows the objective function to be minimized (e.g. for resolution and speed) or maximized (e.g. for DOC) subject to the constraints Equation (69). The variation bounds for design variables (i.e. significant factors) in Equation (69) are listed in Table 36. Evolver (Palisade) has been used to solve the optimization problem. It is an add-in for Microsoft Excel that uses genetic algorithms to perform optimization.

The optimization problem is formulated as follows:

$$\text{min or max} \quad y = f(x_1, x_2, x_3, \dots) \quad (68)$$

$$\text{s.t.} \quad a_i \leq x_i \leq b_i \quad (69)$$

Table 36 Parameter Range Used for Response Optimization

Factors	Low Level	High Level	Units
beam radius (wo)	1.00E-04	2.00E-04	m
monomer diffusion coefficient (Dm)	1.00E-14	1.00E-14	m ² /s
monomer glass transition temperature (Tgm)	1.00E-12	1.00E-12	K
monomer molecular weight (MWm)	0.198	2.156	Kg/mol
initiator loading wt% (wt)	1	5	wt%
initiator molecular weight (MWs)	0.164	0.418	Kg/mol
initiator absorptivity (ebx)	20	60	m ³ /mol-m
quantum efficiency of initiation (phi)	0.1	0.6	N/A
heat of polymerization (delthH)	3.45E+04	2.85E+05	J/mol
laser scanning speed (Vs)	0.02	0.1	m/s
monomer heat capacity (CpM)	1500	3300	J/Kg-K

Table 37 lists the optimization results for each response. It appears that a small beam contributes to improvement in both width resolution and curing speed. Relatively lower monomer glass transition temperature would be preferred for the concern of resolution, which however would also decrease the DOC. Low monomer diffusion coefficient benefits width resolution and DOC, while for depth resolution easier diffusion of monomer is preferable. The quantum efficiency of initiation, initiator wt% loading, initiator absorption coefficient, and initiator molecular weight are parameters that only affect depth resolution. It can be seen that high quantum efficiency and initiator loading are not necessarily good for SL. High absorptivity and low molecular weight of initiator are preferred for the depth resolution due to the correspondingly smaller penetration depth of the laser beam. Monomer molecular weight is another parameter to adjust in need of higher DOC or curing speed. The temperature rise in the resin due to the heat generated by curing can be reduced to negligible value by adjusting the laser scanning speed and adopting material with smaller heat of polymerization and higher heat capacity. For the above responses of interest, most of the important factors are material

property parameters. Process parameters such as laser power, bath temperature, and heat convection at resin surface are comparatively insignificant.

There might be other criteria to evaluate the SL process. For example, if we have a 60 μm depth resolution, the layer thickness must be half or less of standard layer thickness 4 mils (100 μm) in order for neighboring layers to attach together. This would eventually decrease the part fabrication speed (not curing speed).

Table 37 Evolver Optimization Results for Investigated Responses

Responses Optimal Conditions Factors	Width Resolution	Depth Resolution	Curing Time (width)	Max DOC	Max T rise	Units
beam radius (wo)	1.00E-04		1.00E-04			m
monomer diffusion coefficient (Dm)	1.00E-14	1.00E-12		1.00E-14		m ² /s
monomer glass transition temperature (Tgm)	186.17			223.15		K
monomer molecular weight (MWm)			1.05	1.50	1.22	Kg/mol
initiator loading wt% (wt)		1				wt%
initiator molecular weight (MWs)		0.164				Kg/mol
initiator absorptivity (ebx)		60				m ³ /mol-m
quantum efficiency of initiation (phi)		0.1				N/A
heat of polymerization (deltH)					3.45E4	J/mol
laser scanning speed (Vs)					0.1	m/s
monomer heat capacity (CpM)					3300	J/Kg-K
Optimal Responses	215 μm	60 μm	18 ms	34%	0 K	

Table 37 demonstrates the smallest part that can be obtained is about 215 μm wide (slightly larger than the beam diameter) and 60 μm deep. This is evaluated based on the kinetic parameters of the model tetraacrylate material; these values could be different for resins with different kinetics. Recall in the effect significance investigation, kinetic

parameters were not tested due to the complexity and the variety of ways people have employed to describe the photopolymerization kinetics.

The effect analysis of parameters has provided guidelines to perform cost-effective trials to improve SL fabrication performance.

7.4 Parameter Analysis using Exposure Threshold Model

As described earlier, the exposure threshold model only predicts the cured line depth (depth resolution) and width (width resolution). It doesn't provide information for part DOC or curing speed as the DOC threshold model. In this section, the effect of parameters on cure depth and line width will be investigated and sensitive parameters be identified using the exposure threshold model. Regression equations will be established to predict the cured part dimension and parameter optimization be performed to obtain the best resolution.

7.4.1 Parameter Significance Investigation

The parameters involved in the exposure threshold model are shown in Table 38 and a 2^5 full factorial design with 32 runs has been conducted to study the factor effects. For each run, the cure depth and line width of a single line part are calculated using Equations (55) and (56) and recorded.

Table 38 Parameters in Exposure Threshold Model and Their Level Values

PARAMETER	Symbol	low level (-1)	High level (+1)	Units
critical exposure	Ec	5	20	mJ/cm ²
depth of penetration	Dp	5	10	mils
laser power	PL	24	100	mW
beam radius	w ₀	0.1	0.2	mm
laser scanning speed	V _s	20	100	mm/s

The analysis of the design illustrates that all five parameters listed in Table 38 are sensitive parameters for cure depth, while four of the parameters (depth of penetration excluded) are significant factors for cured line width. The main effects plots for cure depth and line width are shown in Figures 62 and 63, respectively.

From Figure 62, it can be seen that the cure depth increases as laser power and depth of penetration increase and decreases as critical exposure, laser scanning speed, and beam radius increase. From Figure 63, it can be seen that the line width increases as laser power and beam radius increase and decreases as critical exposure and laser scanning speed decrease. The line width is not subject to the change of depth of penetration. These observations make physical sense and are consistent with Equations (56) and (57), only expressing the relations in a graphical way. Note that Equation (57) can be rewritten as:

$$L_w = w_0 \sqrt{2 \ln\left(\frac{E_{\max}}{E_c}\right)} \quad (70)$$

Equation (70) obviously shows that the line width is not dependent on the depth of penetration.

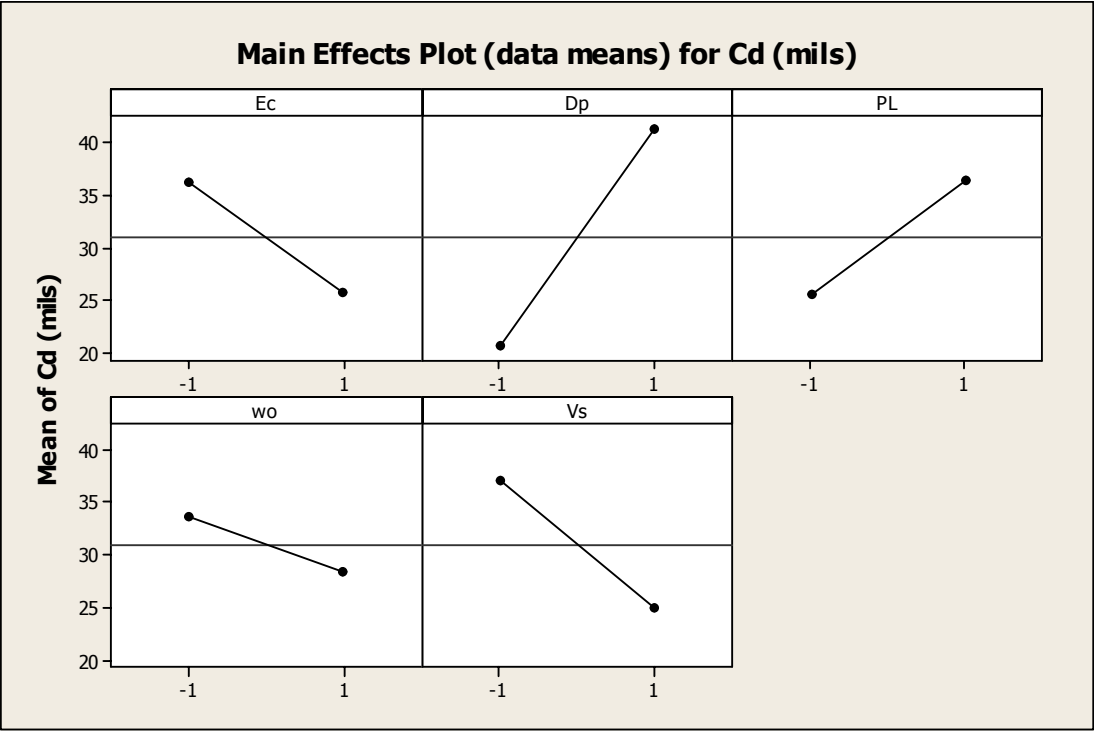


Figure 62 Main Effects Plot for Cure Depth

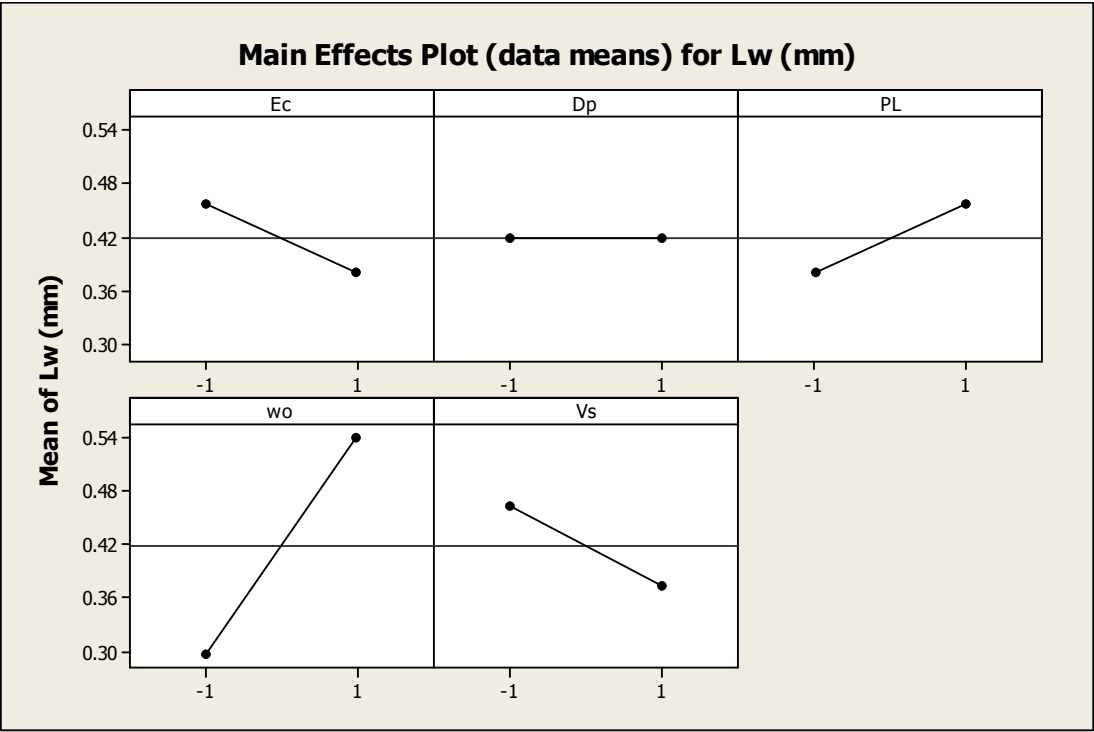


Figure 63 Main Effects Plot for Line Width

Recall the parameter effects on depth resolution (cure depth) investigated using DOC threshold model. The significant factors are initiator wt% loading and quantum efficiency of initiation and less significant ones are initiator molecular weight and initiator absorptivity. The beam radius, laser power, and laser scanning speed are insignificant comparing to these parameters. As discussed earlier, the depth of penetration is dependent on absorptivity, initiator molar concentration (molecular weight and wt% loading of the initiator), while the critical exposure by definition appears dependent on quantum efficiency of initiation. From this point of view, the parameter significance is consistent by either exposure or DOC threshold model.

Recall the parameter effects on width resolution (line width) investigated using DOC threshold model. The significant factors are beam radius and monomer glass transition and a less significant one is monomer diffusion coefficient. Both models tell that the beam radius is a significant factor for line width and depth of penetration is an insignificant one. By the DOC threshold model, the material parameters seem more important than process parameters such as laser power and scanning speed. However, not much information regarding to material property effect can be extracted from exposure threshold model.

7.4.2 Parameter Optimization

The optimization is performed based on the exposure threshold model Equations (56) and (57). The optimization problem is formulated similarly to Equations (68) and (69). The objective here is to minimize the cure depth and line width. The variation bounds of the parameters are as shown in Table 38. The optimization results by Evolver are demonstrated in Table 39.

Table 39 Evolver Optimization Results using Exposure Threshold Model

Factors Conditions Responses	critical exposure (Ec)	depth of penetration (Dp)	laser power (PL)	beam radius (wo)	scanning speed (Vs)	Optimal Response	units
cure depth (Cd)	20	5	24	0.2	100	7.8	mils
line width (Lw)	20		24	0.1	100	0.2	mm
units	mJ/cm ²	mils	mW	mm	mm/s		

From Table 39, we can see that higher critical exposure, smaller penetration depth, lower laser power, larger beam size, and faster drawing speed contribute to smaller cure depth; higher critical exposure, lower laser power, smaller beam size, and faster drawing speed lead to smaller line width. This conclusion confirms the observations in the previous section and can also be drawn from the expressions of Equations (56) and (57).

Therefore, to obtain a smaller size of part, resin with higher critical exposure and smaller penetration depth as well as laser with lower power and faster drawing speed is preferred. However, the depth of the cured line has to compromise with the width to decide desirable beam radius. From the effect analysis using DOC threshold model, we can see that when the variation of material properties also becomes an option, smaller beam size is favorable for a small part since the depth is no more significantly dependent on the beam radius. Furthermore, as shown in Table 39, the smallest part size is the same

as the beam size; while according to the analysis using DOC threshold model, it's slightly larger than the beam size due to diffusion and reaction in the vicinity of irradiation.

In summary, there are limited parameters to adjust when using the exposure threshold model to guide the SL fabrication process. Only two parameters are used to characterize material properties: critical exposure and depth of penetration. As discussed in the previous chapter, unlike other material properties such as absorptivity or molecular weight, the critical exposure is not an inherent property of the material. It is very specific to a certain SL apparatus and certain fabrication as well as post-processing conditions, and therefore has to be experimentally re-evaluated each time these conditions vary. Therefore, the parameter analysis based on the exposure threshold model cannot provide a useful guide for material development. Furthermore, what parameters affect the temperature rise during building, the SL curing speed, as well as the DOC of the part and how they affect these properties can not be investigated based on the exposure threshold.

CHAPTER 8

CONCLUSIONS & RECOMMENDATIONS

It can be concluded from this research that:

1. Due to the rapid radical photopolymerization, transient intensity rather than the exposure incident on the resin should be adopted in stereolithography process simulation. In other words, the irradiation period, although very short (1~10ms scale), cannot be ignored and it's not appropriate to consider the dark reaction only.
2. By taking diffusion limitation into account, the photopolymerization kinetic model can be extended to use in stereolithography with high laser intensity. (also see Tang, Y., 2002)
3. The stereolithography cure process model established here can be used not only to simulate and predict the cured size of a single line part, but parts with overlapping lines and stacked lines. The simulation and prediction of parts with more complex laser drawing patterns can also be expected.
4. The cure process model can be employed to investigate transient profiles of temperature, monomer, initiator, and radical concentrations, as well as their related properties such as propagation and termination rate. It simulates the cure behavior during SL fabrication process, and provides insight into the part building mechanisms.

5. The concept of critical DOC renders the cure process model a DOC threshold model, corresponding to the concept of critical exposure and exposure threshold model.
6. The laser beam radius, monomer glass transition temperature as well as monomer diffusion coefficient are sensitive parameters for width resolution; the initiator wt% loading, molecular weight and absorption coefficient as well as quantum efficiency of initiation are parameters that affect the depth resolution significantly; the laser beam radius and monomer molecular weight are two factors that affect the curing time needed to form a certain width part; the monomer diffusion coefficient, glass transition temperature, and molecular weight are sensitive parameters for the maximum degree of cure a part can reach.
7. Based on knowledge of the effective parameters, material or laser properties can be modified to improve stereolithography speed or resolution.

The following is recommended for further study:

1. If a significant shrinkage occurs upon the laser scanning (i.e. there is a big difference between the density of monomer and that of polymer), the convection phenomenon occurs. In this case, both diffusion and convection should be considered in the mass balance equations. Flach and Chartoff (1994) developed a simple polymer shrinkage model based on the degree of conversion from monomer to polymer and estimated the part shrinkage after the cure reaction. They took the effect of conversion on the shrinkage into account. In effect, the shrinkage also causes the occurrence of convection and

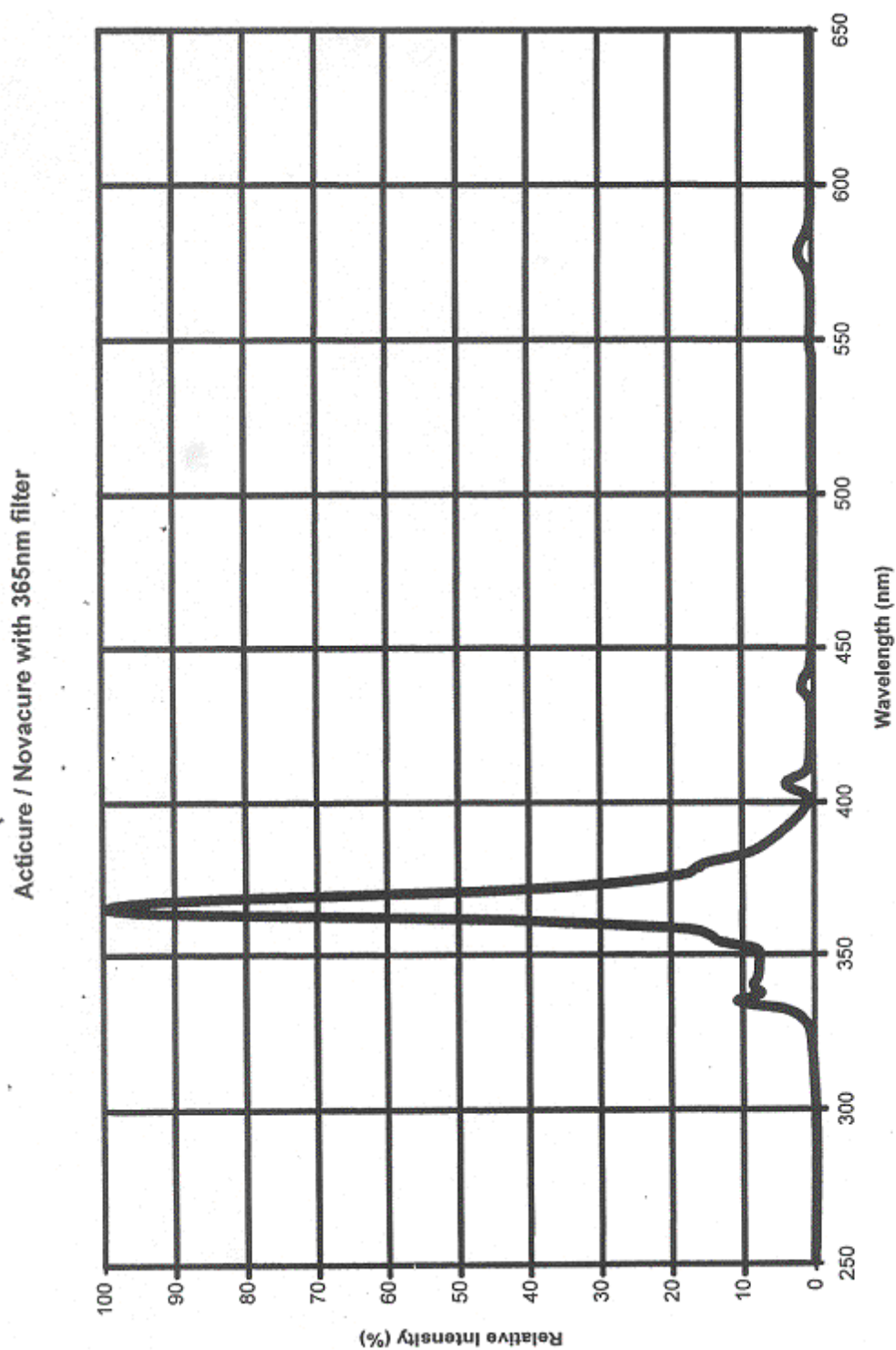
thus affects the monomer conversion. However, this was not considered in their work. In order to incorporate the interactive effects between shrinkage and conversion into the SL process model, a convection term needs to be addressed and incorporated.

2. Since most of SL resins are comprised of not only acrylate but epoxy (Melisaris, et al., 2000; Pang, et al., 2000; Steinmann, et al., 1995, 1999), a model epoxy curing system (monomer and photoinitiator) should be established and its cationic photopolymerization kinetics characterized in order to investigate the epoxy cure behavior and its interaction with the acrylate cure. This knowledge would enrich the material development guidelines prepared here. (The modeling approach presented in this work can be extended to epoxy resin or acrylate-epoxy blend.)

Finally, it should be mentioned that the possibility of extending the cure process model without changing material properties or kinetics to SL commercial resin of confidential compositions has been tested. It turns out that when extending the application of the process model from the model acrylate studied here to commercial SL resin SM 7110, the prediction error is found to be up to 30 %. This indicates that the material properties or the kinetics do need to change accordingly when the resin changes. Cationic polymerization plays a significant role in SM 7110 curing since it's composed of both acrylate and epoxy. That the exposure threshold model does not need to take material change into account is a defect and also an advantage. One big benefit of the SL cure process model established here is to investigate the effects of process, laser, or material properties and to prepare material development guidelines for SL improvement.

APPENDIX A

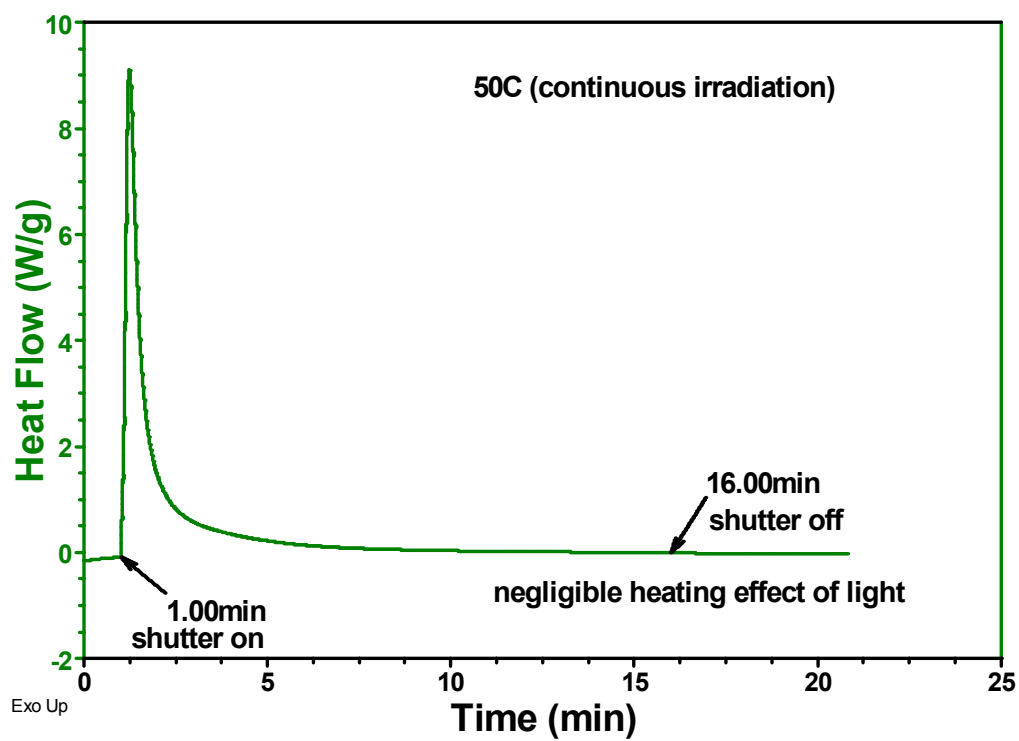
NOVECURE OUTPUT WITH 365NM FILTER (EXFO)



8/11/99

APPENDIX B

NEGLIGIBLE HEATING EFFECT OF LIGHT IN DPC EXPERIMENTS



APPENDIX C

A BRIEF LITERATURE REVIEW ON GEL POINT ESTIMATION

Gel point is a critical value for the extent of reaction above which the produced polymer becomes of infinite molecular weight. Flory (1953) developed a theory to estimate the gel point for the nonlinear condensation polymerization systems. The following assumptions were used: (i) all functional groups of each kind of structural unit, A and B, are equally reactive, i.e. the reactivity of an A or B group is independent of the size or structure of the molecule to which it is attached; (ii) the condensation between A and B on the same molecule is negligible, i.e. cyclization can be ignored. If A and B groups are initially present in equivalent quantities and only one of them has a functionality greater than two, the branching probability (i.e. the probability that a given functional group of a branch unit leads via a chain of bifunctional units to another branch unit), α , can be reduced to be the square of the conversion of the functional units, D .

$$\alpha = D^2 \quad (71)$$

Equation (72) states the critical condition for formation of infinite networks (Flory, 1953):

$$\alpha_c = \frac{1}{f-1} \quad (72)$$

where α_c is the critical value of α , and f is the functionality of the branching unit, A or B, whichever has a functionality greater than two.

Then the gel point, D_c , for the condensation of the two functional units, A and B, can be obtained from the following equation:

$$D_c = \sqrt{\frac{1}{f-1}} \quad (73)$$

Miller et al. (1979), Macosko and Miller (1976), and Valles and Macosko (1979) derived the weight average molecular weight for the nonlinear stepwise polymerization system, and obtained the gel point as the conversion where the molecular weight diverges. Their results are in agreement with Flory's theory. Miller and Macosko (1976) obtained results that agree with Flory's theory, too, by deriving the probability of a finite chain in a polymer network (from which the gel point was estimated). Miller et al. (1979) and Macosko and Miller (1976) also extended the use of Flory's model to include the case where more than one type of branching unit is present in the condensation system.

According to Flory's theory (1953), Miller and Macosko (1976) and Macosko and Miller (1976) applied the same equations they developed for stepwise reactions to cross-linking reactions of polymer chains. The cross-linking occurs by reacting side groups on long, linear polymer chains or through unsaturation in the chain backbone. They assumed all the reactive groups are of the same type and derived the gel point as a function of the weight average degree of polymerization of the initial mixture of long chains (Macosko and Miller, 1976).

Macosko and Miller (1976) also derived an expression to estimate the gel point for networks formed by chain polymerization. The chainwise reaction involves initiation, propagation, and termination. The gel point was found to be related to the monomer functionality, probability that a growing chain adds one more unit, probability that a chain terminates by combination, and the mole fraction of functional groups. Landin and Macosko (1983, 1988) utilized this relation to express the gel point for the chainwise co-

polymerization of mono- and di-functional monomers. Miller and Macosko (1987, 1988) employed the chain length and site distribution to demonstrate the gel point for the network formed by chain crosslinking as a function of the expected number of sites on a chain randomly chosen by site. Dotson and co-workers (1988) derived the weight-average molecular weight for the crosslinking free radical polymerization and obtained the gel point as the conversion where the molecular weight goes to infinity. Okay (1994) also derived an equation to approximate the gel point for the free radical chain copolymerization and cross-linking system. The gel point was expressed as a function of the accumulated average chain lengths of the primary molecules, the initial mole fraction of the functional groups in the monomer mixture, and the reactivity of the functional groups. All these theoretical derivations for gel point of a chain polymerization system, however, were difficult to parameterize and not validated in practice.

González-Romero and Macosko (1985) analyzed the kinetics of the free radical crosslinking polymerization and derived a relation between the gel point and gel time for a radical polymerization system that involves inhibition. They measured the viscosity of the system during the reaction and took the time at which the viscosity goes to infinity as gel time. The gel point thus can be calculated. This relation involving the rate constants for inhibition and propagation was verified experimentally. In this relation, the inhibitor was assumed to be ideal, i.e. the monomer doesn't react with the radicals until the inhibitor is consumed.

Suematsu and Kohno (2000) separated the critical point of branched polymers into two terms: intermolecular reaction and cyclization, i.e. $D_c = D(\text{inter}) + D(\text{ring})$. They took this idea as a starting point and deduced an analytic expression for the gel point of a

polymerizing system consisting of same type functional units (Equation 74). Each functional unit is assumed to have an equal chance to undergo cyclization.

$$D_c = \frac{1}{f-1} + \frac{2[\Gamma]}{fC} \quad (74)$$

where D_c is the conversion at which gelation occurs, f is the functionality, $[\Gamma]$ is the molar concentration of rings formed by cyclization, and C is the initial monomer concentration of the system. Assuming that the gel lattice has high dimensions, Suematsu and Kohno (2000) used a percolation model and expressed the molar concentration of cyclics in a form of the solution of the ring distribution function for the site-bond percolation problem.

If the cyclization in the polymerizing system is negligible, Equation (74) can be reduced to the following:

$$D_c = \frac{1}{f-1} \quad (75)$$

This is in agreement with the Flory's theory if the branched polymerization here is considered as a condensation. In Flory's theory, if only one type of functional group is present and these groups are capable of condensing with one another, then the branching probability α equals the extent of reaction D , not D^2 . Incorporating this relation into the critical condition Equation (72), the gel point expression is the same as Equation (75).

Miller and Macosko (1976), Miller et al. (1979), and Macosko and Miller (1976) also obtained the same gel point expression for the stepwise homo-polymerization.

If considering the investigated tetraacrylate crosslinking system in our work as a condensation (model of Suematsu and Kohno (2000) is for general branched polymers, chainwise or stepwise, and does not need this assumption) and assuming the cyclization to be negligible, the gel point of the system can be estimated to be ~14%. The critical DOC determined (9~10%) for the DOC threshold model (Chapter 6) is thus found to be lower than the gel point, which indicates that the produced polymer doesn't have to achieve an infinite molecular weight to form a solid part.

APPENDIX D

MINITAB REGRESSION OUTPUT OF REDUCED MODEL FOR WIDTH RESOLUTION

Regression Analysis: width resolution (μm) versus wo, Tgm, wo*Tgm

The regression equation is
width resolution (μm) = 530 + 164 wo + 151 Tgm + 45.8 wo*Tgm

Predictor	Coef	SE Coef	T	P	VIF
Constant	529.750	3.455	153.33	0.000	
wo	164.250	3.455	47.54	0.000	1.0
Tgm	151.250	3.455	43.78	0.000	1.0
wo*Tgm	45.750	3.455	13.24	0.000	1.0

S = 9.77241 R-Sq = 99.9% R-Sq(adj) = 99.8%

PRESS = 1528 R-Sq(pred) = 99.63%

Analysis of Variance

Source	DF	SS	MS	F	P
Regression	3	415582	138527	1450.55	0.000
Residual Error	4	382	95		
Total	7	415964			

Source	DF	Seq SS
wo	1	215824
Tgm	1	183013
wo*Tgm	1	16745

APPENDIX E

MINITAB STEPWISE REGRESSION OUTPUT FOR WIDTH RESOLUTION

Stepwise Regression: width resolution versus wo, Dm, ...

Alpha-to-Enter: 0.15 Alpha-to-Remove: 0.15

Response is width resolution on 7 predictors, with N = 8

Step	1	2	3	4	5
Constant	529.8	529.8	529.8	529.8	529.8
wo	164.25	164.25	164.25	164.25	164.25
T-Value	2.54	7.94	47.54	74.23	293.82
P-Value	0.044	0.001	0.000	0.000	0.000
Tgm		151.25	151.25	151.25	151.25
T-Value		7.31	43.78	68.36	270.56
P-Value		0.001	0.000	0.000	0.000
wo*Tgm			45.75	45.75	45.75
T-Value			13.24	20.68	81.84
P-Value			0.000	0.000	0.000
Dm				5.75	5.75
T-Value				2.60	10.29
P-Value				0.080	0.009
wo*Dm					-3.75
T-Value					-6.71
P-Value					0.022
S	183	58.5	9.77	6.26	1.58
R-Sq	51.89	95.88	99.91	99.97	100.00
R-Sq(adj)	43.87	94.24	99.84	99.93	100.00
PRESS	355803	43843.8	1528.00	835.556	80.0000
R-Sq(pred)	14.46	89.46	99.63	99.80	99.98

APPENDIX F

REGRESSION PREDICTION MODEL FOR DEPTH RESOLUTION

Regression Analysis: depth resolution versus phi, wt, ...

The regression equation is

depth resolution = 83.5 + 1640 phi + 31.7 wt + 4.15 ebx - 846 MWs - 303 phi*wt
+ 2941 phi*MWs - 17.9 ebx*phi - 5.90E+12 ebx*Dm
+ 6.99E+14 Dm*MWs

Predictor	Coef	SE Coef	T	P	VIF
Constant	83.49	73.12	1.14	0.297	
phi	1639.9	170.0	9.65	0.000	12.5
wt	31.70	10.34	3.07	0.022	3.0
ebx	4.147	1.139	3.64	0.011	3.6
MWs	-845.9	176.2	-4.80	0.003	3.5
phi*wt	-303.25	24.04	-12.61	0.000	5.2
phi*MWs	2940.9	378.6	7.77	0.000	8.2
ebx*phi	-17.925	2.404	-7.46	0.000	7.0
ebx*Dm	-5.90096E+12	9.48091E+11	-6.22	0.001	3.7
Dm*MWs	6.98905E+14	1.33541E+14	5.23	0.002	3.6

S = 48.0799 R-Sq = 99.3% R-Sq(adj) = 98.3%

PRESS = 92514.2 R-Sq(pred) = 95.57%

Analysis of Variance

Source	DF	SS	MS	F	P
Regression	9	2076450	230717	99.80	0.000
Residual Error	6	13870	2312		
Total	15	2090320			

Source	DF	Seq SS
phi	1	755161
wt	1	354620
ebx	1	166872
MWs	1	74256
phi*wt	1	367842
phi*MWs	1	139502
ebx*phi	1	128522
ebx*Dm	1	26354
Dm*MWs	1	63320

APPENDIX G

REGRESSION PREDICTION MODEL FOR WIDTH RESOLUTION

Regression Analysis: width resolution (µm) versus wo, Tgm, ...

The regression equation is

$$\begin{aligned} \text{width resolution } (\mu\text{m}) = & 1786 + 44289486 \text{ wo} - 18.5 \text{ Tgm} + 0.0479 \text{ Tgm}^2 \\ & - 459543 \text{ wo*Tgm} + 1252 \text{ wo*Tgm}^2 + 2.95\text{E}+08 \text{ Dm*Tgm}^2 \end{aligned}$$

Predictor	Coef	SE Coef	T	P
Constant	1786.3	483.3	3.70	0.004
wo	44289486	2861864	15.48	0.000
Tgm	-18.499	4.923	-3.76	0.003
Tgm^2	0.04795	0.01242	3.86	0.003
wo*Tgm	-459543	29177	-15.75	0.000
wo*Tgm^2	1252.38	73.62	17.01	0.000
Dm*Tgm^2	294949652	74175681	3.98	0.002

S = 5.15323 R-Sq = 100.0% R-Sq(adj) = 99.9%

PRESS = 839.094 R-Sq(pred) = 99.89%

Analysis of Variance

Source	DF	SS	MS	F	P
Regression	6	789990	131665	4958.05	0.000
Residual Error	11	292	27		
Total	17	790282			

Source	DF	Seq SS
wo	1	399022
Tgm	1	270600
Tgm^2	1	87419
wo*Tgm	1	24843
wo*Tgm^2	1	7685
Dm*Tgm^2	1	420

Unusual Observations

Obs	wo	width resolution (µm)	Fit	SE Fit	Residual	St Resid
12	0.000200	890.00	882.07	3.49	7.93	2.09R

R denotes an observation with a large standardized residual.

No evidence of lack of fit (P >= 0.1).

APPENDIX H

REGRESSION PREDICTION MODEL FOR CURING SPEED (WIDTH)

Regression Analysis: time (s) (wi versus wo, wo^2, wo*MWm^2, wo^2*MWm

The regression equation is

$$\text{time (s) (width)} = 0.0189 - 101 \text{ wo} + 894768 \text{ wo}^2 + 1.13 \text{ wo}^2 \text{ MWm}^2 - 23697 \text{ wo}^2 \text{ MWm}$$

Predictor	Coef	SE Coef	T	P
Constant	0.018938	0.002203	8.60	0.001
wo	-101.02	32.10	-3.15	0.035
wo^2	894768	105755	8.46	0.001
wo*MWm^2	1.1304	0.4219	2.68	0.055
wo^2*MWm	-23697	5927	-4.00	0.016

S = 0.000121933 R-Sq = 100.0% R-Sq(adj) = 100.0%

PRESS = 1.004802E-06 R-Sq(pred) = 99.80%

Analysis of Variance

Source	DF	SS	MS	F	P
Regression	4	0.00049545	0.00012386	8330.96	0.000
Residual Error	4	0.00000006	0.00000001		
Total	8	0.00049551			

Source	DF	Seq SS
wo	1	0.00049407
wo^2	1	0.00000100
wo*MWm^2	1	0.00000014
wo^2*MWm	1	0.00000024

APPENDIX I

REGRESSION PREDICTION MODEL FOR MAXIMUM DOC

Regression Analysis: max DOC versus Dm, Tgm, ...

The regression equation is

$$\begin{aligned} \text{max DOC} = & 0.474 + 3.20\text{E}+11 \text{ Dm} - 0.00304 \text{ Tgm} + 0.000007 \text{ Tgm}^2 + 6.74 \text{ MWm} \\ & - 1.84 \text{ MWm}^2 - 0.0732 \text{ Tgm} \cdot \text{MWm} + 0.0199 \text{ Tgm} \cdot \text{MWm}^2 + 0.000198 \text{ Tgm}^2 \cdot \text{MWm} \\ & - 0.000054 \text{ Tgm}^2 \cdot \text{MWm}^2 - 3.76\text{E}+09 \text{ Dm} \cdot \text{Tgm} + 10302010 \text{ Dm} \cdot \text{Tgm}^2 \\ & - 8.34\text{E}+09 \text{ Dm} \cdot \text{MWm} + 2.82\text{E}+09 \text{ Dm} \cdot \text{MWm}^2 \end{aligned}$$

Predictor	Coef	SE Coef	T	P
Constant	0.4737	0.1008	4.70	0.000
Dm	3.20288E+11	87314665530	3.67	0.003
Tgm	-0.003039	0.001025	-2.96	0.011
Tgm^2	0.00000737	0.00000258	2.85	0.014
MWm	6.7374	0.2051	32.85	0.000
MWm^2	-1.83563	0.08471	-21.67	0.000
Tgm*MWm	-0.073176	0.002088	-35.05	0.000
Tgm*MWm^2	0.0199302	0.0008623	23.11	0.000
Tgm^2*MWm	0.00019815	0.00000526	37.64	0.000
Tgm^2*MWm^2	-0.00005398	0.00000217	-24.82	0.000
Dm*Tgm	-3755343521	891121051	-4.21	0.001
Dm*Tgm^2	10302010	2249057	4.58	0.001
Dm*MWm	-8343895499	3836045842	-2.18	0.049
Dm*MWm^2	2820055085	1587589969	1.78	0.099

S = 0.00150408 R-Sq = 100.0% R-Sq(adj) = 100.0%

PRESS = 0.000141634 R-Sq(pred) = 99.94%

Analysis of Variance

Source	DF	SS	MS	F	P
Regression	13	0.236345	0.018180	8036.37	0.000
Residual Error	13	0.000029	0.000002		
Total	26	0.236374			

Source	DF	Seq SS
Dm	1	0.001494
Tgm	1	0.128524
Tgm^2	1	0.043293
MWm	1	0.018624
MWm^2	1	0.003970
Tgm*MWm	1	0.026320
Tgm*MWm^2	1	0.004900
Tgm^2*MWm	1	0.007569
Tgm^2*MWm^2	1	0.001394
Dm*Tgm	1	0.000192
Dm*Tgm^2	1	0.000047
Dm*MWm	1	0.000008
Dm*MWm^2	1	0.000007

APPENDIX J

REGRESSION PREDICTION MODEL FOR MAXIMUM TEMPERATURE RISE

Regression Analysis: max T rise (K) versus delth, Vs*delth, ...

The regression equation is

$$\begin{aligned} \text{max T rise (K)} = & 1.10 + 0.000522 \text{ delth} - 0.00270 \text{ Vs*delth} - 0.000503 \text{ delth*MWm} \\ & + 0.000176 \text{ delth*MWm}^2 - 0.000000 \text{ CpM*delth} \\ & + 0.0129 \text{ Vs}^2\text{delth*MWm} \end{aligned}$$

Predictor	Coef	SE Coef	T	P
Constant	1.104	1.498	0.74	0.467
delth	0.00052242	0.00002567	20.35	0.000
Vs*delth	-0.0026996	0.0002243	-12.04	0.000
delth*MWm	-0.00050308	0.00004547	-11.06	0.000
delth*MWm^2	0.00017646	0.00002592	6.81	0.000
CpM*delth	-0.00000003	0.00000001	-5.17	0.000
Vs^2*delth*MWm	0.012856	0.001800	7.14	0.000

S = 5.10820 R-Sq = 96.1% R-Sq(adj) = 95.3%

PRESS = 1559.30 R-Sq(pred) = 91.97%

Analysis of Variance

Source	DF	SS	MS	F	P
Regression	6	18651.9	3108.6	119.13	0.000
Residual Error	29	756.7	26.1		
Total	35	19408.6			

Source	DF	Seq SS
delth	1	4544.0
Vs*delth	1	3036.8
delth*MWm	1	8366.5
delth*MWm^2	1	811.9
CpM*delth	1	561.9
Vs^2*delth*MWm	1	1330.8

Unusual Observations

Obs	delth	max T rise (K)	Fit	SE Fit	Residual	St Resid
4	159750	74.480	53.719	1.864	20.761	4.37R
30	285000	70.370	78.802	3.601	-8.432	-2.33R

R denotes an observation with a large standardized residual.

No evidence of lack of fit (P >= 0.1).

REFERENCES

- Anseth, K.S. and Bowman, C.N. (1993) 'Reaction Diffusion Enhanced Termination in Polymerizations of Multifunctional Monomers', *Polymer Reaction Engineering*, Vol.1, pp.499-520.
- Anseth, K.S., Bowman, C.N., and Peppas, N.A. (1994a) 'Polymerization Kinetics and Volume Relaxation Behavior of Photopolymerized Multifunctional Monomers Producing Highly Crosslinked Networks', *Journal of Polymer Science: Part A: Polymer Chemistry*, Vol.32, pp.139-147.
- Anseth, K.S., Wang, C.M., and Bowman, C.N. (1994b) 'Reaction Behaviour and Kinetic Constants for Photopolymerizations of Multi(meth)acrylate Monomers', *Polymer*, Vol.35, pp.3243-3250.
- Bass, J., Dugdale, J.S., Foiles, C.L., and Myers, A (1985) in Hellwege, K.H. and Madelung, O. (Eds.) *Numerical Data and Functional Relationships in Science and Technology*, New York: Springer-Verlag, pp.222.
- Brandrup, J. and Immergut E.H. (Ed.) (1989) *Polymer Handbook*, 3rd Edition, New York: John Wiley & Sons, V/77.
- Bowman, C.N. and Peppas, N.A. (1991) 'Coupling of Kinetics and Volume Relaxation during Polymerizations of Multiacrylates and Multimethacrylates', *Macromolecules*, Vol.24, pp.1914-1920.
- Buback, M., Degener, B., and Huckestein, B. (1989) 'Conversion Dependence of Free-Radical Polymerization Rate Coefficients from Laser-Induced Experiments, 1', *Makromol. Chem., Rapid Commun.*, Vol.10, pp.311-316.
- Buback, M. (1990) 'Free-Radical Polymerization up to High Conversion. A General Kinetic Treatment', *Makromol. Chem.*, Vol.191, pp.1575-1587.
- Bueche, F. (1962) *Physical Properties of Polymers*, New York: Interscience.
- Burel, F., Lecamp, L., Youssef, B., Bunel, C., and Saiter, J-M. (1999) 'Synthesis and Photoinitiated Polymerization of a New Urethane Acrylate Monomer: Influence of Polymerization Temperature', *Thermochimica Acta*, Vol.326, pp.133-141.
- Cho, H.S., Park, W.S., Choi, B.W., and Leu, M.C. (2000) 'Determining Optimal Parameters for Stereolithography Processes via Genetic Algorithm', *Journal of Manufacturing Systems*, Vol.19, pp.18-27.

- Chockalingam, K., Jawahar, N., and Vijaybabu, E. R. (2003) 'Optimization of Process Parameters in Stereolithography using Genetic Algorithm', *Proceedings of SPIE-The International Society for Optical Engineering*, 5062 (Pt. 1, Smart Materials, Structures, and Systems), pp.417-424.
- Cook, W.D. (1992) 'Thermal Aspects of the Kinetics of Dimethacrylate Photopolymerization', *Polymer*, Vol.33, pp.2152-2161.
- Cook, W.D. (1993) 'Photopolymerization Kinetics of Oligo(ethylene oxide) and Oligo(methylene) Oxide Dimethacrylates', *J. Polym. Sci. Part A: Polym. Chem.*, Vol.31, pp.1053-1067.
- Crivello, J.V. and Dietliker, K. (1998) *Photoinitiators for Free Radical, Cationic & Anionic Photopolymerisation*, 2nd Edition, Vol. III in Bradley, G. (Ed.) *Chemistry & Technology of UV & EB Formulation for Coatings, Inks & Paints*, New York: John Wiley & Sons.
- DiGuilio, R.M. and Teja, A.S. (1990) 'Thermal Conductivity of Poly(ethylene glycols) and Their Binary Mixtures', *Journal of Chemical and Engineering Data*, Vol.35, pp.117-121.
- Dotson, N.A, Galván, R., and Macosko, C.W. (1988) 'Structural Development during Nonlinear Free-Radical Polymerizations', *Macromolecules*, Vol.21, pp.2560-8.
- Eschl, J., Blumenstock, T., and Eyerer, P. (1999) 'Comparison of the Curing Process of Epoxy and Acrylate Resins for Stereolithography by Means of Experimental Investigations and FEM – Simulation', *Solid Freeform Fabrication Symposium Proceedings*, pp.453-460.
- Esposito Corcione, C., Greco, A., and Maffezzoli, A. (2003) 'Photopolymerization Kinetics of an Epoxy Based Resin for Stereolithography', *Journal of Thermal Analysis and Calorimetry*, Vol.72 (2), pp.687-693.
- Esposito Corcione, C., Greco, A., and Maffezzoli, A. (2004) 'Photopolymerization Kinetics of an Epoxy-Based Resin for Stereolithography', *Journal of Applied Polymer Science*, Vol.92 (6), pp. 3484-3491.
- Flach, L. and Chartoff, R.P. (1994) 'A Simple Polymer Shrinkage Model Applied to Stereolithography', *Solid Freeform Fabrication Symposium Proceedings*, pp.225-233.
- Flach, L. and Chartoff, R.P. (1995a) 'A Process Model for Nonisothermal Photopolymerization with a Laser Light Source. I: Basic Model Development', *Polymer Engineering and Science*, Vol. 35, pp.483-492.
- Flach, L. and Chartoff, R.P. (1995b) 'A Process Model for Nonisothermal

- Photopolymerization with a Laser Light Source. II: Behavior in the Vicinity of a Moving Exposed Region”, *Polymer Engineering and Science*, Vol. 35, pp.493-498.
- Flory, P.J. (1953) *Principles of Polymer Chemistry*, Ithaca, NY: Cornell University Press.
- Fouassier, J.-P. (1995) *Photoinitiation, Photopolymerization, and Photocuring – Fundamentals and Applications*, Cincinnati, OH: Hanser/Gardner Publications.
- González-Romero, V.M. and Macosko, C.W. (1985) ‘Viscosity Rise during Free Radical Crosslinking Polymerization with Inhibition’, *Journal of Rheology*, Vol.29, pp.259-272.
- Goodner, M.D., Lee, H.R., and Bowman, C.N. (1997) ‘Method for Determining the Kinetic Parameters in Diffusion-controlled Free-Radical Homopolymerizations’, *Ind. Eng. Chem. Res.*, Vol.36, pp.1247-1252.
- Goodner, M.D. and Bowman, C.N. (1998) ‘Modeling and Experimental Investigation of Light Intensity and Initiator Effects on Solvent-Free Photopolymerization’, in Long, T.E. and Hunt M.O. (Eds.), *Solvent-Free Polymerizations and Processes: Minimization of Conventional Organic Solvents*, Washington, DC: American Chemical Society, Vol.713, pp.220-231.
- Goodner, M.D. and Bowman, C.N. (1999) ‘Modeling Primary Radical Termination and Its Effects on Autoacceleration in Photopolymerization Kinetics’, *Macromolecules*, Vol.32, pp.6552-6559.
- Goodner, M.D. and Bowman, C.N. (2002) ‘Development of Comprehensive Free Radical Photopolymerization Model Incorporating Heat and Mass Transfer Effects in Thick Films’, *Chemical Engineering Science*, Vol.57, pp.887-900.
- Hur, S. S., Lee, J. H., and Youn, J. R. (1997) ‘A Study on Simulation of the Deformation of 3-D Stereolithography Products’, *Han'guk Somyu Konghakhoechi*, Vol.34(6), pp.374-385.
- Hur, S. S. and Youn, J. R. (2000) ‘Thermal Deformation of a Photo-cured Polymer for the Analysis of Stereolithography’, *Polymer-Plastics Technology and Engineering*, Vol.39 (4), pp.651-666.
- Jacobs, P.F. (1992) *Rapid Prototyping & Manufacturing: Fundamentals of Stereolithography*, Dearborn, MI: Society of Manufacturing Engineers.
- Jayanthi, S., Keefe, M., and Gargiulo, E. P. (1994) ‘Studies in Stereolithography: Influence of Process Parameters on Curl Distortion in Photopolymer Models’, *Solid Freeform Fabrication Symposium Proceedings*, pp.250-258.

- Kahle, O., Wielsch, U., Metzner, H., Bauer, J., Uhlig, C., and Zawatzki, C. (1998) 'Glass Transition Temperature and Thermal Expansion Behaviour of Polymer Films Investigated by Variable Temperature Spectroscopic Ellipsometry', *Thin Solid Films*, Vol.313-314, pp.803-807.
- Landin, D.T. and Macosko, C.W. (1983) 'Rheological Changes during the Copolymerization of Vinyl and Divinyl Monomers', *Organic Coatings and Applied Polymer Science Proceedings: Preprints of Papers*, Vol.48, pp.433-439.
- Landin, D.T. and Macosko, C.W. (1988) 'Cyclization and Reduced Reactivity of Pendant Vinyls during the Copolymerization of Methyl Methacrylate and Ethylene Glycol Dimethacrylate', *Macromolecules*, Vol.21, pp.846-851.
- Lecamp, L., Youssef, B., and Bunel, C. (1997) 'Photoinitiated Polymerization of a Dimethacrylate Oligomer: 1. Influence of Photoinitiator Concentration, Temperature and Light Intensity', *Polymer*, Vol.38, pp.6089-6096.
- Lecamp, L., Youssef, B., Bunel, C., and Lebaudy, P. (1999) 'Photoinitiated Polymerization of a Dimethacrylate Oligomer: Part 3. Postpolymerization Study', *Polymer*, Vol.40, pp.6313-6320.
- Mack, C.A. (1985) 'Prolith: a Comprehensive Optical Lithography Model', *SPIE Optical Microlithography IV*, Vol.538, pp.207-220.
- Mack, C.A. (1986) 'Analytical Expression for the Standing Wave Intensity in Photoresist', *Applied Optics*, Vol.25, pp.1958-1961.
- Mack, C.A. (1994) 'Standing Waves in Photoresist', *Microlithography World*, pp.22-24.
- Macosko, C.W. and Miller, D.R. (1976) 'A New Derivation of Average Molecular Weight of Nonlinear Polymers', *Macromolecules*, Vol.9, pp.199-206.
- Maffezzoli A., Micelli, F., Terzi R., and Luprano, V.A.M. (2001), 'Characterization of the Kinetic Behavior of Resin Modified Glass-Ionomer Cements by DSC, TMA and Ultrasonic Wave Propagation', *Journal of Materials Science: Materials in Medicine*, Vol.12, pp.151-156.
- Maffezzoli A. and Terzi R. (1995), 'Thermal Analysis of Visible-Light-Activated Dental Composites', *Thermochimica Acta*, Vol.269/270, pp.319-335.
- Maffezzoli, A. and Terzi, R. (1998) 'Effect of Irradiation Intensity on the Isothermal Photopolymerization Kinetics of Acrylic Resins for Stereolithography', *Thermochimica Acta*, Vol.321, pp.111-121.
- Marten, F.L. and Hamielec, A.E. (1979), 'High Conversion Diffusion-Controlled Polymerization', *American Chemical Society Symposium*, Ser.104, pp.43-70.

- Marten, F.L. and Hamielec, A.E. (1982), 'High Conversion Diffusion-Controlled Polymerization of Styrene I', *Journal of Applied Polymer Science*, Vol.27, pp.489-505.
- Mateo, J.L., Serrano, J., and Bosch, P. (1997), 'Photopolymerization of Di- and Tetrafunctional Methacrylic Monomers in a Polymeric Medium: Kinetics and Evidence of Reaction Diffusion throughout the Photopolymerization Reaction', *Macromolecules*, Vol.30, pp.1285-1288.
- Melisaris, A.P. et al. (2000) 'Liquid, Radiation-curable Composition, Especially for Producing Flexible Cured Articles by Stereolithography', *United States Patent*, Pat. No. 6,136,497.
- Miller, D.R., and Macosko, C.W. (1976) 'A New Derivation of Post Gel Properties of Network Polymers', *Macromolecules*, Vol.9, pp.206-211.
- Miller, D.R., Valles, E.M., and Macosko, C.W. (1979) 'Calculation of Molecular Parameters for Stepwise Polyfunctional Polymerization', *Polymer Engineering and Science*, Vol.19, pp.272-283.
- Miller, D.R. and Macosko, C.W. (1987) 'Molecular Weight Relations for Crosslinking of Chains with Length and Site Distribution', *Journal of Polymer Science: Part B: Polymer Physics*, Vol.25, pp.2441-69.
- Miller, D.R. and Macosko, C.W. (1988) 'Network Parameters for Crosslinking of Chains with Length and Site Distribution', *Journal of Polymer Science: Part B: Polymer Physics*, Vol.26, pp.1-54.
- Nagamori, S. and Yoshizawa, T. (2001), 'Research on Solidification of Resin in Stereolithography (Comparison between Measured and Estimated Shapes of Solidified Resin, and Manufacturing Accuracy of Photo-cured Model)', *SPIE's International Symposium on Intelligent Systems and Advanced Manufacturing* (Opto-Mechatronic Systems).
- Nagamori, S. and Yoshizawa, T. (2003), 'Research on Shape of Solidified Resin in Stereolithography', *Proceedings of SPIE-The International Society for Optical Engineering*, 5058 (Optical Technology and Image Processing for Fluids and Solids Diagnostics), pp.447-456.
- Neter, J., Kutner, M.H., Nachtsheim, C.J., and Wasserman, W. (1996) *Applied Linear Statistical Models*, New York: McGraw-Hill.
- Okay, O. (1994) 'Kinetics of Gelation in Free Radical Crosslinking Copolymerization', *Polymer*, Vol.35, pp.2613-18.

- Onuh, S.O. and Hon, K.K.(1998a) ‘Optimising Build Parameters for Improved Surface Finish in Stereolithography’, *International journal of Machine Tools Manufacture*, Vol.38, pp.329-342.
- Onuh, S.O. and Hon, K.K.(1998b) ‘Application of the Taguchi Method and New Hatch Styles for Quality Improvement in Stereolithography’, *Proceedings of the Institution of Mechanical Engineers, Part B*, Vol.212, pp.461-472.
- Pananakis, D. and Watts, D.C. (2000) ‘Incorporation of the Heating Effect of the Light Source in a Non-isothermal Model of a Visible-light-cured Resin Composites’, *J. Mat. Sci.*, Vol.35, pp.4589-4600.
- Pang, T.H. et al. (2000) ‘Liquid Radiation-curable Composition Especially for Producing Cured Articles by Stereolithography having High Heat Deflection Temperatures’, *United States Patent*, Pat. No. 6,100,007.
- Rosen, D.W. (2002) ‘Stereolithography Technology — Course Material for ME7227: Rapid Prototyping in Engineering’.
- Satio, A. (1993) ‘A Study on Development of 3D Model Stereo-Lithography’, Fiscal 1992, Ministry of Education, Japan, S No.03555022.
- Schaub, D.A., Chu, K-R, and Montgomery, D.C. (1997) ‘Optimising Stereolithography Throughput’, *Journal of Manufacturing Systems*, Vol.16, pp.290-303.
- Schulz, G.V. (1956) ‘Über die Polymerisationskinetik in hochkonzentrierten Systemen – Zur Kinetik des Trommsdorffeffektes an Methylmethacrylat’, *Zeitschrift für Physikalische Chemie*, Vol. 8, pp.190-317.
- Smith, B.C. (1996) *Fundamentals of Fourier Transform Infrared Spectroscopy*, New York: CRC Press.
- Sun, T. and Teja, A.S. (2003) ‘Density, Viscosity, and Thermal Conductivity of Aqueous Ethylene, Diethylene, and Triethylene Glycol Mixture between 290K and 450K’, *Journal of Chemical and Engineering Data*, Vol.48, pp.198-202.
- Steinmann, B. et al. (1995) ‘Photosensitive Compositions’, *United States Patent*, Pat. No. 5,476,748.
- Steinmann, B. et al. (1999) ‘Liquid, Radiation-curable Composition, Especially for Stereolithography’, *United States Patent*, Pat. No. 5,972,563.
- Suematsu, K. and Kohno, M. (2000) ‘Estimation of Critical Points of Branched Polymers’, *American Physical Society, Physical Review E*, Vol.62, pp.3944-53.

- Tang, Y. (2002) 'Stereolithography Cure Modeling', *MS Thesis*, Georgia Institute of Technology.
- Tryson, G.R. and Shultz A.R. (1979) 'A Calorimetric Study of Acrylate Photopolymerization', *J. of Poly. Sci.: Poly. Phys. Ed.*, Vol.17, pp.2059-2075.
- Valles, E.M., and Macosko, C.W. (1979) 'Structure and Viscosity of Poly(dimethylsiloxanes) with Random Branches', *American Chemical Society*, Vol.12, pp.521-526.
- Van Krevelen, D.W. (1990) *Properties of Polymers – their correlation with chemical structure; their numerical estimation and prediction from additive group contributions*, New York: Elsevier.
- Wu, C.F.J. and Hamada, M. (2002), *Experiments Planning, Analysis, and Parameter Design Optimization*, New York: John Wiley & Sons.
- Yaws, C. L. (2003) *Yaws' Handbook of Thermodynamic and Physical Properties of Chemical Compounds*, Norwich, N.Y.: Knovel.